



ORNL/Sub/85-22011/1

**OAK RIDGE  
NATIONAL  
LABORATORY**

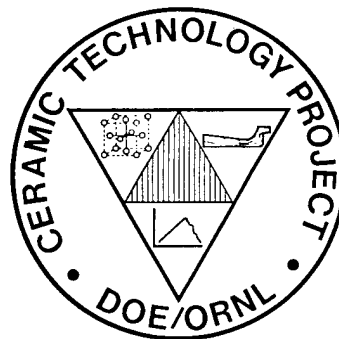
**MARTIN MARIETTA**

**Dispersoid-Toughened Silicon  
Nitride Composites**

**Final Report**

S. T. Buljan  
J. G. Baldoni  
J. Neil  
G. Zilberstein

*CERAMIC TECHNOLOGY FOR  
ADVANCED HEAT ENGINES*



19980819 126

Prepared by  
GTE Laboratories incorporated  
40 Sylvan Road

PLEASE RETURN TO Waltham, Massachusetts 02254

OPERATED BY  
MARTIN MARIETTA ENERGY SYSTEMS, INC.  
FOR THE UNITED STATES  
DEPARTMENT OF ENERGY

BMD TECHNICAL INFORMATION CENTER  
BALLISTIC MISSILE DEFENSE ORGANIZATION  
7100 DEFENSE PENTAGON  
WASHINGTON D.C. 20301-7100

42541

Printed in the United States of America. Available from  
National Technical Information Service  
U.S. Department of Commerce  
5285 Port Royal Road, Springfield, Virginia 22161  
NTIS price codes—Printed Copy: A06 Microfiche A01

This report was prepared as an account of work sponsored by an agency of the United States Government. Neither the United States Government nor any agency thereof, nor any of their employees, makes any warranty, express or implied, or assumes any legal liability or responsibility for the accuracy, completeness, or usefulness of any information, apparatus, product, or process disclosed, or represents that its use would not infringe privately owned rights. Reference herein to any specific commercial product, process, or service by trade name, trademark, manufacturer, or otherwise, does not necessarily constitute or imply its endorsement, recommendation, or favoring by the United States Government or any agency thereof. The views and opinions of authors expressed herein do not necessarily state or reflect those of the United States Government or any agency thereof.

ORNL/Sub/85-22011/1  
Dist. Category UC-95

DISPERSOID-TOUGHENED SILICON  
NITRIDE COMPOSITES

S. T. Buljan, J. G. Baldoni, J. Neil,  
and G. Zilberstein

Date Published - September 1988

FINAL REPORT

Prepared by  
GTE Laboratories Incorporated  
40 Sylvan Road  
Waltham, Massachusetts 02254  
Subcontract No. 86X-22011C

Prepared for the  
Assistant Secretary for Conservation  
and Renewable Energy  
Office of Transportation Systems  
Advanced Materials Development Program  
EE 04 00 00 0

for  
OAK RIDGE NATIONAL LABORATORY  
Oak Ridge, Tennessee 37831  
operated by  
MARTIN MARIETTA ENERGY SYSTEMS, INC.  
for the  
U.S. DEPARTMENT OF ENERGY  
under contract DE-AC05-84OR21400

## Table of Contents

	<u>Page</u>
List of Figures . . . . .	v
List of Tables . . . . .	ix
Abstract . . . . .	1
Introduction . . . . .	1
I. Material Characterization and Development . . . . .	5
Precursor Materials . . . . .	5
Powder Processing . . . . .	6
Test Methods . . . . .	8
Si <sub>3</sub> N <sub>4</sub> -TiC System . . . . .	9
Composites with Particulate TiC . . . . .	9
Composites with TiC Whiskers . . . . .	19
Si <sub>3</sub> N <sub>4</sub> -SiC System . . . . .	21
Composites with Particulate SiC . . . . .	21
Composites with SiC Whiskers . . . . .	23
Powder Processing . . . . .	23
Densification . . . . .	26
Fracture Strength and Toughness . . . . .	26
Fracture Toughness-Crack Length Dependence . . . . .	34
Slow Crack Growth and Creep Resistance . . . . .	35
Oxidation Resistance . . . . .	40
Thermal Conductivity . . . . .	44
Thermal Expansion . . . . .	44
II. Development of Process for Complex Part Fabrication . . . . .	48
Powder Preparation . . . . .	48
Compounding . . . . .	49
Injection Molding . . . . .	50
Binder Removal . . . . .	51
Hot Isostatic Pressing . . . . .	51
Study of Distortion Mechanism . . . . .	52
Conclusions . . . . .	57
References . . . . .	57
Publications . . . . .	59
Presentations . . . . .	59
Appendix 1: Engineering Property Data for Si <sub>3</sub> N <sub>4</sub> and 30 v/o SiC Whisker Composites . . . . .	61
Appendix 2: Indentation Fracture Toughness . . . . .	63

## List of Figures

	<u>Page</u>
Figure 1. Schematic Representation of Crack Bowing Between Dispersoid Particles	3
Figure 2. Schematic Representation of (a) the Residual Stress State Around the Dispersoid, Having a Higher Thermal Expansion than the Matrix and (b) Resulting Crack Deflection	3
Figure 3. Theoretical Predictions of Composite Toughening by Dispersoids of Various Shapes	4
Figure 4. Size Distribution of Whiskers (a) SiC (ARCO SC-9) and (b) TiC (GTTEL)	7
Figure 5. Whisker Composite Process Flow Sheet	7
Figure 6. Two-Dimensional Finite Element Model of Ceramic Composite Microstructure	10
Figure 7. Crack-Dispersoid Interactions: (a-c) $\text{Si}_3\text{N}_4$ (AY6)-TiC; (d-e) $\text{Al}_2\text{O}_3$ -TiC	12
Figure 8. Fracture Toughness of $\text{Si}_3\text{N}_4$ (AY6)-TiC (2 $\mu\text{m}$ ) Composites As a Function of Dispersoid Content	13
Figure 9. Microstructures of $\text{Si}_3\text{N}_4$ (AY6)-TiC Composites Prepared by (a) a Standard and (b) an Extended Time Processing	13
Figure 10. TEM Bright Field Images of the (a) Dispersoid-Free and (b) 30 v/o TiC-Containing $\text{Si}_3\text{N}_4$ (AY6) Composites	14
Figure 11. $\text{Si}_3\text{N}_4$ Grain Size (Equivalent Diameter) Distribution in (a) the $\text{Si}_3\text{N}_4$ (AY6)-30 v/o TiC Composite and (b) the $\text{Si}_3\text{N}_4$ (AY6) Monolith	15
Figure 12. Energy-Dispersive X-ray Spectrum of the Glass Phase (Indicated by a Circle on the Upper Micrograph) in the $\text{Si}_3\text{N}_4$ (AY6)-30 v/o TiC Composite	15
Figure 13. Crack Propagation in (a) a $\text{Si}_3\text{N}_4$ (AY6) Monolith and (b) a $\text{Si}_3\text{N}_4$ (AY6)-20 v/o TiC Composite	16
Figure 14. Intergranular Crack Path and Deflection in a Matrix of $\text{Si}_3\text{N}_4$ (AY6)-30 v/o TiC Composite	17
Figure 15. Model of Crack Deflection Dependency on Grain Size	17
Figure 16. Microstructure of a $\text{Si}_3\text{N}_4$ (AY6) + 10 v/o TiC Whisker Composite	20
Figure 17. Room-Temperature Fracture Toughness of $\text{Si}_3\text{N}_4$ (AY6)-Based Composites Containing 0.5 $\mu\text{m}$ or 8 $\mu\text{m}$ SiC Particulates	21
Figure 18. Fracture Energy of SiC Particulate/ $\text{Si}_3\text{N}_4$ Composites As a Function of Dispersoid Content and Size	22

**List of Figures  
(Continued)**

	<u>Page</u>
Figure 19. Particulate Material Contained in ARCO SiC Whiskers	24
Figure 20. Microstructure of a $\text{Si}_3\text{N}_4$ (AY6)-20 v/o SiC Whisker Composite	25
Figure 21. Densification of $\text{Si}_3\text{N}_4$ (AY6)-Based Ceramics	27
Figure 22. Room-Temperature Fracture Toughness of $\text{Si}_3\text{N}_4$ (AY6)-SiC Whisker Composites	27
Figure 23. Fracture Surfaces of $\text{Si}_3\text{N}_4$ (AY6)-Based Ceramics Broken at Room Temperature	28
Figure 24. Room-Temperature Modulus of Rupture of $\text{Si}_3\text{N}_4$ (AY6)-SiC Whisker Composites	29
Figure 25. Fracture Toughness ( $K_{IC}$ ) and Modulus of Rupture (MOR) of $\text{Si}_3\text{N}_4$ (AY6)-SiC Whisker Composites at (a) 1000°C and (b) 1200°C	29
Figure 26. Indentation-Induced Crack Propagation	31
Figure 27. Fracture Surface of Silicon Nitride Base Material Held at Sintering Temperature for (a) 90 and (b) 400 min	31
Figure 28. TEM Bright Field Images and the $\text{Si}_3\text{N}_4$ Grain Size (Equivalent Diameter) Distributions in the $\text{Si}_3\text{N}_4$ -20 v/o SiC Whisker Composites Hot Pressed for (a) 210 min and (b) 400 min	33
Figure 29. Comparison Between the Measured and Calculated $K_{IC}$ Values vs SiC Content for AY6-(0-30) v/o SiC Whisker Composites Hot Pressed (a) 400 min; (b) Minimum Time to Full Density	33
Figure 30. Shape Distribution of $\text{Si}_3\text{N}_4$ Grains in AY6-20 v/o SiC Whisker Composites Hot Pressed for (a) 210 min and (b) 400 min	34
Figure 31. Modulus of Rupture of AY6- $\text{Si}_3\text{N}_4$ Monolith and 30 v/o SiC Whisker Composite with Vickers Indentations Produced at Various Loads	35
Figure 32. Modulus of Rupture of $\text{Si}_3\text{N}_4$ (AY6) Ceramics and $\text{Si}_3\text{N}_4$ (AY6) + 30 v/o SiC Whisker Composite up to 1400°C	36
Figure 33. Results of Four-Point Creep Evaluation for (a) Monolithic $\text{Si}_3\text{N}_4$ (AY6) and $\text{Si}_3\text{N}_4$ (AY6)-30 v/o SiCw Composite (b) Comparison of $\text{Si}_3\text{N}_4$ (AY6) and $\text{Si}_3\text{N}_4$ (AY6)-30 v/o SiCw Composite and Pre-cracked Composite in Four-Point Creep (c) Effect of SiC Dispersoid Morphology Equiaxed Particle (p) vs Whisker (w) on the Creep of $\text{Si}_3\text{N}_4$ (AY6)-Based Materials (d) Four-Point Creep at 1200°C of $\text{Si}_3\text{N}_4$ (AY6) and $\text{Si}_3\text{N}_4$ (AY6)-30 v/o SiC Whisker Composite	37

**List of Figures  
(Continued)**

	<u>Page</u>
Figure 34. Steady State Compressive Creep Test of $\text{Si}_3\text{N}_4$ (AY6) and a $\text{Si}_3\text{N}_4$ (AY6)-30 v/o SiC Whisker Composite (after R.D. Nixon, et al.)	39
Figure 35. Ambient Atmosphere Oxidation at 1200 °C of $\text{Si}_3\text{N}_3$ (AY6) and an $\text{Si}_3\text{N}_4$ (AY6) + 30 v/o SiCw (SC-9) Composite	40
Figure 36. Auger Elemental Profiles Through the Oxide Scale Formed on the $\text{Si}_3\text{N}_4$ (AY6)-30 v/o SiC Whisker Composite After 200 hr Oxidation in Static Air at 1200 °C	41
Figure 37. SEM Photomicrograph of the Oxidized Surface Layer of $\text{Si}_3\text{N}_4$ (AY6)-30 v/o ARCO SiC Whiskers (100 hr, 1200 °C, Static Air)	42
Figure 38. Static Air Oxidation of ARCO (SC-9) SiC Whiskers	43
Figure 39. Thermal Conductivity of $\text{Si}_3\text{N}_4$ (AY6) and a $\text{Si}_3\text{N}_4$ (AY6) + 30 v/o SiC Whisker Composite up to 1200 °C	47
Figure 40. Thermal Expansion of Baseline $\text{Si}_3\text{N}_4$ (AY6) and $\text{Si}_3\text{N}_4$ (AY6) Containing 30 v/o SiC Whiskers As a Function of Temperature	48
Figure 41. Outline of Process Development Approach	49
Figure 42. Series of Short Shots Showing Fill Pattern of $\text{Si}_3\text{N}_4$ /Binder Mix in CATE Turbine Blade and Test Bar Die	50
Figure 43. Fracture Surface of Injection-Molded $\text{Si}_3\text{N}_4$ (AY6)-30 v/o SiC Whisker Composite	51
Figure 44. Injection-Molded CATE Blades Prepared from $\text{Si}_3\text{N}_4$ -30 v/o SiC (Whisker) Composite in As-Molded, Dewaxed, and Fired State	52
Figure 45. Distortion of Injection-Molded, HIPed Test Bars Containing $\text{Si}_3\text{N}_4$ -30 v/o SiC Whiskers	53
Figure 46. Regions Examined on Bar Cross Section for Whisker Orientation Determinations	54
Figure 47. Digitized SiC Whiskers in Injection-Molded and HIPed Material Showing Orientation and Length/Diameter of Each Measured Whisker	55
Figure 48. Whisker Orientation Model for Test Bar	55
Figure 49. Process Flow Sheet	56

**List of Figures  
(Continued)**

	<u>Page</u>
Figure A2-1. Appearance of Vickers Indentation and Parameters Used for $K_C$	63
Figure A2-2. Appearance of Vickers Indentation and Parameters Used for IFT Determination at GTE Laboratories	64



## List of Tables

	<u>Page</u>
Table 1. Potential Toughening Mechanisms for Ceramic-Matrix Composites with Particulate or Whisker Dispersoids	2
Table 2. Properties of Composite Constituents	5
Table 3. Impurities in Precursor Powders	6
Table 4. Material Properties Used for Finite Element Analyses	11
Table 5. Mechanical Properties of $\text{Si}_3\text{N}_4$ (AY6)-TiC Particulate Composites	19
Table 6. Mechanical Properties of $\text{Si}_3\text{N}_4$ (AY6)-TiC Whisker Composites	20
Table 7. Fracture Toughness, Modulus of Rupture, and Elastic Constants of $\text{Si}_3\text{N}_4$ (AY6) Composites with SiC (8 $\mu\text{m}$ ) Particulates at Room and Elevated Temperatures	23
Table 8. Average Whisker Lengths and Relative Amounts Obtained from Separated Column Levels	24
Table 9. Characterization of SiC Whisker Lengths After Various Process Steps	26
Table 10. Mechanical Properties Comparison of $\text{Si}_3\text{N}_4$ (AY6)-30 v/o SiC Whisker Composites Containing As-Received or Separated Whiskers	26
Table 11. Elastic Constants for $\text{Si}_3\text{N}_4$ (AY6) and $\text{Si}_3\text{N}_4$ (AY6)-SiC Whisker Composites	28
Table 12. Indentation Fracture Toughness Anisotropy in Hot-Pressed Silicon Nitride-Based Ceramics	30
Table 13. Grain Size and Fracture Toughness Data of $\text{Si}_3\text{N}_4$ (AY6)-SiC Whisker Composites	32
Table 14. Oxidation Rate Constants of Investigated Materials	43
Table 15. Strength of Oxidized Silicon Nitride-Based Ceramics	44
Table 16. Enthalpy and Specific Heat for $\text{Si}_3\text{N}_4$ (AY6)	45
Table 17. Enthalpy and Specific Heat Values for $\text{Si}_3\text{N}_4$ (AY6)-30 v/o SiC Whisker Composite	45
Table 18. Thermal Diffusivity/Conductivity of $\text{Si}_3\text{N}_4$ (AY6)	46
Table 19. Thermal Diffusivity/Conductivity of $\text{Si}_3\text{N}_4$ (AY6)-30 v/o SiC Whisker Composite	46
Table 20. Thermal Expansion Coefficients of $\text{Si}_3\text{N}_4$ (AY6) and $\text{Si}_3\text{N}_4$ (AY6) Containing 30 v/o SiC Whisker Composite	47
Table 21. Normalized Densification Shrinkage of Injection-Molded Composites Containing 30 v/o SiC Additions	53

**List of Tables  
(Continued)**

	<u>Page</u>
Table A2-1. Indentation data and calculated indentation fracture toughness (IFT)	66
Table A2-2. Indentation Fracture toughness of $\text{Si}_3\text{N}_4$ (AY6) + 30 v/o TiC accessed by various techniques	67

## **DISPERSOID-TOUGHENED SILICON NITRIDE COMPOSITES\***

**S.T. Buljan, J.G. Baldoni, M.L. Huckabee, J. Neil, and G. Zilberstein**

### **ABSTRACT**

This report is a summary of results of a study aimed at the development of silicon nitride composites of enhanced fracture toughness and strength utilizing particulate and whisker dispersoids. Composites with 40% higher fracture toughness and 25% higher room-temperature fracture strength over that of the base silicon nitride "monolith" have been prepared using 30 v/o SiC whisker dispersoids. An increase in fracture toughness of 70% has been observed at 35 v/o whisker additions. Both fracture toughness and strength improvements persist over a wide range of temperatures (25–1200 °C). These composites exhibit excellent oxidation resistance and improved resistance to slow crack growth and creep at elevated temperatures.

A process for fabrication of complex composite ceramic parts was developed and demonstrated. The present study has also provided extensive information regarding microstructure-property dependence in dispersoid-modified ceramics, which has been utilized to derive a formal theory of fracture toughness and microstructure relationship.

### **INTRODUCTION**

The application of silicon nitride, as well as other ceramics, in the demanding heat engine environment is limited by their relatively low flaw tolerance. Improvement in the strength, and particularly the fracture toughness, of these materials would considerably expand their application range and contribute to a more rapid development of heat engines.

The development of silicon nitride composites offers a potential for considerable improvement in mechanical properties. Options include the development of fiber and dispersoid composites and laminates.

Considering the difficulties encountered in the development of fiber-reinforced materials, the utilization of particulates and whiskers as toughening constituents appears more near-term and, to some extent, economically more appealing due to simpler processing. Work on such silicon nitride-based composites was initiated in the 1970's and early 1980's.<sup>1-5</sup> Intended applications have directed the research, and while fracture toughness was an important issue, it did not dominate all the development efforts. Other properties such as hardness and chemical and electrical characteristics were given more attention for wear, corrosive environment, and electrical applications.

---

\*Research sponsored by the U.S. Department of Energy, Assistant Secretary for conservation and Renewable Energy, Office of Transportation systems, as part of the Ceramic Technology for Advanced Heat Engines Project of the Advanced Materials Development Program, under contract DE-AC05-84OR21400 with Martin Marietta Energy Systems, Inc.

The concepts of composite toughening by particulate and short fiber dispersoids are listed in Table 1. The usefulness of some of these can be restricted by severe application conditions. In advanced heat engines, where lifetimes of 10,000 hours are a goal, microcracking leads to a reduction in the component strength and the elastic modulus. Additionally, internal oxidation along microcracks or spalling of microcracked areas means that the reliability of materials toughened by this mechanism is not acceptable for such demanding applications.

Table 1. Potential toughening mechanisms for ceramic-matrix composites with particulate or whisker dispersoids

Mechanism	Description
Microcracking	Crack interaction with residual strain field around dispersoid to create process zone ahead of crack tip
Phase Transformation	Dispersoid volumetric change by phase transformation creating a process zone to shield crack from applied stress
Crack Impediment	Crack blunting by dispersoid or line tension impeding crack propagation
Crack Deflection	Surface toughening and crack tilting and twisting during propagation around dispersoid caused by thermal expansion mismatch and/or elastic modulus mismatch stresses
Crack Bridging	Pullout and crack bridging by whisker dispersoids

Phase-transformation toughening also has limited promise for  $\text{Si}_3\text{N}_4$ -based composites. Careful consideration of the various additives that could toughen a  $\text{Si}_3\text{N}_4$  matrix by this means has indicated that many of them would combine chemically with the  $\text{SiO}_2$ -based second phase during consolidation. However, some of them may be applicable in reaction-bonded silicon nitride (RBSN). The utilization of this mechanism has not yielded the thermal stability required, particularly for applications in engine components which are exposed to elevated temperatures for an extended period of time.

Crack impediment by the ductile dispersoids may be another somewhat less attractive option. It has been shown that in a metal dispersoid/brittle matrix composite, the advancing crack front may be blunted when it encounters the ductile dispersoid obstacle, which can deform plastically.<sup>6</sup> The plastic deformation absorbs sufficient energy to stop crack propagation and therefore toughens the ceramic composite. In addition to crack blunting, the relaxed stress field around the dispersoid may allow a second crack blunting interaction to become active, that of line tension. The line tension effect is analogous to dislocation motion past obstacles as illustrated in Figure 1.<sup>7</sup> The stress needed to propagate the bowed segments of the crack front is greater than that needed to propagate the crack in a dispersoid-free material, hence an increase in toughness results. Metallic dispersoids, however, restrict the use of composites to

low temperatures due to reduced oxidation resistance. Some ceramic systems may, however, provide an alternative. For example, in the  $\text{Si}_3\text{N}_4$ -TiC system, a crack impediment may become operative at high temperatures, since it was reported<sup>8</sup> that TiC undergoes a brittle-ductile transition between 800 and 900°C.

The predominant toughening mechanism that has so far been explored in composite development for applications in severe environments has been crack deflection and bridging by crack interaction with the dispersed, hard refractory particulates or whiskers. The deflection mechanism originates in the presence of a stress field surrounding the dispersoid along the matrix/dispersoid interface, which is caused by thermal expansion or elastic modulus mismatch. A considerable number of potential dispersoids (e.g., refractory carbides) have higher thermal expansion coefficients than  $\text{Si}_3\text{N}_4$  so that the residual strain state in the  $\text{Si}_3\text{N}_4$  matrix surrounding such dispersoids is, after densification, radial tension and tangential (hoop) compression. This strain state tends to divert an advancing crack around the dispersoid as depicted in Figure 2.

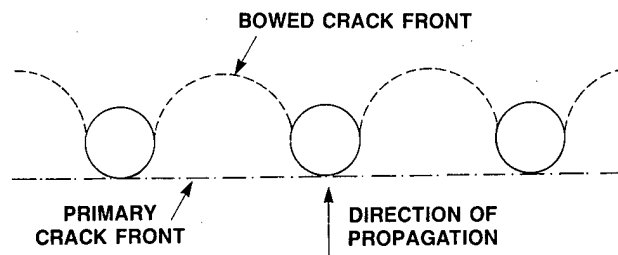


Figure 1. Schematic Representation of Crack Bowing Between Dispersoid Particles<sup>7</sup>

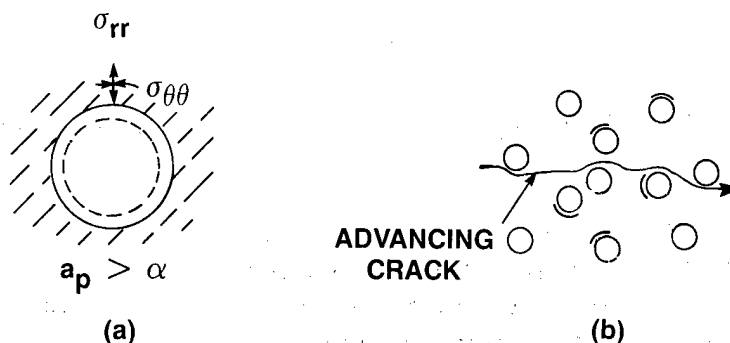


Figure 2. Schematic Representation of (a) the Residual Stress State Around the Dispersoid, Having a Higher Thermal Expansion than the Matrix and (b) Resulting Crack Deflection<sup>11</sup>

Toughening by crack deflection has been postulated to be independent of dispersoid size but dependent on dispersoid volume irrespective of the sign of thermal expansion mismatch stresses. However, this has only been demonstrated in glass-matrix systems,<sup>9,10</sup> which are free of matrix grain boundaries.

The development of composites requires careful consideration of dispersoid shape, as well as its properties. It has been hypothesized that crack deflection, which produces tilting and twisting of the advancing crack front, is an effective toughening mechanism and that the degree of toughening is dependent upon dispersoid shape. On a theoretical basis,<sup>12</sup> rod-shaped particles are predicted to be more effective toughening agents than disc-shaped particles, which are more effective than spheres (see Figure 3). Toughness increases of up to four times, using rod-shaped dispersoids, have been predicted. Attempts to develop ceramic composites of this type have met with limited success.<sup>13,14</sup> Generally, experimental results have deviated considerably from predictions based on the assumption of a homogeneous continuum matrix<sup>6,12</sup> and from results obtained with glass-matrix composites.<sup>9</sup> Additionally, the complexity of composites often results in increased processing difficulties and enlarged processing flaw size. This has at times produced improvements in fracture toughness at the expense of strength.<sup>14</sup>

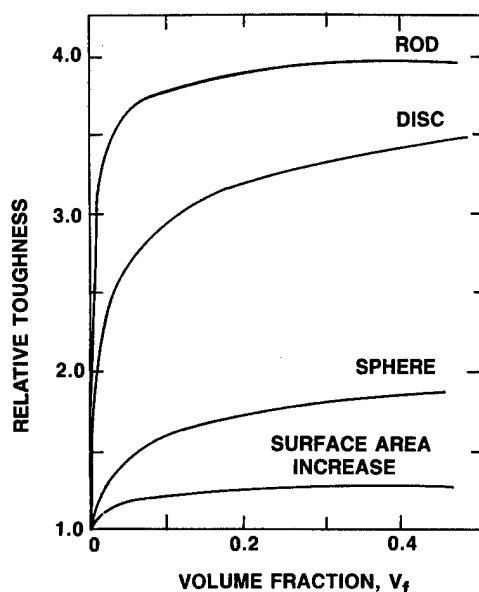


Figure 3. Theoretical Predictions of Composite Toughening by Dispersoids of Various Shapes<sup>12</sup>

The purpose of the present study was to examine the effect of second phase additions on the fracture toughness of silicon nitride and to develop a composite with increased mechanical properties. It was anticipated that crack deflection toughening by crack interaction with dispersed, hard, refractory particulates or whiskers provided the best option. In order to invoke toughening by crack deflection, metal carbides — TiC and SiC in both equiaxed and elongated (whisker) shapes — were employed as dispersoids in a  $\text{Si}_3\text{N}_4 + 6 \text{ w/o } \text{Y}_2\text{O}_3 + 1.5\% \text{ Al}_2\text{O}_3$  (AY6) matrix. Both TiC and SiC have higher thermal expansion coefficients than  $\text{Si}_3\text{N}_4$ , so that the residual strain state in the  $\text{Si}_3\text{N}_4$  matrix surrounding a TiC or SiC dispersoid tends to deflect an advancing crack around the dispersoid.<sup>9,15,16</sup>

The physical properties of these dispersoid constituents are given in the following table (Table 2) and compared with the matrix phase.

Table 2. Properties of composite constituents

	TiC	Si <sub>3</sub> N <sub>4</sub> Matrix-(AY6)	SiC
Young's Modulus (GPa)	430	300	420
Poisson's Ratio	0.19	0.26	0.18
$\mu$ H (GPa)	28.4	12.0	27.4
K <sub>IC</sub> (MPa • m <sup>1/2</sup> )	3.5	4.6	4.6
Thermal Expansion Coefficient, $\alpha$ (10 <sup>-6</sup> /°C)	7.4	3.6	5.0

Since both TiC and SiC have higher moduli of elasticity than Si<sub>3</sub>N<sub>4</sub>, the strain state produced by elastic modulus mismatch, when the composite is under tensile load, also tends to divert the crack around the dispersoid. In Si<sub>3</sub>N<sub>4</sub> + TiC or Si<sub>3</sub>N<sub>4</sub> + SiC composites under load, the residual strain and elastic moduli mismatch effects are additive, and crack deflection is expected.

It was another objective of this investigation to develop and demonstrate fabrication methods and generate a process flow sheet. The intended use of ceramic composites as structural components of automotive engines requires a process capable of producing complex parts in high volumes. Forming of green parts by injection molding and densification by hot isostatic pressing were considered to be processing techniques capable of meeting the above goals. A CATE (DOE-Ceramic Applications in Turbine Engines program) turbine blade, because of its complex shape, was considered a suitable part for process demonstration.

## I. MATERIAL CHARACTERIZATION AND DEVELOPMENT

### PRECURSOR MATERIALS

The results of chemical analysis of the precursor materials used in this study, along with the examination method, are given in Table 3. For the ARCO SC-9 SiC whiskers, examination of small aggregates of particulate matter by Scanning Transmission Electrical Microscopy (STEM) showed the majority of the impurities were contained in these particles and not at the surface of the whiskers. Phase analysis for the materials was determined by x-ray diffraction. The ARCO SiC whiskers were found to be composed of a major phase of  $\beta$ , 8F and minor  $\alpha$ , 4H/8H, while the Lonza SiC and Cerac SiC

particulate materials were found to be  $\alpha$ - $\text{Si}_3\text{N}_4$ . The SiC whiskers had a surface area, determined by BET, of  $3.3 \text{ m}^2/\text{g}$  with average length of  $17.5 \mu\text{m}$  and average diameter of  $0.53 \mu\text{m}$ . The size distributions as determined by quantitative image analysis from SEM photomicrographs are seen in Figure 4a.

Table 3. Impurities in precursor powders

Precursor	Impurities, Wt. %											
	Metals									Nonmetals		
Powder	Al	Mg	Ca	Fe	Cr	Ni	Mn	Mo	Free Si	Free C	O <sub>2</sub>	Cl
	Emission Spectroscopy								XRD	CTC, Leco	NAA	XRF
$\text{Si}_3\text{N}_4^a$	< 0.01	ND	-	< 0.05	ND	ND	ND	0.005	< 1.0	ND	1.5	< 0.05
SiC(W) <sup>b</sup>	< 0.1	0.1-0.3	0.1-0.3	< 0.1	< 0.1	< 0.1	0.1-0.3	ND	ND	0.36	1.78	ND
SiC(P) <sup>c</sup>	0.09	0.002	ND	0.02	ND	< 0.01	0.001	ND	ND	1.00	0.81	ND
SiC(P) <sup>d</sup>	0.02	< 0.003	ND	0.07	ND	0.008	< 0.001	ND	ND	0.60	0.31	ND
TiC(W) <sup>e</sup>	ND	ND	ND	0.07	0.39	0.22	ND	ND	ND	0.19	0.50	ND
TiC(P) <sup>f</sup>	< 0.01	< 0.001	ND	0.01	< 0.02	< 0.01	< 0.001	ND	ND	0.07	0.40	ND

<sup>a</sup>SN-502, GTE Chemical and Metallurgical Division, Towanda, PA

<sup>b</sup>Silar SC-9, originally ARCO Chemical Co., Greer, SC, now owned by Tateho USA.

<sup>c</sup>UF-15 Lonza, AG, CL-4002, Basel, Switzerland

<sup>d</sup>Cerac, Milwaukee, WI

<sup>e</sup>GTE Laboratories Incorporated, Waltham, MA

<sup>f</sup>CA Grade Hermann C. Starck Berlin, NY, NY

The Lonza SiC had a mean particle size of  $0.5 \mu\text{m}$  and a surface area of  $16.5 \text{ m}^2/\text{g}$ , while the mean particle size of the Cerac material was  $8 \mu\text{m}$  and surface area  $0.3 \text{ m}^2/\text{g}$ . The surface area of the TiC powder was  $1.89 \text{ m}^2/\text{g}$ . The TiC whiskers had an average length of  $275 \mu\text{m}$  and average diameter of  $5.1 \mu\text{m}$ . Figure 4b shows the length and diameter size distributions.

The  $\text{Si}_3\text{N}_4$  powder (GTE SN502) typically contained  $\approx 95\%$   $\alpha$ - $\text{Si}_3\text{N}_4$  and  $\approx 5\%$   $\beta$ - $\text{Si}_3\text{N}_4$ , with an initial surface area of  $4.0 \text{ m}^2/\text{g}$  measured by BET. The particles had an acicular morphology.

## POWDER PROCESSING

The baseline  $\text{Si}_3\text{N}_4$ -AY6 material was milled and screened prior to hot pressing. For the particulate composite materials, this composition was milled with the appropriate content of SiC and TiC. Silicon nitride grinding balls were used in all milling steps. To reduce breakup of the SiC and TiC whiskers during milling, an alternative processing route was employed (Figure 5). This process produced good dispersion of the whiskers, but did cause some comminution. A more detailed discussion of this process is included in the discussion of  $\text{Si}_3\text{N}_4$ -SiC whisker composites.

Hot pressing was carried out using BN-coated graphite dies in flowing  $\text{N}_2$  atmosphere for the base material and the SiC composites and flowing argon for the TiC composites to avoid nitridation. The hot-pressing pressure was raised to the maximum



in a stepwise fashion as the temperature increased. Maximum pressure was reached at 1500°C and held for the duration of the hot-pressing cycle. The maximum temperature employed for hot pressing was <1800°C.

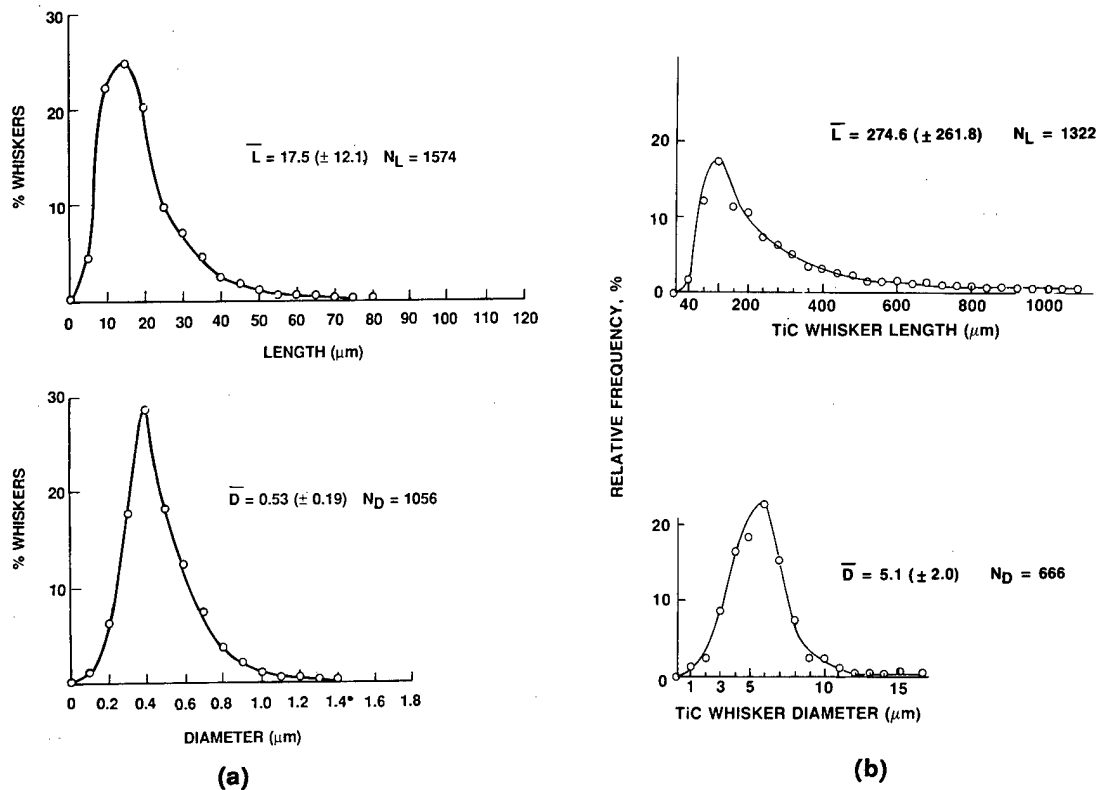


Figure 4. Size Distribution of Whiskers (a) SiC (ARCO SC-9) and (b) TiC (GTCL)

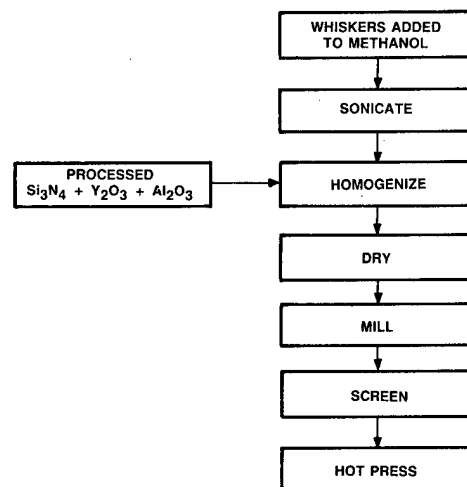


Figure 5. Whisker Composite Process Flow Sheet

## TEST METHODS

Modulus of rupture samples were rectangular bars,  $0.127 \times 0.254 \times 2.5$  cm, machined from the billets with the tensile face perpendicular to the hot-pressing direction. The machine lay was parallel to the length of the bars and the edges were chamfered. The tensile face of each sample was wet-polished to a  $1\text{-}\mu\text{m}$  diamond paste finish.

For fracture toughness measurements by the controlled flaw technique,<sup>17</sup> randomly selected groups of test bars of the monolithic and the composite materials were precracked with a single Knoop indentation. A 100N load was used, with the long axis of the indentation aligned perpendicular to the tensile stress direction of the bars. The precracked samples were annealed in argon at  $1200^\circ\text{C}$  in order to relieve the residual stresses produced by the indentation process.<sup>17</sup> Test bars of the materials, both precracked and nonprecracked, were broken in a four-point loading fixture placed in a tungsten mesh furnace. Inner and outer loading points were 1.016 and 2.286 cm, respectively. Room-temperature testing was performed in air and high-temperature testing in flowing argon with a minimum of three specimens tested at each temperature. A crosshead speed of 0.05 cm/min was used for all tests. The fracture surfaces of each broken, precracked test bar were examined by optical and scanning electron microscopy, and the individual induced surface flaw sizes were measured from photomicrographs. Fracture toughness,  $K_{IC}$ , was calculated using the relationships given in Appendix 1.

Samples for indentation fracture toughness (IFT) determination<sup>18-20</sup> were polished sections cut from the same hot-pressed billets used for test bars. Polished surfaces both perpendicular and parallel to the hot-pressing direction were indented for investigations of anisotropy. Microhardness values were obtained using a Knoop indenter with a load of 10N, while IFT values were determined using a Vickers diamond pyramid indenter at a load of 100N.

The modulus of elasticity of selected materials was measured at room temperature in directions parallel and perpendicular to the direction of applied hot-pressing load using the pulse-echo overlap sonic technique.

The thermal expansion coefficients of materials were determined using a dilatometer. Samples were rectangular ( $0.250 \times 0.250 \times 1.000$  in.) bars. Measurements were made in an inert atmosphere by heating the bar from room temperature at a constant heating rate, interrupting the heating and allowing the bar to equilibrate, then increasing the temperature to a higher level. Seven points were selected for measurement between room temperature and  $1400^\circ\text{C}$ .

The oxidation tests were conducted employing MOR bars in conventional laboratory furnaces for 20 to 1000 hours exposure. Specimens, supported on Pt wires, are weighed prior to the test and after each exposure period. All oxidation exposures were in an ambient laboratory air environment (relative humidity  $\approx 50\%$ ). Moduli of rupture of oxidized samples were measured as previously described.

The resistance to creep at elevated temperature was evaluated by two methods. Specimens, 7.6 mm by 3.8 mm dia. right cylinders, were tested in compression in nitrogen in the temperature range  $1150\text{--}1300^\circ\text{C}$ . Modulus of rupture bars were evaluated at  $1200^\circ\text{C}$  in a four-point loading fixture using the same spans employed

for fast fracture evaluation. Tests were conducted in air using a three-point alumina probe and LVDT configuration to measure sample deflection.

Thermal conductivity was determined from measurements of specific heat (calorimeter technique) and thermal diffusivity (laser flash technique). Enthalpy-specific heat measurements were made using the drop-type method. In this approach, specific heat is derived as the slope of the curve describing the enthalpy temperature relationship. Enthalpy is measured with a Bunsen-type ice calorimeter. Specific heat is then derived from the enthalpy data. Enthalpy-specific heat measurements made by the drop ice calorimeter method conform generally to Specification ASTM-D2766-83.

Thermal diffusivity was measured by a laser pulse method. This measurement method conforms generally to Specification ASTM C-714-72. Thermal conductivity ( $\lambda$ ) was calculated using the following relationship:

$$\lambda = \alpha \rho C_p$$

where  $\lambda$  = thermal conductivity

$\alpha$  = thermal diffusivity

$C_p$  = specific heat

$\rho$  = density

### **Si<sub>3</sub>N<sub>4</sub>-TiC SYSTEM**

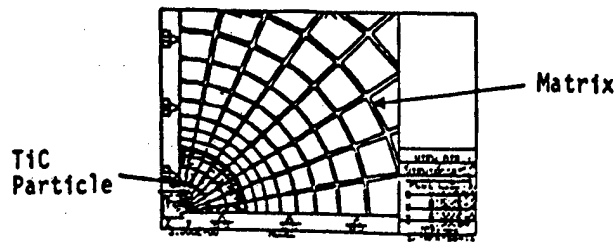
The selection of TiC as a dispersoid to be incorporated in a Si<sub>3</sub>N<sub>4</sub>-based matrix was based on the thermomechanical properties (Table 1), which suggest its potential to provide crack deflection in a Si<sub>3</sub>N<sub>4</sub> matrix. The chemical and structural character of TiC was deemed substantially different from SiC to allow observation of effects of these parameters on composite microstructure development and crack-particle interactions.

#### **Composites with Particulate TiC**

Crack-particle interaction was studied in a Si<sub>3</sub>N<sub>4</sub>-TiC composite and compared to an equivalent Al<sub>2</sub>O<sub>3</sub>-TiC composite. Residual strain produced by thermal expansion mismatch in these two composites is expected to be of opposite sign.

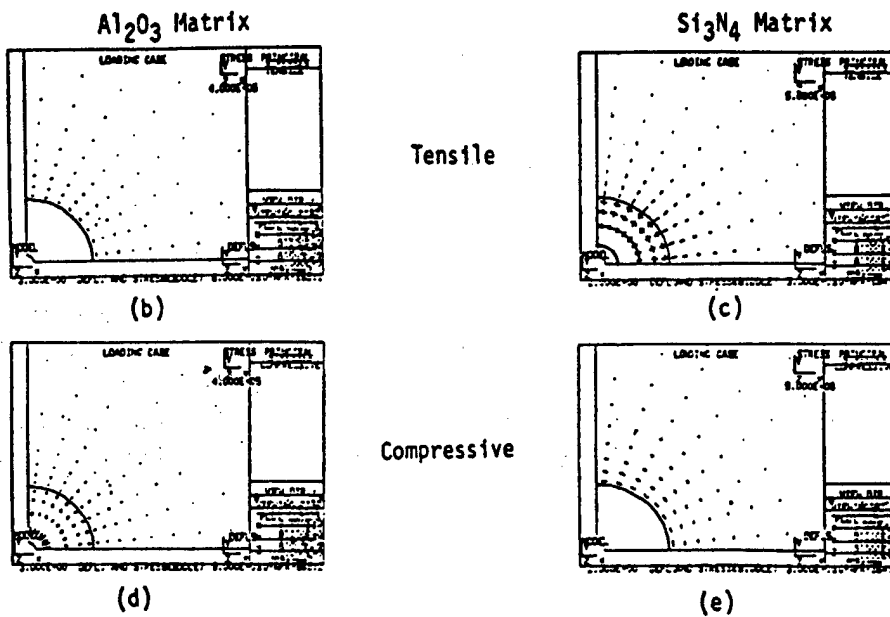
In order to assess the residual state of stress at the interface between TiC and ceramic matrices (Si<sub>3</sub>N<sub>4</sub>, Al<sub>2</sub>O<sub>3</sub>), a computer modeling approach was used. Figure 6a shows the model, which represents a spherical particle that is integrally bonded to the ceramic continuum. The model was reduced to a two-dimensional analysis because of the symmetrical nature of the problem. The material properties used to compute the residual stresses are listed in Table 4.

The differences between thermal expansion coefficients are responsible for the thermal strain mismatch at the matrix/particle interface. Figures 6b-g show the residual stress when a temperature reduction of 800°C from the densification temperature is applied to each of the ceramic composite systems. Inspection of the principal stress distributions for the Al<sub>2</sub>O<sub>3</sub>-TiC material reveals hoop tensile stresses in the Al<sub>2</sub>O<sub>3</sub> matrix, which increase at the interface. The principal compressive stresses are radial through the TiC particle and matrix, with an additional hoop component in the particle region.



(a)

### Comparison of Principal Stresses



### Comparison of Normal Stresses

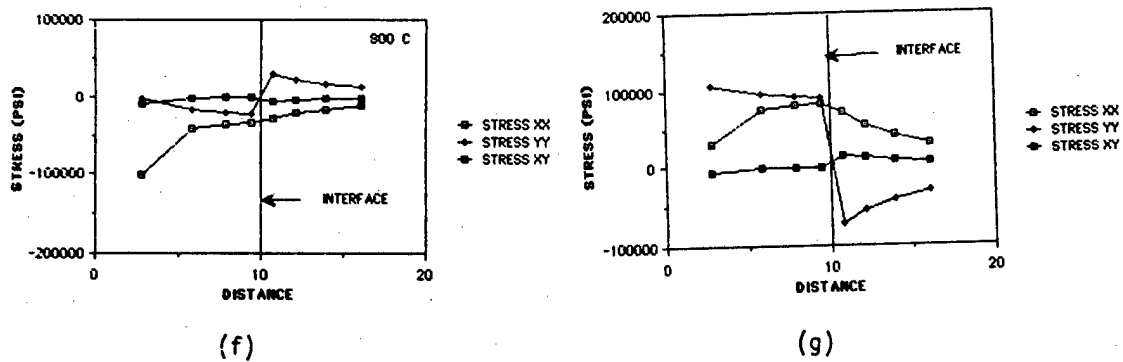


Figure 6. Two-Dimensional Finite Element Model of Ceramic Composite Microstructure

In direct contrast is the  $\text{Si}_3\text{N}_4$ -TiC composite, which reverses the tensile and compressive principal stress distribution. The magnitude of the normal stresses across the particle/matrix interface is greatest for the  $\text{Si}_3\text{N}_4$ -TiC system. The resulting shear stress (stress  $\sigma_{xy}$ ) is essentially invariant, which results from the symmetrical problem definition.

Table 4. Material properties used for finite element analyses

Materials	Modulus of Elasticity, E ( $10^6$ psi)	Poisson's Ratio $\nu$	Coefficient of Thermal Expansion, $\alpha$ ( $10^{-6}/^\circ\text{C}$ )
$\text{Si}_3\text{N}_4$	43	0.26	3.6
$\text{Al}_2\text{O}_3$	54	0.23	8.5
TiC	62	0.19	7.4

To elucidate crack-particle interaction, composites containing TiC single crystals were prepared, indented with a Vickers indenter, and examined. Two basic TiC single-crystal morphologies were observed in the composite microstructures, elongated rectangular grains with  $\{100\}$  planes parallel to the straight edges of the grain and more equiaxed pseudo-hexagonal cross sections of crystals whose habit is defined by a combination of  $\{100\}$  and  $\{120\}$  planes. For the  $\text{Si}_3\text{N}_4$  matrix composite, crack deflection around these grains was generally not observed. However, cleavage steps (deflection) were observed within some rectangular grains (Figure 7b). Crack penetration of the TiC crystal without deflection around the grains was the primary interaction in the majority of the cases observed.

For the  $\text{Al}_2\text{O}_3$ -TiC material, the crack-dispersoid interaction was observed to be dependent on dispersoid morphology. Cracks were observed to penetrate rectangular grains (Figure 7e) and deflect around pseudo-hexagonal grains (Figure 7d). Deflection-induced crack branching was also observed.

These observations indicate that the sign of the thermal expansion mismatch stress affects the tendency for crack deflection to occur for TiC crystals which cleave readily on  $\{100\}$  planes. The radial thermal expansion mismatch stress for TiC in a  $\text{Si}_3\text{N}_4$  matrix is tensile. The addition of the tensile stress field of the advancing crack to the residual stress may produce TiC cleavage and allow the crack front to propagate through the dispersoid phase as observed. For the  $\text{Al}_2\text{O}_3$ -TiC composite, the radial thermal expansion mismatch stress is compressive. Apparently this reduces the tendency for cleavage with the appropriate crack-dispersoid orientation (Figure 7d), although crystal cleavage may still occur if the crack front encounters cleavage planes in a specific direction (Figure 7e).

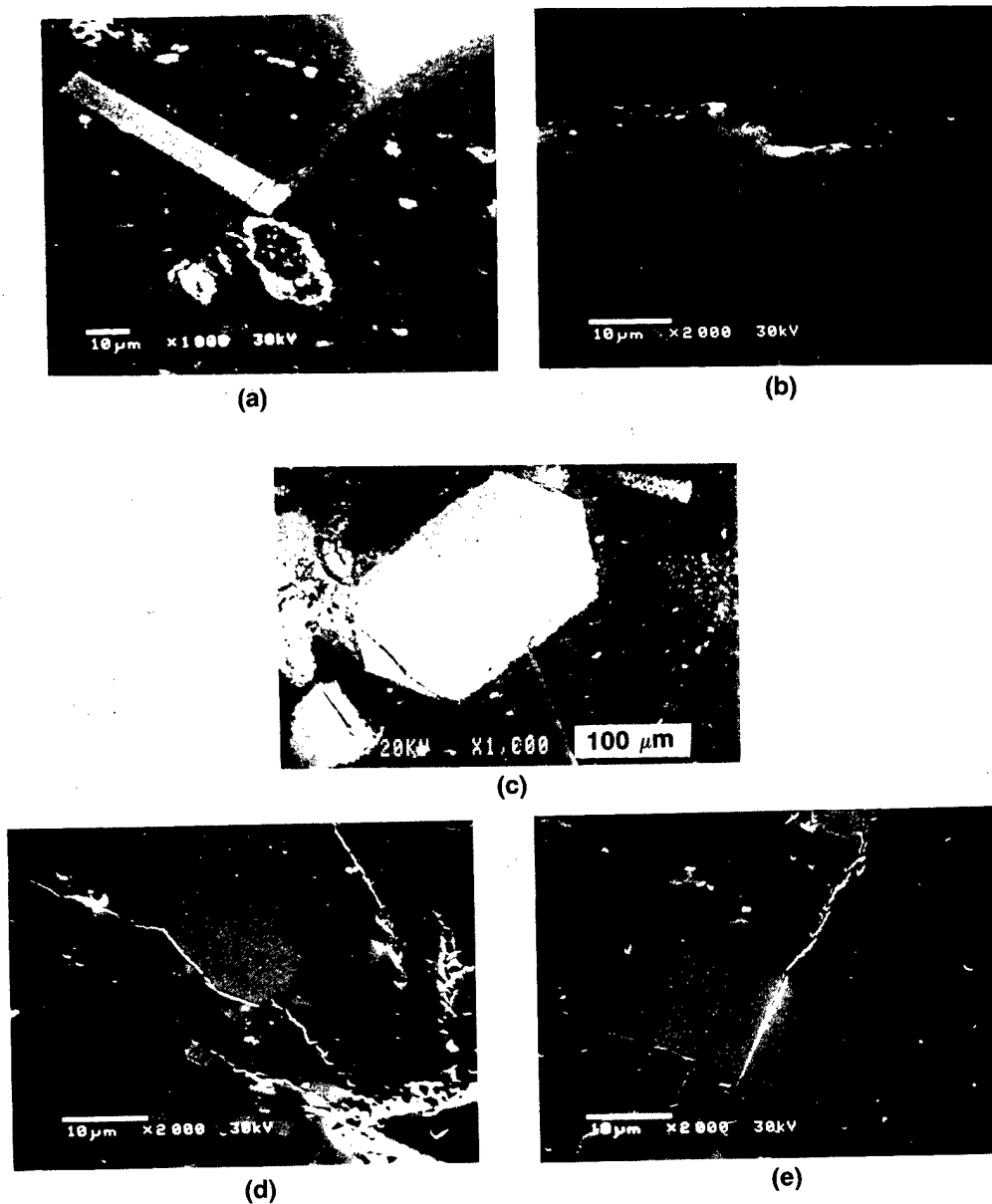


Figure 7. Crack-Dispersoid Interactions: (a-c)  $\text{Si}_3\text{N}_4$  (AY6)-TiC; (d-e)  $\text{Al}_2\text{O}_3$ -TiC

The investigations have demonstrated effective crack-dispersoid interaction and crack deflection in both composite systems. However, the examination of a series of composites containing up to 30 v/o TiC has shown that addition of particulate TiC of an average size of about  $2\text{ }\mu\text{m}$  (Figure 8) produces no change in fracture toughness despite observed crack-particle interaction. It was felt that absence of toughening may be a consequence of a chemical reaction between the matrix and the dispersoid and associated microstructural changes.

The microstructure of  $\text{Si}_3\text{N}_4$ -30 v/o TiC particulate composite prepared by a standard processing schedule is shown in Figure 9a. Holding at the densification temperature for an extended time reveals the presence of a reaction product zone around TiC grains (Figure 9b). It has been shown<sup>21</sup> that this reaction zone is composed of SiC and  $\text{TiC}_{0.5}\text{N}_{0.5}$  crystals which form at elevated temperatures according to the reaction

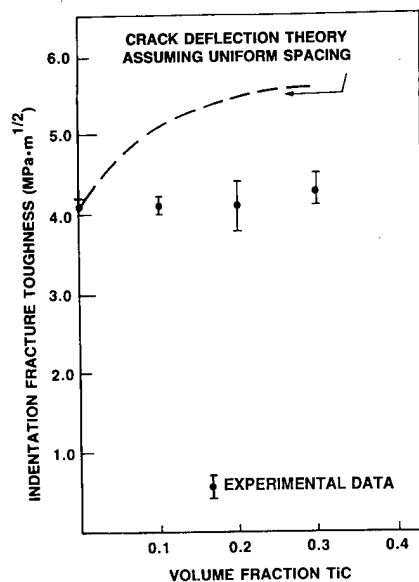
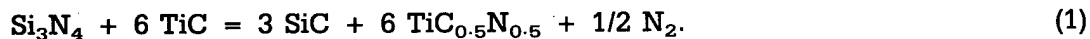


Figure 8. Fracture Toughness of  $\text{Si}_3\text{N}_4$  (AY6)-TiC ( $2 \mu\text{m}$ ) Composites As a Function of Dispersoid Content

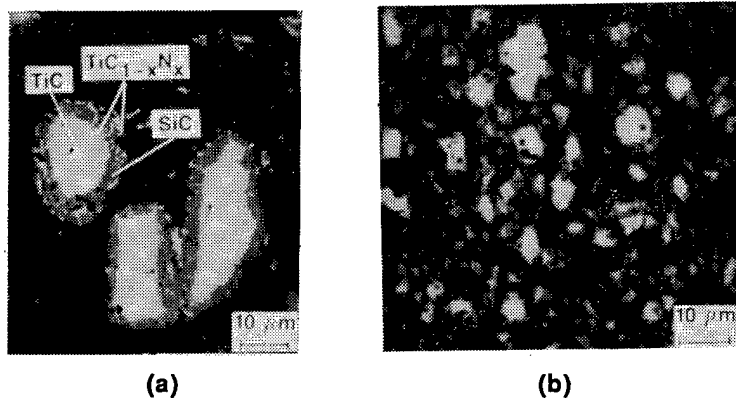


Figure 9. Microstructures of  $\text{Si}_3\text{N}_4$  (AY6)-TiC Composites Prepared by (a) a Standard and (b) an Extended Time Processing

At the densification temperature, the reaction can proceed ( $\Delta G_T \approx -30,000$  cal/mole) until all TiC is consumed. Hence, if the reaction is carried to completion, the properties expected from such a composite, which were based on the properties of the starting materials and their respective (volume) quantities in the composite formulation, will not be realized because of substantial changes in the phase composition. Appropriate adjustment of processing parameters (standard processing schedule, Figure 9a) produces a composite with limited reaction, which essentially preserves the dispersoid properties and confines the reaction to a very narrow zone at the matrix-dispersoid interphase boundary. This limited reaction, however, affects the matrix microstructure development. TEM photomicrographs of the dispersoid-free and the 30 v/o TiC-containing  $\text{Si}_3\text{N}_4$  composite having the same amount of sintering aids and hot pressed identically (Figure 10) show that the  $\text{Si}_3\text{N}_4$  microstructure of the TiC-free material is characterized by larger  $\text{Si}_3\text{N}_4$  grain sizes and a  $\text{Si}_3\text{N}_4$  grain size distribution substantially broader than that of the TiC-containing composite. The silicon nitride grain size distributions were evaluated using quantitative microscopy and are given in Figure 11 as relationships between the  $\text{Si}_3\text{N}_4$  equivalent grain diameter\* and its volume percent of the total  $\text{Si}_3\text{N}_4$  content in each material.



Figure 10: TEM Bright Field Images of the (a) Dispersoid-Free and (b) 30 v/o TiC-Containing  $\text{Si}_3\text{N}_4$  (AY6) Composites

The observed difference in  $\text{Si}_3\text{N}_4$  grain sizes and distributions could be attributed to the differences in the  $\text{Si}_3\text{N}_4$  solution-precipitation and growth behavior, which are apparently influenced by Ti present in the glass phase of  $\text{Si}_3\text{N}_4$ -TiC composite as determined by EDS analysis of the intergranular glass by AEM (Figure 12).

---

\*Diameter of a circle whose area is equal to the grain area measured from the photomicrograph.



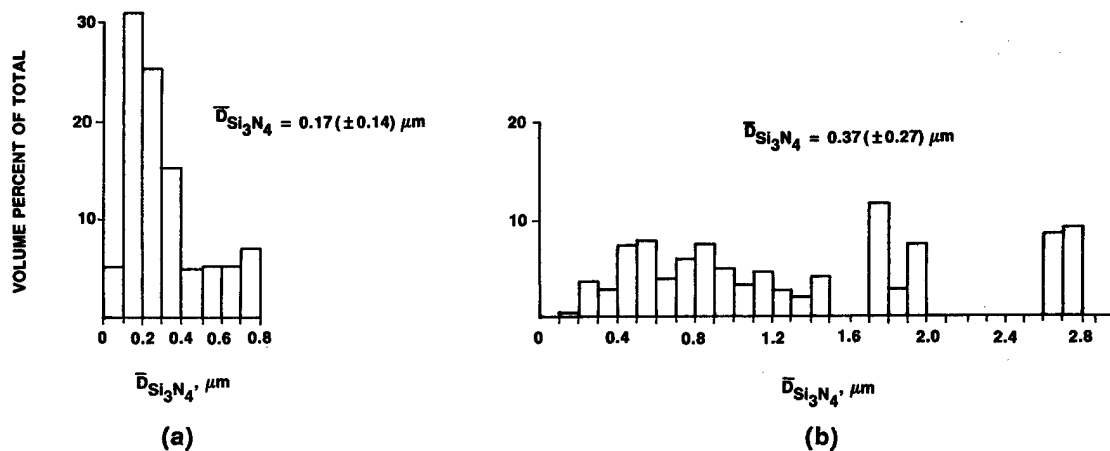


Figure 11.  $\text{Si}_3\text{N}_4$  Grain Size (Equivalent Diameter) Distribution in (a) the  $\text{Si}_3\text{N}_4$  (AY6)-30 v/o TiC Composite and (b) the  $\text{Si}_3\text{N}_4$  (AY6) Monolith

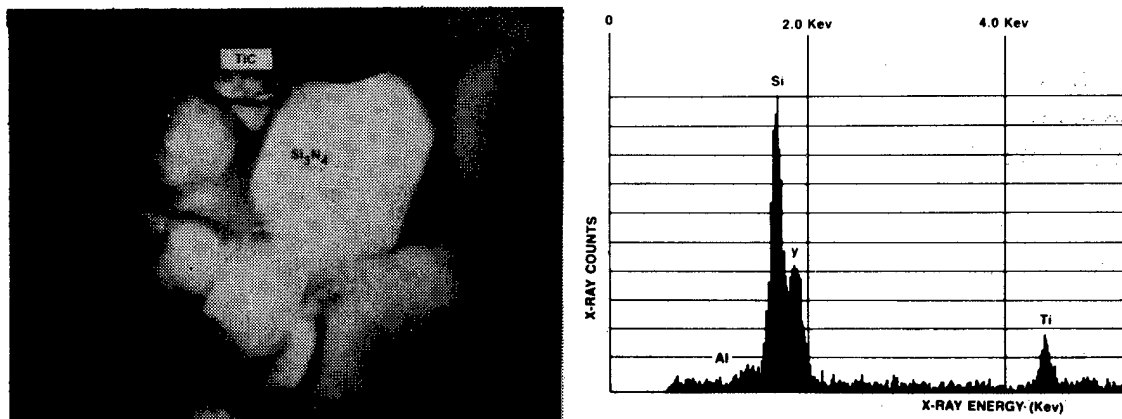


Figure 12. Energy-Dispersive X-ray Spectrum of the Glass Region (Indicated by a Circle on the Upper Photomicrograph) in the  $\text{Si}_3\text{N}_4$  (AY6)-30 v/o TiC Composite

One of the goals pursued in the design of  $\text{Si}_3\text{N}_4$ -TiC composites was to improve the material's fracture toughness by one of the "crack-TiC particle" interaction mechanisms. As was described, the composite's fracture toughness remained at the level of the  $\text{Si}_3\text{N}_4$ -monolith at best. Crack propagation patterns in the  $\text{Si}_3\text{N}_4$  monolith and the  $\text{Si}_3\text{N}_4$ -30 v/o TiC hot-pressed composites were examined on the polished specimen surfaces cracked with a single Vickers indenter using 100 N load (Figure 13). The patterns show that amplitude of crack deflection in the composite matrix is considerably smaller than that observed in the monolith.

The matrix of the  $\text{Si}_3\text{N}_4$ -TiC composite is characterized by a  $\text{Si}_3\text{N}_4$  grain size ( $0.17 \mu\text{m}$ ) that is less than half that of the monolith ( $0.37 \mu\text{m}$ ), and the crack propagation path through the fine grain material, fracturing intergranularly, should be less tortuous than in a coarser grain counterpart (Figure 13). Figure 14 gives an example of an intergranular crack path.

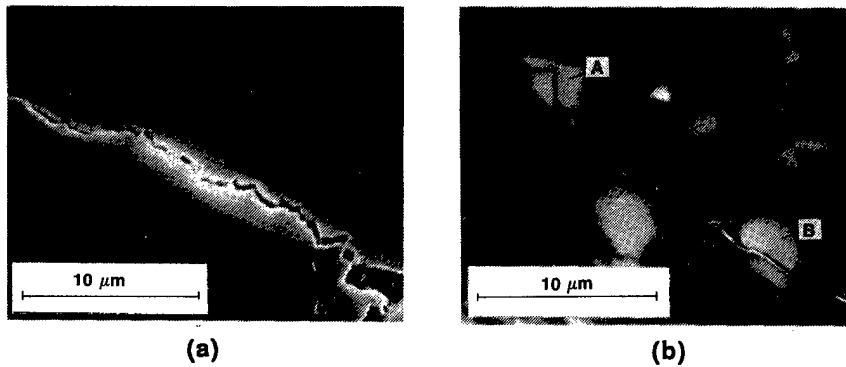


Figure 13. Crack Propagation in (a) a  $\text{Si}_3\text{N}_4$  (AY6) Monolith and (b) a  $\text{Si}_3\text{N}_4$  (AY6)-20 v/o TiC Composite

In a material with a typical intergranular fracture, it is reasonable to expect that the energy expended to propagate the crack is directly proportional to the frequency and amplitude of crack deflection. Crack length (surface) does not increase with an increase in grain size (Figure 15).

In a homogeneous elastic solid, fracture toughness  $K_{IC}$  is directly proportional to the square root of the product of elastic modulus and the energy ( $\gamma$ ) required to create a new surface:

$$K_{IC} = \sqrt{2E\gamma} \quad (2)$$

However, in polycrystalline ceramics, surface energy calculated from experimentally determined values of  $K_{IC}$  and  $E$  varies broadly from those calculated from bond strengths. The difference is due to the presence of intergranular fracture and grain size/shape effects. It seems then plausible to assume that if a polycrystalline solid fractures intergranularly, the measured fracture toughness is proportional to the product of intergranular bond strength (surface energy for intergranular fracture  $\gamma_i$ ) and a function of grain size and shape,  $f(D)$ :

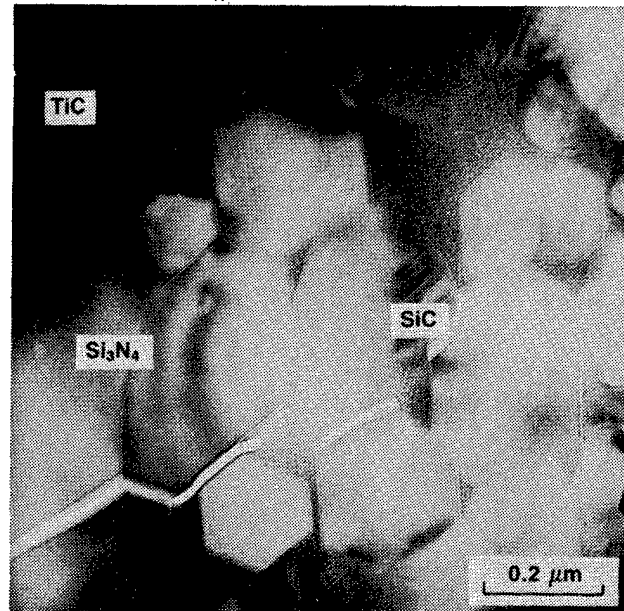


Figure 14. Intergranular Crack Path and Deflection in a Matrix of  $\text{Si}_3\text{N}_4$  (AY6)-30 v/o TiC Composite

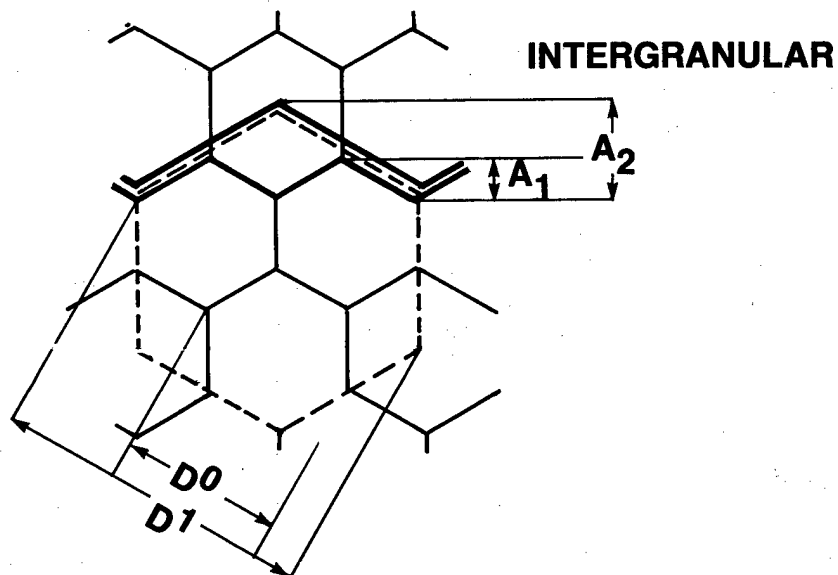


Figure 15. Model of Crack Deflection Dependency on Grain Size

$$K_C = \sqrt{2E\gamma_i f(D)} \quad (3)$$

The expected change in fracture toughness due to grain size can then be expressed as

$$dK_C = E\gamma_i df(D)/K_C \quad df(D) = f'(D)dD \quad (4)$$

or

$$dK_C = \sqrt{E\gamma_i/2f(D)} \cdot df(D). \quad (5)$$

If we assume that  $f(D)$  in the absence of grain shape change is simply  $D$  to calculate the change of  $K_C$  due to change of grain size (without change in fracture mode and  $\gamma_i$ ), one would only need to know  $K_C$  and  $D$  values for one baseline structure  $K_C^0$ ,  $D^0$ , then

$$dK_C = \frac{1}{2} K_C^0 df(D)/\sqrt{f(D)f(D^0)} \quad (6)$$

and substituting  $f(D) = D$

$$dK_C = \frac{1}{2} K_C^0 (dD/\sqrt{DD^0}). \quad (7)$$

For small changes in grain size, eq. (7) below provides a good approximation: (20)

$$dK_C \approx \frac{1}{2} K_C^0 (dD/D^0) \quad (8)$$

Remembering that the relationships above were derived for intergranular fracture only, assessment of grain size effects in real structures has also to consider their diminished contributions in mixed mode fracture, which would, for example, in a 50:50 intergranular/transgranular mode reduce the  $dK_C$  by one half.

Based on these assumptions, the fracture toughness of the composite can be similarly estimated using appropriate fractional contributions of the matrix and dispersoid grain size. According to this analysis, if there is no change in fracture mode or other microstructural features, the interaction of the advancing crack front with finer dispersoids (i.e., smaller than the matrix grains) should result in a toughness reduction and its interaction with coarse dispersoid in an increase of the composite fracture toughness due to the change in amplitude of crack deflection. This model has made it easier to rationalize the toughening behavior in various composite ceramics.

According to the proposed relationship, eq. (7), the expected change in fracture toughness ( $\Delta K_C$ ) due to grain size is

$$\Delta K_C = CK_C^0 (D/D^0 - 1). \quad (9)$$

A typical indentation fracture toughness value measured on a hot-pressed  $\text{Si}_3\text{N}_4$  monolith is  $K_C^0 = 4.1 \text{ MPa}\cdot\text{m}^{1/2}$  (IFT), with the average  $\text{Si}_3\text{N}_4$  grain size  $D^0 = 0.37 \mu\text{m}$ . The expected change in fracture toughness, due to reduced grain size ( $D = 0.17 \mu\text{m}$ ), is represented by  $\Delta K_C = -0.5 \text{ MPa}\cdot\text{m}^{1/2}$ . This calculation assumes 50% intergranular fracture (see page 16). Assuming that there is no major change in the relative amount of energy required to fracture the intergranular phase or in the amount of an intergranular fracture, the fracture toughness of 4.3 (30 v/o)  $\text{MPa}\cdot\text{m}^{1/2}$  measured for  $\text{Si}_3\text{N}_4$  - 30 v/o TiC composite is a product of fracture toughness provided by the crack deflection in  $\text{Si}_3\text{N}_4$  matrix and by TiC dispersoid, where TiC provides toughness increase over the  $\text{Si}_3\text{N}_4$  monolith of finer ( $0.17 \mu\text{m}$ ) grain size. Although it is clear from the discus-

sion presented above that incorporation of a hard dispersoid of a given ( $2\text{ }\mu\text{m}$ ) grain size into  $\text{Si}_3\text{N}_4$  matrix could potentially provide an increase in the composite fracture toughness, this effect is paralleled by the lower fracture toughness as a result of a finer  $\text{Si}_3\text{N}_4$  grain size due to the  $\text{Si}_3\text{N}_4$ -TiC reaction during densification. This effect may be reduced through utilization of coated TiC dispersoids.

The properties of  $\text{Si}_3\text{N}_4$ -TiC particulate composites are summarized in Table 5. Addition of TiC increases the elastic modulus and decreases the Poisson's ratio. Modulus of rupture is also reduced. This reduction can be attributed to an increase in flaw size due to TiC particle agglomeration.

Table 5. Mechanical properties of  $\text{Si}_3\text{N}_4$  (AY6) — TiC particulate composites

Material	MOR (MPa)	IFT (MPa $\cdot$ m <sup>1/2</sup> )	Young's Modulus (GPa)	Poisson's Ratio	Shear Modulus (GPa)	Bulk Modulus (GPa)
AY6	773 $\pm$ 67	4.1 $\pm$ 0.1	297	0.27	116	218
AY6 + 10 v/o TiC	669 $\pm$ 41	4.1 $\pm$ 0.1	317	0.28	124	240
AY6 + 20 v/o TiC	557 $\pm$ 42	4.1 $\pm$ 0.3	332	0.26	132	228
AY6 + 30 v/o TiC	582 $\pm$ 35	4.3 $\pm$ 0.2	349	0.24	141	225

#### Composites with TiC Whiskers

Preparation of the composites containing TiC whiskers followed the procedures previously described and illustrated in Figure 5. For 10 and 20 v/o whisker loadings, hot pressing to full density was achieved in 100 minutes, while 220 minutes was required for the 30 v/o composite. The measured densities for all three compositions were greater than the values calculated using the rule of mixtures for the individual components. X-ray analysis of all hot-pressed billets showed the presence of  $\beta\text{-Si}_3\text{N}_4$ , TiC, and a solid solution of  $\text{Ti}(\text{C},\text{N})$ . The presence of the solid solution phase may account for the increase in the measured density values.

Processing of the TiC whiskers using the homogenization step leads to shortening of the whisker. Figure 16 shows the shortened whiskers in a low volume loaded hot-pressed composite. This figure also illustrates the range of whisker sizes (diameters and lengths) which were observed.

Densification of the whisker-containing composite, due to retarded particle rearrangement, required extended sintering time, which increased the extent of matrix-dispersoid chemical reactions. Large whisker size and reactions with the matrix adversely affect the strength of the composite (Table 6).

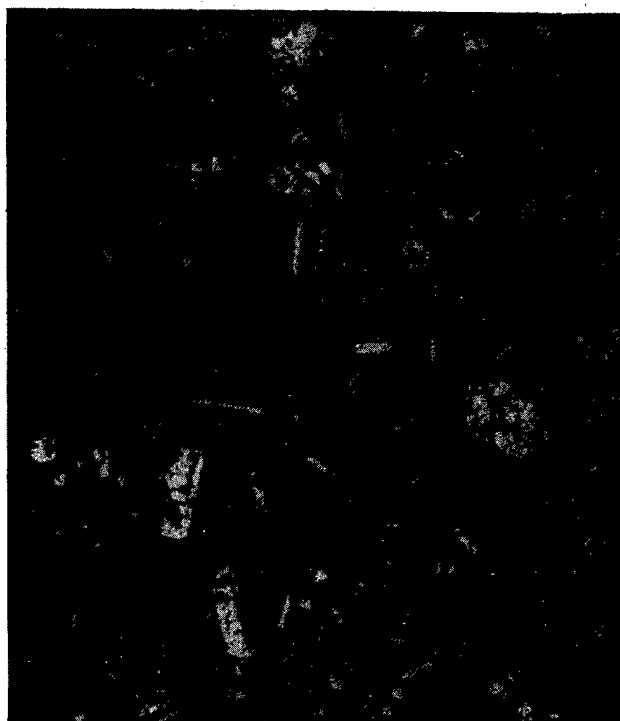


Figure 16. Microstructure of a  $\text{Si}_3\text{N}_4$  (AY6) + 10 v/o TiC Whisker Composite

Table 6. Mechanical properties of  $\text{Si}_3\text{N}_4$  — TiC whisker composites

Material	MOR (MPa)	IFT (MPa $\cdot$ m <sup>1/2</sup> )	Young's Modulus (GPa)	Poisson's Ratio	Shear Modulus (GPa)	Bulk Modulus (GPa)
AY6 + 10 v/o TiC	412 $\pm$ 24	4.1 $\pm$ 0.1	291	0.25	117	192
AY6 + 20 v/o TiC	375 $\pm$ 17	4.4 $\pm$ 0.2	286	0.23	116	177
AY6 + 30 v/o TiC	345 $\pm$ 6	6.1 $\pm$ 1.8	287	0.21	119	164

In light of the above observations, it has become apparent that attainment of simultaneous fracture toughness and strength improvements would require complex process modifications. It was therefore considered more expeditious to concentrate on the  $\text{Si}_3\text{N}_4$ -SiC system.

## Si<sub>3</sub>N<sub>4</sub>-SiC SYSTEM

The high modulus of elasticity of SiC and the stress produced by elastic modulus and thermal expansion mismatch at the matrix-dispersoid interface is expected to invoke the crack deflection mechanism. Higher chemical stability of SiC in contrast with TiC provides for better control of microstructure development during densification.

### Composites with Particulate SiC

The fracture toughness of the Si<sub>3</sub>N<sub>4</sub> composites containing fine ( $\approx 0.5 \mu\text{m}$  APD) SiC particles, as measured by the controlled surface flaw technique, was found to decrease with increasing dispersoid content, while that of the composites containing coarser ( $8 \mu\text{m}$  APD) SiC particles was observed to increase slightly up to 30 v/o dispersed second phase (Figure 17). However, the limited increases in fracture toughness deviated considerably from predictions based on toughening models. Since dispersoids have to meet a certain minimum size requirement, with respect to the matrix grain size, as well as elastic modulus and thermal expansion coefficient mismatch criteria in order to effect toughening by crack deflection, the matrix grain size is apparently larger than  $0.5 \mu\text{m}$  and somewhat smaller than  $8.0 \mu\text{m}$ . Therefore, it is expected that if there is no change in fracture mode or other microstructural features, the interaction of the advancing crack front with the finer dispersoids, i.e., smaller than the matrix grains, would result in a reduction of the composite fracture toughness due to the diminished amplitude of crack deflection.

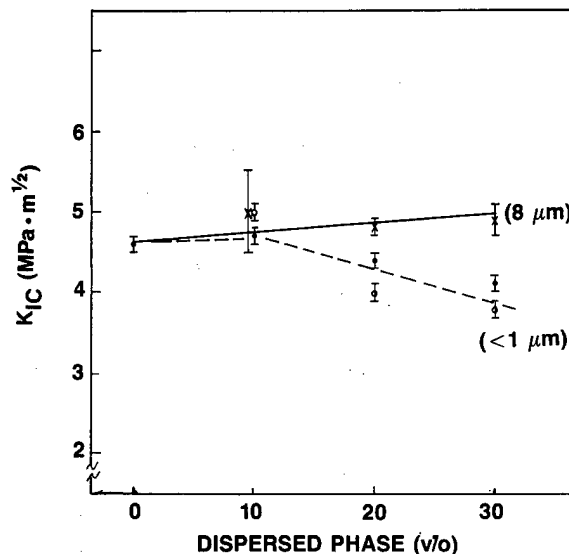


Figure 17: Room-Temperature Fracture Toughness of Si<sub>3</sub>N<sub>4</sub> (AY6)-Based Composites Containing  $0.5 \mu\text{m}$  or  $8.0 \mu\text{m}$  SiC Particles

The addition of coarse SiC particles with a size larger than the matrix grains would in turn be expected to increase the fracture toughness of the composite. These obser-

variations are supported by other published data for  $\text{Si}_3\text{N}_4$  matrix-SiC particulate composites,<sup>1,2</sup> containing various sintering aids. The fracture toughness of SiC- $\text{Si}_3\text{N}_4$  composites has been observed to decrease with increasing concentration of submicron SiC.<sup>2</sup> Another study<sup>1</sup> has indicated that smaller dispersoids of a 5–9  $\mu\text{m}$  particle size do not promote toughening, but indeed decrease the fracture energy (toughness). Increases in toughness were observed only for coarse, 32- $\mu\text{m}$  dispersoids (Figure 18).

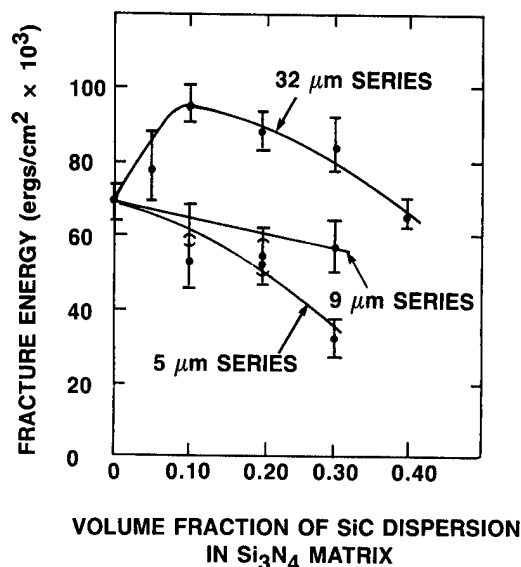


Figure 18: Fracture Energy of SiC Particulate/ $\text{Si}_3\text{N}_4$  Composites As a Function of Dispersoid Content and Size<sup>1</sup>

Since processing in the presence of a dispersoid alters the matrix-microstructure development during consolidation, rationalization of the above results would require complete characterization of the composite microstructure. It is nevertheless conceivable that toughening of  $\text{Si}_3\text{N}_4$  ceramics may require relatively coarse particulate dispersoids, since the effective grain size in the monolithic materials is amplified by the acicular nature of  $\text{Si}_3\text{N}_4$ , which reduces the effectiveness of equiaxed particulates as toughening agents. Under these circumstances, use of whisker dispersoids provides a better option.

Silicon nitride composites with SiC particulate dispersoids densified readily. Compaction rate in hot pressing was only slightly lower than that of matrix material. Composites with dispersoids of 8  $\mu\text{m}$  average particle size exhibited strength equal to or higher than that of the base monolith (Table 7), and while they appeared to have somewhat higher strength at 1000°C, their MOR at 1200°C was essentially equivalent to that of the monolith. The fracture toughness dependence on temperature showed a similar trend.



Table 7. Fracture toughness, modulus of rupture, and elastic constants of  $\text{Si}_3\text{N}_4$  (AY6) composites with SiC ( $8\text{ }\mu\text{m}$ ) particulates at room and elevated temperatures

		Fracture Toughness (MPa · m <sup>1/2</sup> )*			
Material		20°C	1000°C	1200°C	
AY6		4.6 ± 0.2	4.9 ± 0.3	6.1	
AY6 + 10 v/o SiC		5.0 ± 0.6	5.9 ± 0.1	5.9	
AY6 + 20 v/o SiC		4.8 ± 0.1	5.9 ± 0.1	5.8	
AY6 + 30 v/o SiC		4.9 ± 0.2	5.7 ± 0.1	5.7	
		Modulus of Rupture (MPa)			
Material		20°C	1000°C	1200°C	
AY6		773 ± 67	585 ± 14	486 ± 43	
AY6 + 10 v/o SiC		950 ± 56	778 ± 6	517 ± 12	
AY6 + 20 v/o SiC		763 ± 67	715 ± 62	451 ± 33	
AY6 + 30 v/o SiC		885 ± 64	809 ± 31	466 ± 7	
		Young's Modulus (GPa)	Poisson's Ratio	Shear Modulus (GPa)	Bulk Modulus (GPa)
Material					
AY6 + 10 v/o SiC		320	0.26	127	225
AY6 + 20 v/o SiC		338	0.25	136	223
AY6 + 30 v/o SiC		336	0.25	134	225

\*Controlled flaw technique

### Composites with SiC Whiskers

**Powder Processing.** Processes for whisker fabrication are still being developed and yield materials with broad size distribution. As-received whiskers contain sub-micron particles and, more importantly, large particles and hard whisker aggregates. These aggregates and particulates, if processed into the composite, may act as a fracture origin and reduce the composite strength. Particles of various sizes were separated using a sedimentation column, which allows removal of whisker/particle suspension at three different levels. For a given time of settling, the top portion of liquid contains the finest particles and floating debris, the bottom portion, the largest particles, which are to be removed, and the middle, a range of sizes between the two.

Figure 19 shows particulate material obtained from the top section of the column. SEM/EDS analysis of these particles shows the presence of Zn, Mn, Mg, K, Ca, and P, which are probably remnants of the whisker precursor.

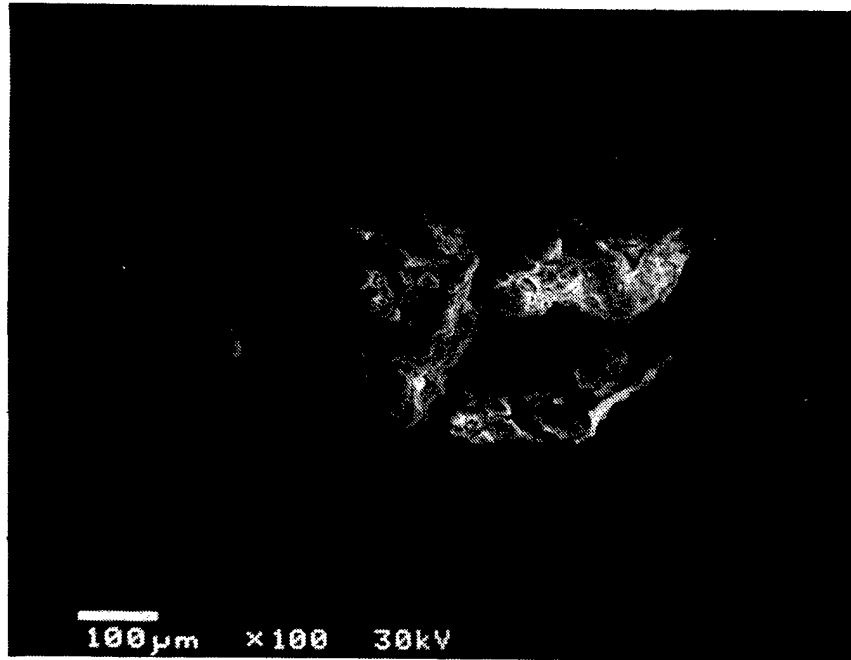


Figure 19: Particulate Material Contained in ARCO SiC Whiskers

Whiskers were separated with a minimum of 98.8% of the material being recovered after separation. Table 8 shows the average length and relative amounts in each section (top, middle, and bottom) for a typical separation, using a settling time which would allow particles with a 10- $\mu$ m radius or larger to settle to the bottom of the column. It was not anticipated that whiskers could be sharply separated by size using such a column. Approximately 70% (middle section) of the starting material was deemed of appropriate quality for composite fabrication.

Table 8. Average whisker lengths and relative amounts obtained from separated column levels

Material	Average Whisker Length ( $\mu$ m) After Separation			
	As-Received	Top	Middle	Bottom
ARCO (SC-9)	17.5 $\pm$ 12.6	19.0 $\pm$ 8.7	17.5 $\pm$ 9.5	29.3 $\pm$ 14.5
Relative Amounts of Whiskers (%) After Separation				
		Top	Middle	Bottom
ARCO (SC-9)		29.7	68.3	1.9

Initial composite powders were prepared by simple dry mixing of preprocessed  $\text{Si}_3\text{N}_4$  + 6 w/o  $\text{Y}_2\text{O}_3$  + 1.5 w/o  $\text{Al}_2\text{O}_3$  with the as-received SiC whiskers. Microstructural observation of polished sections from hot pressed samples showed poor dispersion of the whiskers. To obtain better whisker dispersion, the processing route previously described was used. This process produced excellent dispersion in the hot pressed composite (Figure 20).

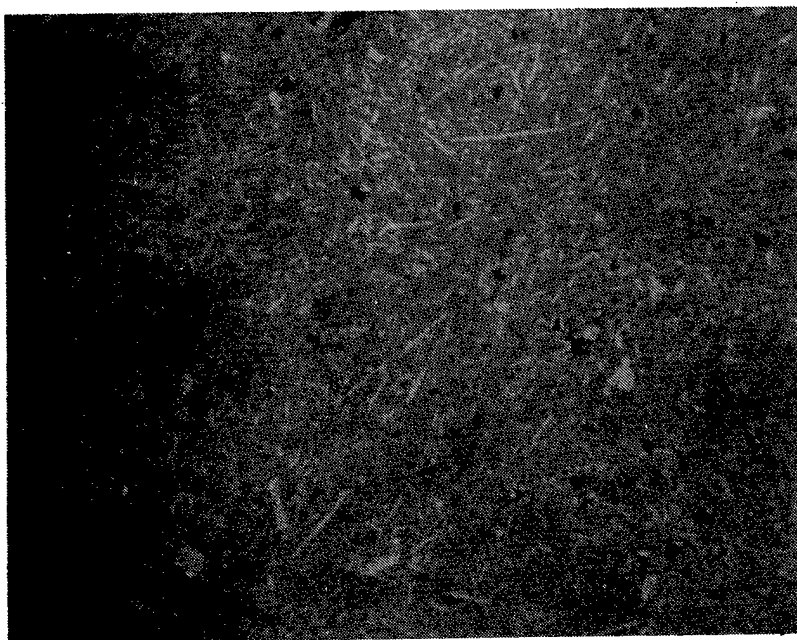


Figure 20: Microstructure of  $\text{Si}_3\text{N}_4$  (AY6)-20 v/o SiC Whisker Composites

To determine the extent of damage to the SiC whiskers during processing, whiskers or whisker/powder mixtures were sampled after different process steps, and the lengths were determined from SEM photomicrographs. Table 9 gives the results of whisker length measurements and the resultant whisker aspect ratio ( $L/D$ ) at various process steps. As-received whiskers have an average diameter of  $0.53 \pm 0.19 \mu\text{m}$ .

Testing after homogenization, which is the harshest processing step, shows the SiC whisker lengths reduced by a factor of  $\approx 3$ . Examination of the whisker lengths from a fully dense hot-pressed sample confirms the observation and indicates that limited decrease in lengths may be occurring during hot pressing.

The mechanical properties of composites containing 30 v/o of as-received SiC whiskers are given in Table 10. As can be seen, the application of as-received whiskers results in a  $\approx 20\%$  reduced MOR, despite up to 40% increased fracture toughness over that of base AY6 material.

Table 9. Characterization of SiC whisker lengths after various process steps

Processing Step	Average Length ( $\mu\text{m}$ )/ No. of Whisker Counted	Aspect Ratio
As-Received	$17.5 \pm 12.0/1574$	33
After Sedimentation	$17.5 \pm 9.4/1430$	33
After Homogenization	$5 \pm 3/1439$	10
Hot-Pressed Composite	$6 \pm 3/1180$	12

Table 10. Mechanical properties comparison of  $\text{Si}_3\text{N}_4$  (AY6)-30 v/o SiC whisker composites containing As-received or separated whiskers

Material	$K_{IC}$ ( $\text{MPa} \cdot \text{m}^{1/2}$ )	MOR (MPa)	Calculated Flaw Size ( $\mu\text{m}$ )
As-Received	$6.0 \pm 0.1$	$597 \pm 5$	65
Separated	$6.4 \pm 0.5$	$975 \pm 39$	28
AY6 Monolith	$4.7 \pm 0.3$	$773 \pm 67$	24

Based on these results, whisker beneficiation by water column separation was incorporated in the process to fabricate composites.

**Densification.** The densification rates of the  $\text{Si}_3\text{N}_4$ -based materials were found to be affected by additions of SiC whisker dispersoids. Increasing contents of SiC whiskers were observed to decrease the densification rates of the composites relative to monolithic  $\text{Si}_3\text{N}_4$ ; composite materials therefore required extended times to achieve full density.

To observe the differences in densification rates, the ram travel during hot pressing was recorded as a function of time using a dial gauge, and these data were converted to relative density. Time zero for the plots in Figure 21 indicates the time when maximum temperature was reached. The end-point criterion for each run was a decrease in compaction rate to  $2 \times 10^{-4}$  cm/min of ram travel, which from experience has been found to yield high density ( $> 99\%$  of calculated theoretical) for  $\text{Si}_3\text{N}_4$ -based ceramics.

**Fracture Strength and Toughness.** The room-temperature fracture toughness, measured by the controlled surface flaw technique of  $\text{Si}_3\text{N}_4$ -SiC whisker composites densified by the schedules shown in Figure 21, is presented in Figure 22. Elastic prop-

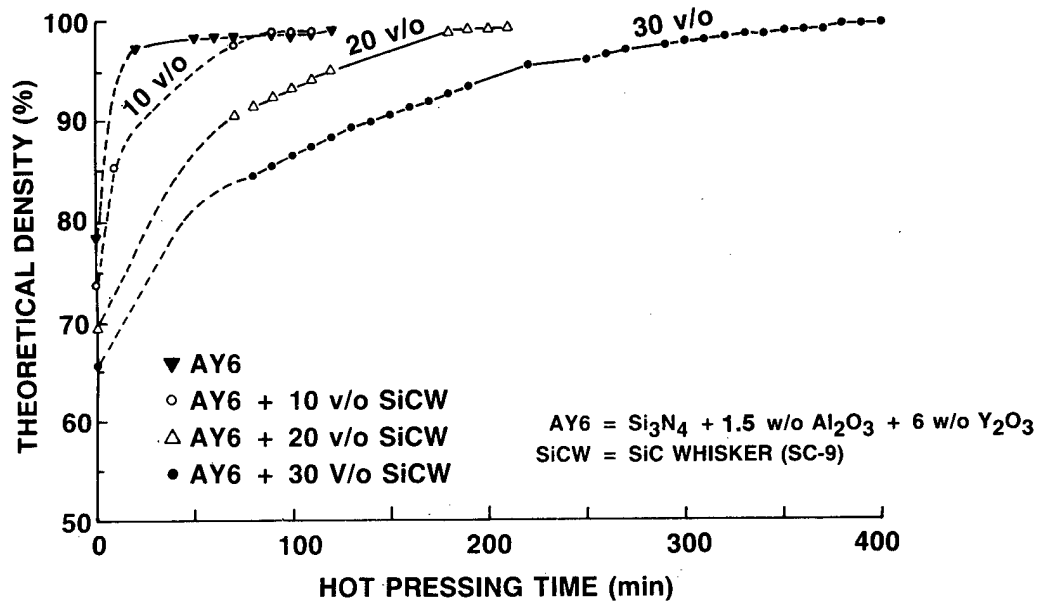


Figure 21: Densification of  $\text{Si}_3\text{N}_4$  (AY6)-Based Ceramics

erty measurements of selected materials indicated an insignificant degree of anisotropy and a slight increase in Young's modulus, resulting from dispersoid additions (Table 11). The fracture toughness increased to a value of  $6.4 \pm 0.5 \text{ MPa}\cdot\text{m}^{1/2}$  for the composite containing 30 v/o SiC whiskers. This represents an approximate 40% increase in  $K_{\text{IC}}$  for this composite, compared to the monolith. Figure 23 compares the fracture surfaces of the  $\text{Si}_3\text{N}_4$  and a 30 v/o SiC whisker composite broken at room temperature. Numerous depressions caused by fracture around the whiskers and occasional whisker cavities and protruding whiskers are indications that crack deflection and limited whisker pullout may contribute to toughening. Additions of whiskers above 30 v/o further increase the difficulties in both whisker dispersion and densification. Nevertheless, at the level of 35 v/o a fracture toughness of  $8.3 \pm 0.7$  (75% increase) was obtained. Modulus of rupture of this composite was equivalent to that of the baseline (AY6) monolith.

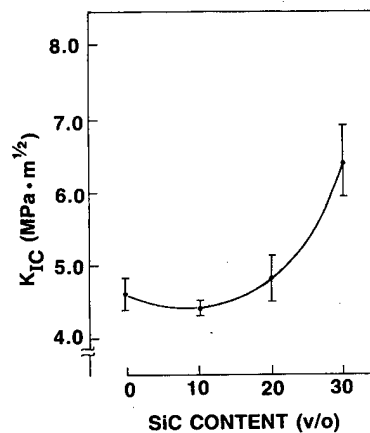


Figure 22: Room-Temperature Fracture Toughness of  $\text{Si}_3\text{N}_4$  (AY6)-SiC Whisker Composites

Table 11. Elastic constants for  $\text{Si}_3\text{N}_4$  (AY6) and  $\text{Si}_3\text{N}_4$  (AY6)-SiC whisker composites

Material	Young's Modulus (GPa)		Poisson's Ratio	Shear Modulus (GPa)	Bulk Modulus (GPa)
	Par*	Per**			
AY6	297	299	0.27	116	218
AY6 + 10 SiCw	311	—	0.28	123	228
AY6 + 20 SiCw	311	325	0.26	127	223
AY6 + 30 SiCw	333	340	0.26	113	234

\* Par – measured in plane parallel to hot-pressed direction

\*\* Per – measured in plane perpendicular to hot-pressed direction

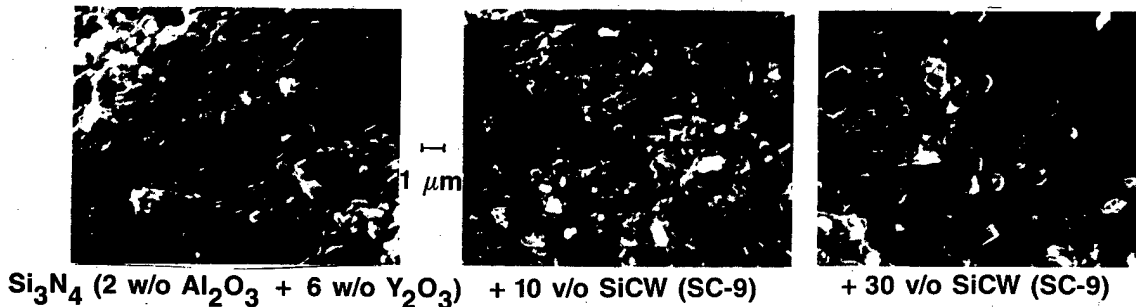


Figure 23. Fracture Surfaces of  $\text{Si}_3\text{N}_4$  (AY6)-Based Ceramics Broken at Room Temperature

The room temperature strength of the 30 v/o whisker composite increased by 25 % compared to the base monolith (Figure 24). Although increased fracture toughness and strength have been reported for SiC whisker additions to alumina and mullite,<sup>13</sup> reported results for SiC whisker additions to  $\text{Si}_3\text{N}_4$  have shown increases in fracture toughness and decreases in modulus of rupture, which were attributed to large processing flaws, some of which were whisker-related, and microcracking at tips of SiC whiskers.<sup>14</sup> The results of the present study illustrate that simultaneous increases in strength and fracture toughness can be achieved. Higher strength is generally observed at room as well as elevated temperatures (Figure 25). Fractography of samples broken at high temperature again showed evidence of both crack deflection and whisker pullout. A change in the degree of the pullout contribution to property enhancement at elevated temperature was not evident.

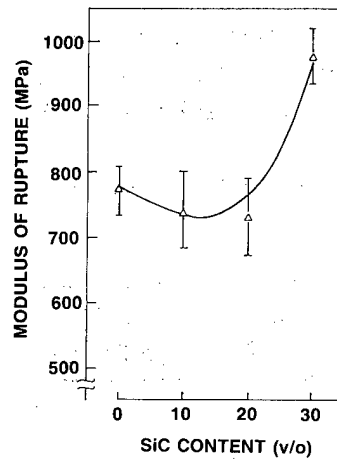


Figure 24. Room-Temperature Modulus of Rupture of  $\text{Si}_3\text{N}_4$  (AY6)-SiC Whisker Composites

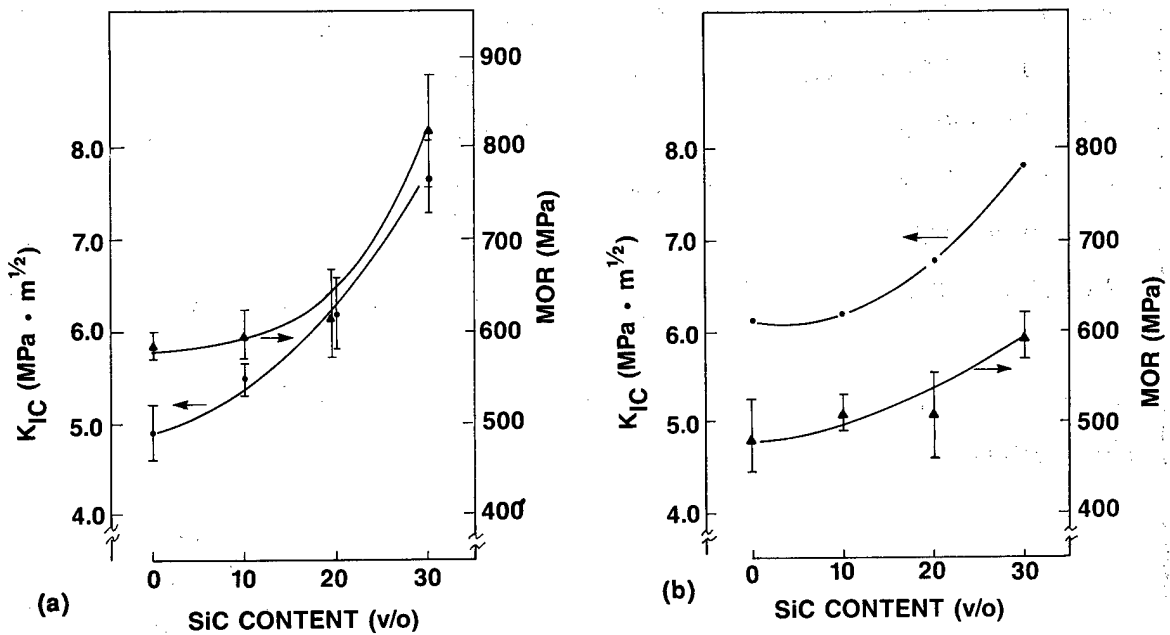


Figure 25. Fracture Toughness ( $K_{IC}$ ) and Modulus of Rupture (MOR) of  $\text{Si}_3\text{N}_4$  (AY6)-SiC Whisker Composites at (a) 1000°C and (b) 1200°C

In order to assess the anisotropy of mechanical properties of the hot-pressed ceramics, indentation fracture toughness was measured both parallel and perpendicular to the hot-pressing axes in a plane parallel to the hot-pressing direction and in two directions 90° from each other in a plane perpendicular to the hot-pressing direction.

The results (Table 12) indicate that anisotropy in fracture toughness exists for all hot-pressed materials. The IFT in a plane perpendicular to the hot-pressing direction

was lower in all cases than that measured parallel to the hot-pressing direction. For the whisker-containing composites, the degree of anisotropy increased with increasing whisker content, due to whisker and acicular  $\text{Si}_3\text{N}_4$  grain alignment.

Table 12. Indentation fracture toughness anisotropy in hot-pressed silicon nitride-based ceramics

	Plane IFT	$\parallel$ HPD ( $\text{MPa} \cdot \text{m}^{1/2}$ )	Plane IFT	$\perp$ HPD ( $\text{MPa} \cdot \text{m}^{1/2}$ )
	Direction			
Material	$\parallel$ HPD (1)	$\perp$ HPD (2)	(3)	(4)
AY6 (90 min)	$4.1 \pm 0.2$	$3.4 \pm 0.2$	$3.6 \pm 0.2$	$3.7 \pm 0.2$
AY6-10 v/o SiCp <sup>x</sup> (8 $\mu\text{m}$ )	$3.9 \pm 0.3$	$3.2 \pm 0.2$	$3.8 \pm 0.2$	$3.8 \pm 0.2$
AY6-20 v/o SiCp (8 $\mu\text{m}$ )	$4.1 \pm 0.2$	$3.0 \pm 0.1$	$3.8 \pm 0.2$	$3.8 \pm 0.2$
AY6-30 v/o SiCp (8 $\mu\text{m}$ )	$3.7 \pm 0.2$	$3.0 \pm 0.2$	$4.0 \pm 0.2$	$4.0 \pm 0.2$
AY6-10 v/o SiCw <sup>xx</sup>	$3.7 \pm 0.2$	$3.5 \pm 0.1$	$3.8 \pm 0.1$	$3.5 \pm 0.2$
AY6-20 v/o SiCw	$4.0 \pm 0.1$	$2.9 \pm 0.3$	$3.8 \pm 0.1$	$3.6 \pm 0.2$
AY6-30 v/o SiCw	$4.8 \pm 0.2$	$3.0 \pm 0.2$	$4.7 \pm 0.2$	$4.6 \pm 0.2$

p<sup>x</sup> = Particulate  
w<sup>xx</sup> = Whisker

Figure 26 illustrates the indentation-induced crack interactions with the whiskers on planes parallel and perpendicular to the hot-pressing direction. Due to whisker alignment, the degree of deflection around whiskers is higher in the parallel plane. Pullout (bridging) is observed in this plane, whereas this phenomenon is rarely observed in the perpendicular plane, since the whisker alignment virtually precludes the possibility of this toughening mechanism occurring in this orientation.



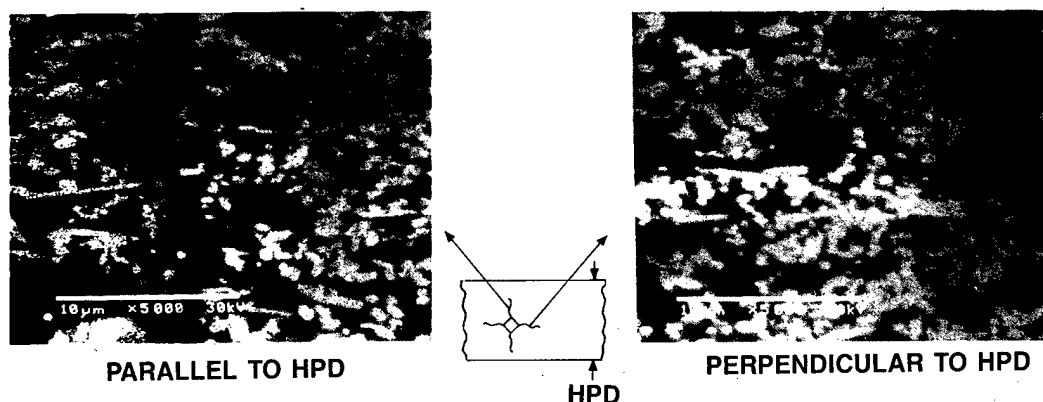


Figure 26. Indentation-Induced Crack Propagation

In order to examine the interdependence of microstructures and properties of the matrix material in this study, the base monolithic  $\text{Si}_3\text{N}_4$  composition was hot pressed for an extended time to promote grain growth. This microstructural modification resulted in an increase in the room-temperature fracture toughness from  $4.7 \pm 0.3 \text{ MPa}\cdot\text{m}^{1/2}$  to  $5.4 \pm 0.5 \text{ MPa}\cdot\text{m}^{1/2}$ , with a concomitant increase in modulus of rupture from  $773 \pm 67 \text{ MPa}$  to  $896 \pm 29 \text{ MPa}$  for the monoliths hot pressed for 90 minutes and 400 minutes, respectively. The increased time at densification temperature resulted in growth of the  $\beta\text{-Si}_3\text{N}_4$  grains, as indicated by observing surfaces of MOR bars broken at room temperature (Figure 27), which produced increased  $K_{IC}$  and MOR.

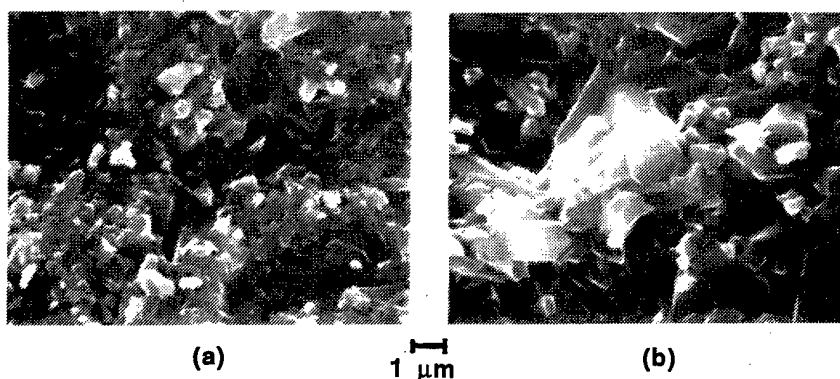


Figure 27. Fracture Surface of Silicon Nitride Base Material Held at Sintering Temperature for (a) 90 min and (b) 400 min

As with the monolithic  $\text{Si}_3\text{N}_4$ , variations in the densification parameters (Figure 21) of the composites are anticipated to result in differences in matrix microstructures and hence mechanical properties. It follows that the resultant matrix microstructures of the densified composites may not be identical in grain size distribution. Hence, the toughening behavior observed through whisker additions would not be expected to be a singular function such as that based on models which assume a homogenous continuum matrix. The observed functional dependence consists of individual points on a family of toughening curves, each point depending on the microstructure of the

individual composite matrix, since the degree of toughening achieved with a whisker dispersoid is dependent upon its size relative to the polycrystalline matrix grain size.

To test the proposed behavior, two sets of  $\text{Si}_3\text{N}_4$ -(0-30) v/o SiC whisker composites were hot pressed at the same temperature using two densification schedules. The first schedule was based on the shortest time necessary to achieve a complete  $\alpha$ - $\beta$   $\text{Si}_3\text{N}_4$  conversion and  $\approx 100\%$  theoretical density. The second one was to extend time to 400 min for each composition to provide the equivalent conditions for  $\text{Si}_3\text{N}_4$  grain growth. The resulting microstructures were examined by quantitative metallographic analysis, and the  $\text{Si}_3\text{N}_4$  grain size and distribution determined from STEM micrographs at 25,000X magnification. Figure 28 gives an example of  $\text{Si}_3\text{N}_4$  + 20 v/o SiC whisker microstructure and  $\text{Si}_3\text{N}_4$  grain size distribution for composites hot pressed for 210 min and 400 min. Table 13 contains the quantitative metallographic analysis on all examined composites and the associated fracture toughness values.

Table 13. Grain size and fracture toughness data of  $\text{Si}_3\text{N}_4$  (AY6)-SiC whisker composites

Material	Hot-Pressing	$\text{Si}_3\text{N}_4$ Grain *		$K_{IC}$ ( $\text{MPa} \cdot \text{m}^{1/2}$ )
	Time (min)	Size ( $\mu\text{m}$ )	$\pm \sigma_n^D$	
AY6	90	0.37	0.27	$4.7 \pm 0.3$
AY6	400	0.59	0.41	$5.4 \pm 0.5$
AY6-10 v/o SiCw	110	0.36	0.24	$4.4 \pm 0.1$
AY6-10 v/o SiCw	400	0.47	0.30	$6.0 \pm 0.1$
AY6-20 v/o SiCw	210	0.24	0.14	$4.8 \pm 0.3$
AY6-20 v/o SiCw	400	0.49	0.32	$5.9 \pm 0.8$
AY6-30 v/o SiCw	400	0.36	0.24	$6.4 \pm 0.5$

\*Equivalent diameter

\*\*Controlled surface flaw technique

Figure 29 and Table 13 show that an increased fracture toughness of composites hot pressed for 400 min is clearly due to the combined effect of a well-developed matrix microstructure and the additional toughening effect of SiC whiskers. In order to assess the applicability of the proposed relationship between the grain size and the resulting composite fracture toughness to predict an expected composite fracture toughness using the microstructural parameters, the  $K_{IC}$  of the composites listed in Table 13 were calculated using equation (7) for all seven compositions. Figure 29 indicates that the dependence resulting from using the calculated  $K_{IC}$  values (the dashed lines) approximates to a substantial degree the one based on actual measurements, despite the assumption that both matrix and whisker dispersoid grains are equiaxed. Although

the average SiC whisker aspect ratio is 6.0 in the hot-pressed composites, the average SiC equivalent grain diameter  $\bar{D}_{\text{SiC}} = 1.95 \mu\text{m}$  was used in the calculations.

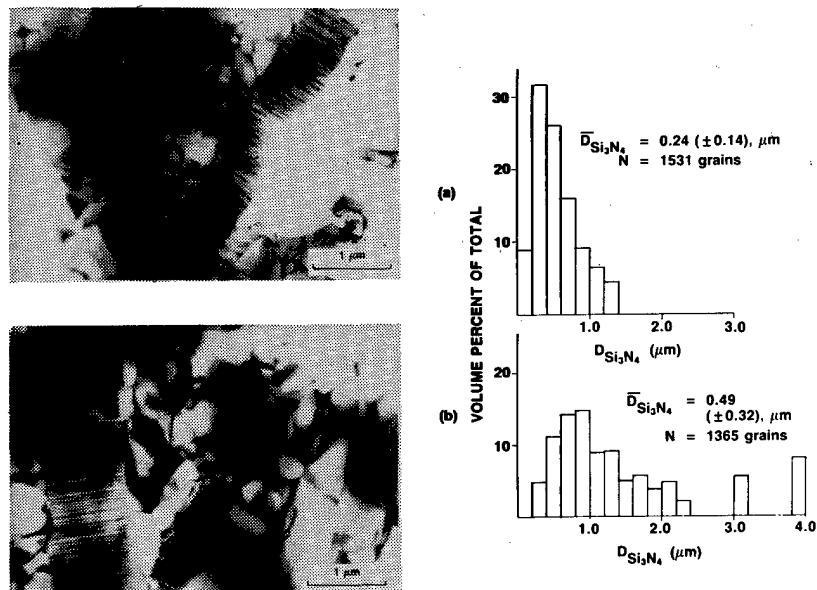


Figure 28. TEM Bright Field Images and the Si<sub>3</sub>N<sub>4</sub> Grain Size (Equivalent Diameter) Distributions in the Si<sub>3</sub>N<sub>4</sub>-20 v/o SiC Whisker Composites Hot Pressed for (a) 210 min and (b) 400 min

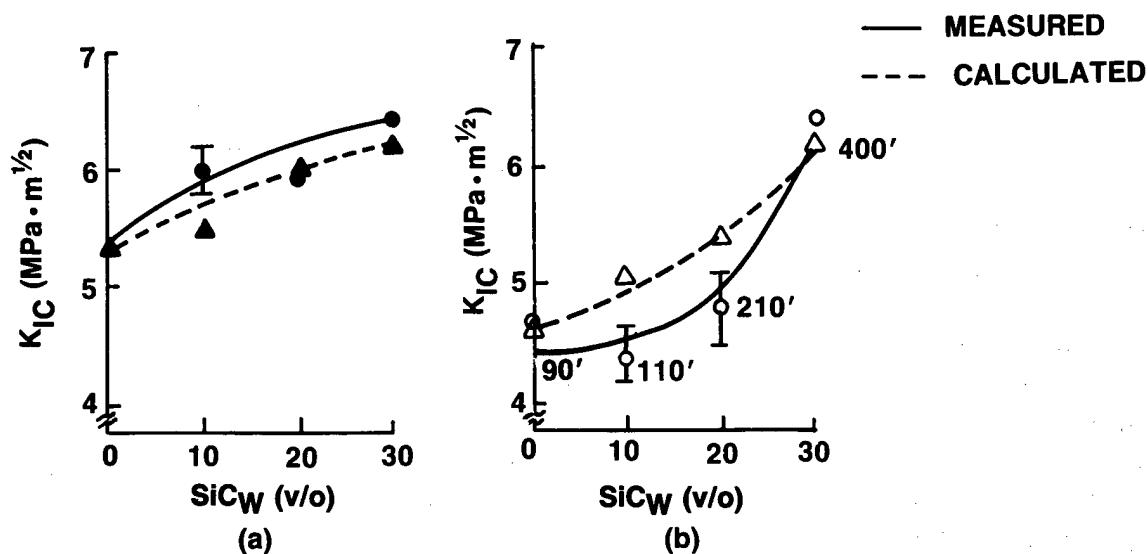


Figure 29. Comparison Between the Measured and Calculated  $K_{\text{IC}}$  Values vs SiC Content for AY6-(0-30) v/o SiC Whisker Composites Hot Pressed for (a) 400 min HP and (b) Minimum Time to Full Density

Based on these observations, it is apparent that in the case of discontinuous composites that fracture in an intergranular mode, the matrix grain size influences the choice of the dispersoid size and, therefore, the relationship between these two should be taken into consideration.

The actual shape distribution of  $\text{Si}_3\text{N}_4$  grains in AY6-20 v/o SiC hot pressed for 210 min and 400 min was evaluated using quantitative microscopy and is shown in Figure 30. The form factor varies between zero and 1.0, with  $F = 1.0$  corresponding to an equiaxed or circular grain shape and  $0.0 < F < 1.0$  describing a deviation from an equiaxed (spherical) toward more elongated shapes. The average aspect ratio for  $\text{Si}_3\text{N}_4$  grains calculated using the data from Figures 28 and 30 was  $\ell/d = 1.5$  in the 210 min specimen and  $\ell/d = 1.8$  in the 400 min specimen. These data indicate that the  $\text{Si}_3\text{N}_4$  grain growth rate is rather slow, that the grain growth is, for the most part, planar, and that the  $\text{Si}_3\text{N}_4$  grain aspect ratio is maintained at a low and constant level, independent of sintering time.

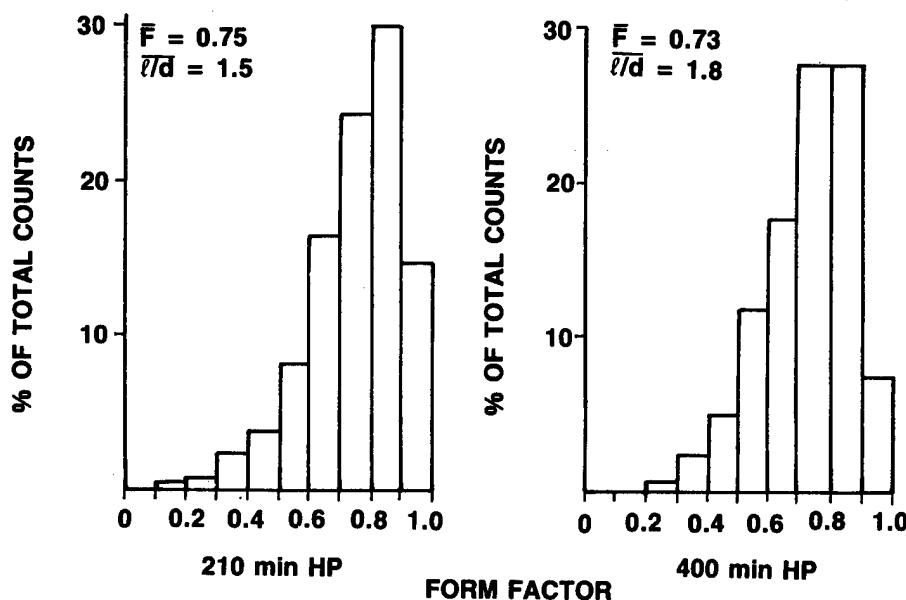


Figure 30. Shape Distribution of  $\text{Si}_3\text{N}_4$  Grains in AY6-20 v/o SiC Whisker Composites Hot Pressed for (a) 210 min and (b) 400 min

**Fracture Toughness-Crack Length Dependence.** Mechanical property characterization of silicon nitride-based ceramics also addressed the issue of potential rising R-curve behavior for composites containing SiC whiskers. MOR bars of monolithic AY6 and an AY6 + 30 v/o SiC whisker (ARCO SC-9) composite were indented with a single Vickers indentation. The indentation load was varied from 10 to 500 N and the test bars annealed in argon at 1200 °C for one hour to relieve the residual strain produced by the indentation process. The bars were broken in four-point loading at a crosshead rate of 0.05 cm/min. Figure 31 is a plot of log MOR versus log indentation load. Both materials show linear decreases in log MOR as log load increases. Linear regression analysis of the data yields slopes of  $-0.3334$  for AY6 and  $-0.3612$  for the composite. Materials which exhibit a fracture toughness which is independent of crack exten-

sion have a slope of  $-1/3$  for this type of plot. Fracture toughness of both materials is, within the limits of indentation cracks produced, independent of crack size.

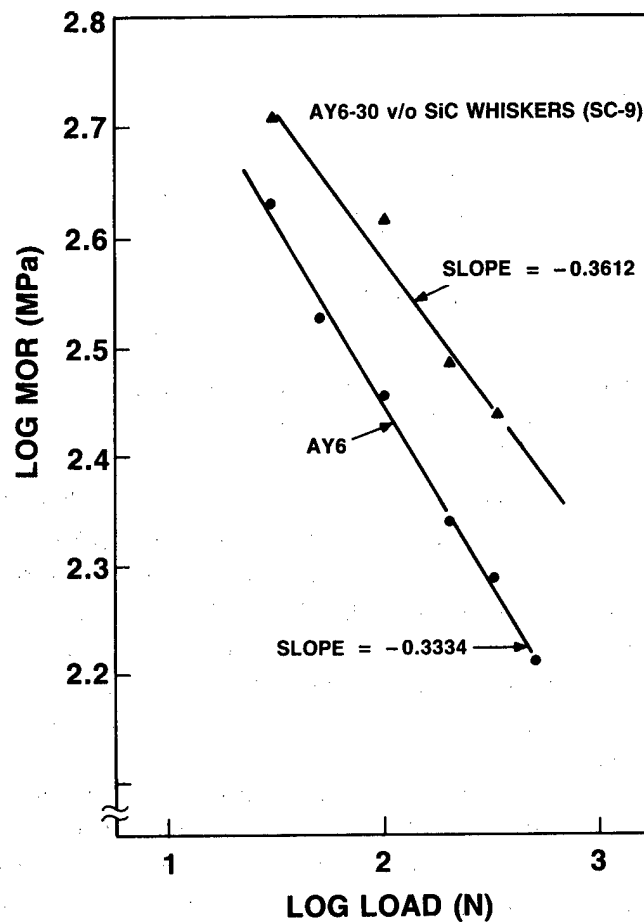


Figure 31. Modulus of Rupture of AY6-Si<sub>3</sub>N<sub>4</sub> Monolith and 30 v/o SiC Whisker Composite with Vickers Indentations Produced at Various Loads

**Slow Crack Growth and Creep Resistance.** Figure 32 compares the strength from room temperature to 1400°C of two AY6 materials densified as described above to an AY6-30 v/o SiC whisker (ARCO SC-9) composite which required 400 minutes to densify. The AY6 material hot pressed for 400 minutes retains its higher strength compared to AY6 produced by standard process up to 1200°C. Both monolithic ceramics exhibit lower values of strength compared to the composite reinforced with 30 v/o SiC whiskers. The data at higher temperatures ( $\geq 1200^\circ\text{C}$ ) show these two monolithic materials to be essentially equivalent in strength. In this temperature regime, the softened intergranular glass phase controls the mechanical properties. Fractographic analysis has shown that at these higher temperatures subcritical crack growth related to intergranular glass phase viscosity occurs and results in strength degradation.

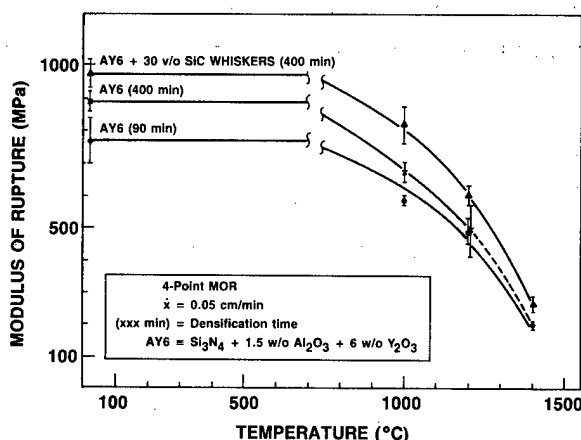


Figure 32. Modulus of Rupture of  $\text{Si}_3\text{N}_4$  (AY6) Ceramics and  $\text{Si}_3\text{N}_4$  (AY6) + 30 v/o SiC Whisker Composite up to 1400 °C

As shown in Figure 32, the strength improvement by SiC whisker reinforcement is retained up to 1400 °C under the fast fracture conditions imposed by the MOR test. The increased strength at the higher temperatures appears to be related to an increased resistance to subcritical crack growth of the composite. Fractography of controlled flaw samples broken at 1200 °C showed an increase in crack depth of 82 % and half crack length of 229 % prior to fast fracture for the AY6 material hot pressed for 90 minutes. The respective increases for the AY6-30 v/o SiC whisker composite under the same conditions were 60 % and 156 %.

Four-point creep tests (ambient air atmosphere) were conducted to compare monolithic AY6 to an AY6 + 30 v/o SiC whisker composite. Figure 33a compares the strain-time relationships at 1200 °C, 30 ksi applied stress of AY6 to the composite. This whisker-containing composite had appreciably higher resistance to creep under these conditions compared to the monolith. One AY6 bar exhibited substantial subcritical crack growth, as opposed to the expected grain boundary sliding controlled creep. This crack growth was observed to be initiated from a grinding flaw in the chamfer. The conditions of this test are in a regime where creep and crack growth from existing flaws are competitive mechanisms of failure for  $\text{Si}_3\text{N}_4$ . To further evaluate these phenomena, test bars of both materials were precracked with 100 N Knoop indentations, which produces a surface flaw of approximately 125  $\mu\text{m}$  in depth. The samples were then annealed at 1200 °C in argon to relieve indentation stresses and subsequently creep tested at 1200 °C/30 ksi. The indented AY6 bar fractured 20 minutes after the test load was applied, while the indented SiC whisker-containing composites showed essentially the same steady state creep rate as had been measured for the unindented composite (Figure 33b). These data again indicate that the addition of SiC whiskers to  $\text{Si}_3\text{N}_4$  decreases the material's susceptibility to slow crack growth and demonstrates that the flaw sensitivity of the composite is greatly reduced under operating conditions which may be encountered in heat engine applications.

The effect of dispersoid morphology was also evaluated (Figure 33c). The resistance to creep of AY6 was appreciably reduced by the addition of 30 v/o SiC particulates ( $\approx 8 \mu\text{m}$ ). The effect is thought to be due to the substitution of equiaxed SiC particles for acicular  $\beta\text{-Si}_3\text{N}_4$  grains, which should enhance grain boundary sliding. Figure 33d compares results for AY6 and the SiC whisker composite at  $1200^\circ\text{C}/30 \text{ ksi}$  to those obtained for the composite at  $1200^\circ\text{C}/40 \text{ ksi}$ . The creep rate of the composite at the higher stress is equivalent to that of the monolith at the lower stress. These results indicate that at  $1200^\circ\text{C}$  the AY6 + 30 v/o SiC whisker composite can be subjected to 30% higher stress than the monolith, at which point both have equivalent resistance to creep.

The results of compressive creep studies conducted in collaboration with North Carolina State University<sup>22</sup> on 20 v/o SiC(w) composite have shown that, although the fast fracture strength is increased at  $1200^\circ\text{C}$  and above by whisker additions, under conditions of low compression strain rate, the steady state creep resistance of the monolith and composite are essentially the same at  $1200^\circ\text{C}$ , while the composite creeps faster at  $1250^\circ\text{C}$  (Figure 34). This behavior under compressive creep conditions has been attributed to an increased stability of the intergranular glass phase of the composite due to impurities contained in the ARCO SC-9 whiskers, which reduces its tendency to crystallize. Under the conditions employed in this testing, a four-hour anneal at the test temperature prior to test initiation, the monolithic AY6 was shown by TEM to contain a much larger percentage of devitrified glass phase compared to the composite. Hence, initially at  $1250^\circ\text{C}$  (1520 K) the composite exhibited a higher creep rate. This may also be related to whisker orientation effects, since compressive load was applied parallel to the hot-pressing direction, i.e., perpendicular to the plane in which whiskers are preferentially aligned. TEM analyses of tested specimens have indicated that the glass phase of the composite continues to devitrify during testing.

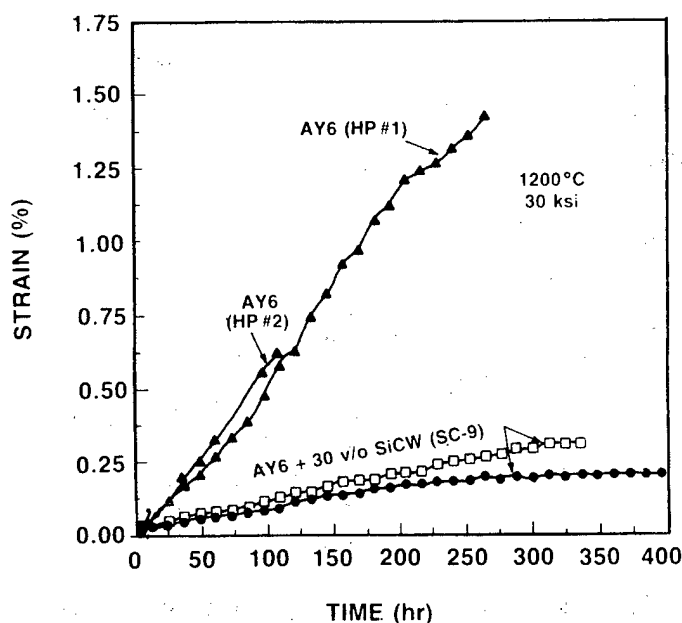


Figure 33a. Results of Four-Point Creep Evaluation for Monolithic  $\text{Si}_3\text{N}_4$  (AY6) and  $\text{Si}_3\text{N}_4$  (AY6) - 30 v/o SiCw Composite

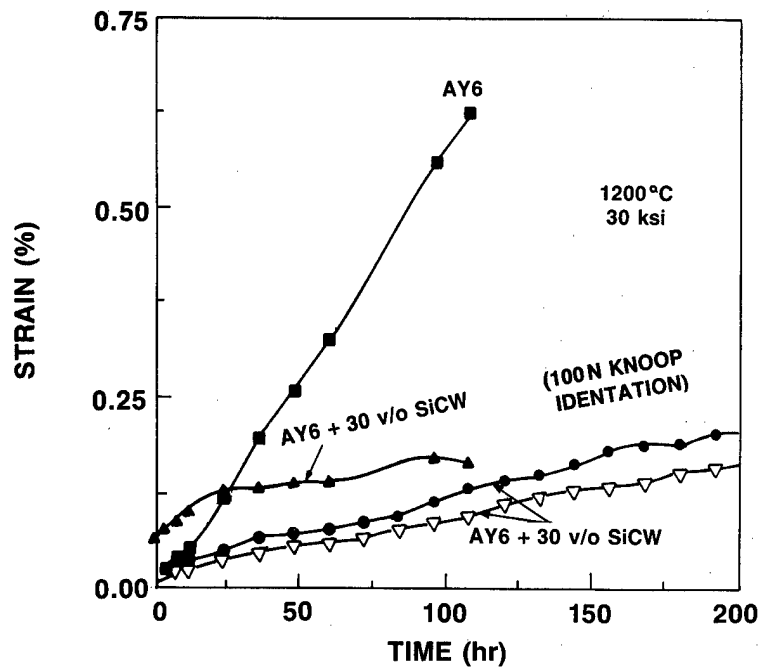


Figure 33b. Comparison of  $\text{Si}_3\text{N}_4$  (AY6) and  $\text{Si}_3\text{N}_4$  (AY6)-30 v/o SiCw Composite and Precracked Composite in Four-Point Creep

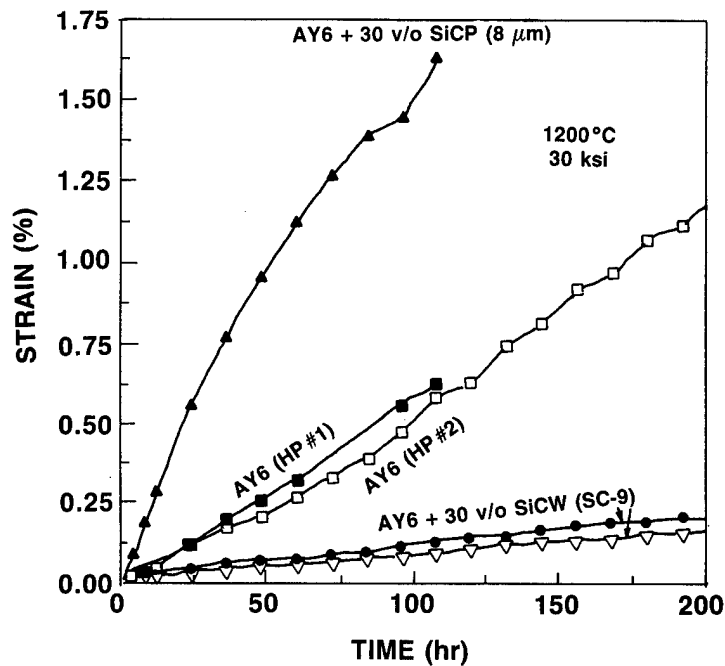


Figure 33c. Effect of SiC Dispersoid Morphology Equiaxed Particle (p) vs Whisker (w) on the Creep of  $\text{Si}_3\text{N}_4$  (AY6)-Based Materials



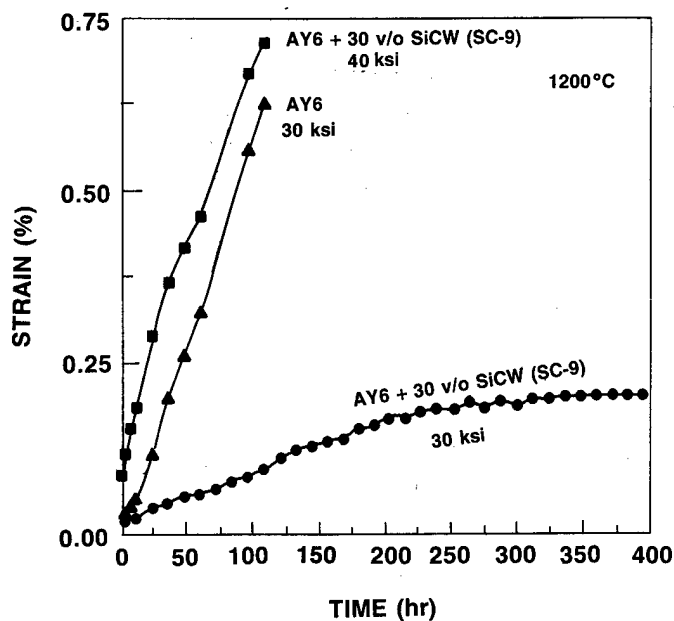


Figure 33d. Four-Point Creep at 1200°C of  $\text{Si}_3\text{N}_4$  (AY6) and  $\text{Si}_3\text{N}_4$  (AY6)-30 v/o SiC Whisker Composite

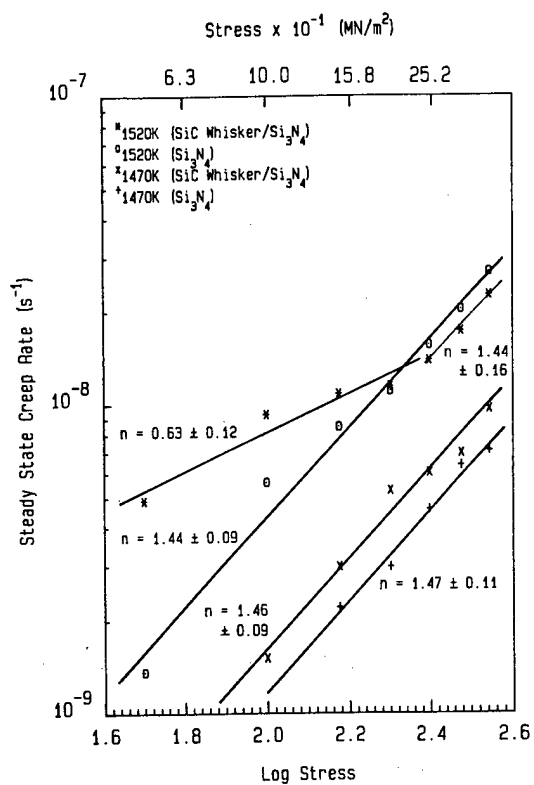


Figure 34. Steady State Compressive Creep Test of  $\text{Si}_3\text{N}_4$  (AY6) and a  $\text{Si}_3\text{N}_4$  (AY6) - 30 v/o SiC Whisker Composite (after R.D. Nixon, et al.)

**Oxidation Resistance.** The oxidation of an AY6 + 30 v/o SiC whisker composite was evaluated relative to standard hot-pressed AY6 ( $\text{Si}_3\text{N}_4$  + 6 w/o  $\text{Y}_2\text{O}_3$  + 1.5 w/o  $\text{Al}_2\text{O}_3$ ) up to 1000 hours of exposure to ambient air at 1200°C. The results (Figure 35) show that the long-term (>500 hour) oxidation resistance of the composite is equivalent to AY6. The small difference is most likely related to dilution of the ( $\text{Al}_2\text{O}_3$  +  $\text{Y}_2\text{O}_3$ ) sintering aid by substitution of SiC for the blended AY6 powder. The data show that the oxidation of AY6 was not adversely affected by the addition of ARCO SC-9 SiC whiskers.

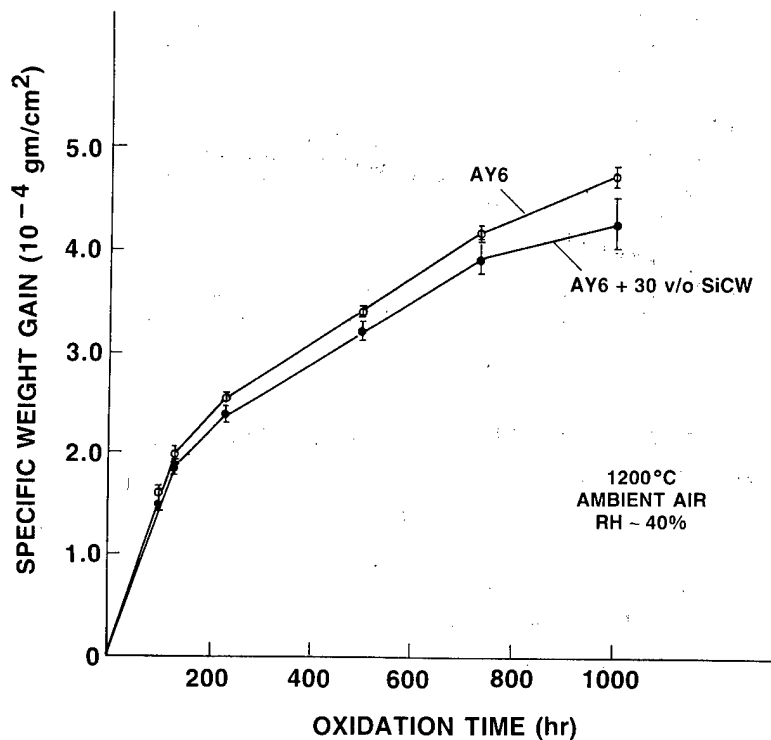


Figure 35. Ambient Atmosphere Oxidation at 1200°C of  $\text{Si}_3\text{N}_4$  (AY6) and an  $\text{Si}_3\text{N}_4$  (AY6) + 30 v/o SiCw (SC-9) Composite

The study of oxidation resistance of AY6 and AY6-SiC whisker composites was supplemented by the examination of the oxide scales formed after 200 hours of oxidation in air at 1200°C. Using Auger Electron Spectroscopy (AES) and x-ray diffraction (XRD) phase analysis, the oxidation products were examined while attached and after being mechanically separated from the bar surface. The oxide scale thickness, as determined by AES, was found to be  $\approx 2 \mu\text{m}$  for both materials. The elemental profiles through the oxidation layers (Figure 36) show that in either material the scale is composed of two distinct sublayers. The outermost layer was found to be yttrium-enriched to a thickness of  $\approx 1500 \text{ nm}$  ( $1.5 \mu\text{m}$ ). Below this layer the yttrium signal gradually decreases to the background level. The oxide layer on the AY6-SiC(w) specimen revealed the presence of carbon and calcium throughout the entire layer. However, beyond the oxide-ceramic interface the calcium signal drops to almost zero, while the carbon increases considerably and then levels off. Neither carbon nor calcium

was detected in the AY6 specimen. Examination of the Si peak energy position and the peak shape in the AY6-30 v/o SiCw specimen has indicated a complete Si-O bonding in the outermost oxide layer (60 nm into the layer), a mixed Si-O, Si-C, and Si-N state in the middle of the layer (960 nm), and a predominantly unoxidized Si-N and Si-C bonding in the bulk of the specimen (2410 nm  $\approx$  2.4  $\mu$ m into the specimen).

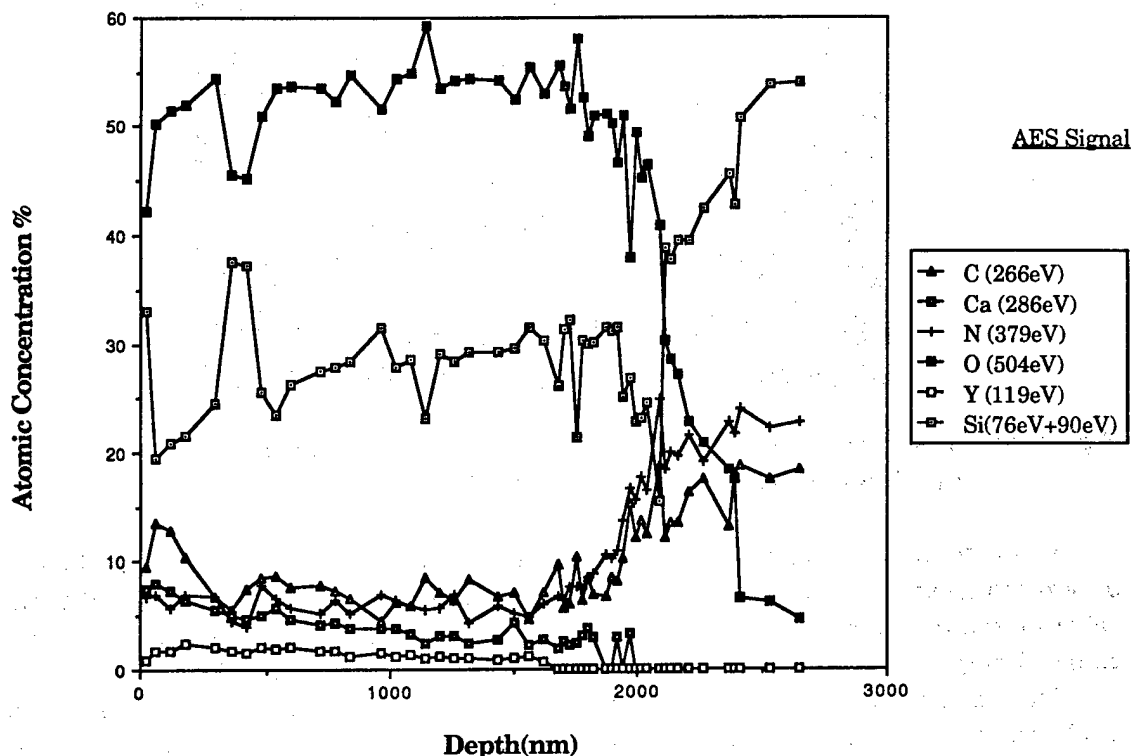


Figure 36. Auger Elemental Profiles Through the Oxide Scale Formed on the  $\text{Si}_3\text{N}_4$  (AY6)-30 v/o SiC Whisker Composite After 200 hr Oxidation in Static Air at 1200°C

The phase composition of the oxide deposits, as determined by the XRD phase analysis, was similar for both specimens in that the  $\gamma\text{-Y}_2\text{Si}_2\text{O}_7$  was the major and  $\text{SiO}_2$ -low quartz the minor phase identified. A yttrium enrichment of the outermost layers in both specimen scales, coupled with the  $\text{Y}_2\text{Si}_2\text{O}_7$  found by XRD, points out that needle-like crystals of yttrium silicate form as a result of devitrification of glass in the near surface region (Figure 37).

Calcium detected in the scale on the AY6-SiCw composite apparently did not form any crystalline compounds under the employed heating and cooling conditions. The changes in the position and shape of the silicon peak through the scale depth indicate continuous change in the phase composition of the oxidation products. The carbon profile through the oxide layer and into unoxidized composite with a low but steady signal in the scale and a considerable signal increase in the substrate ceramic, together with the XRD results showing a relative increase in  $\beta\text{-SiC}$  reflections with increasing oxidation time, suggests that the hexagonal form of SiC is more susceptible to oxidation than the  $\beta$ -cubic. Finally, the oxidation layer thickness measured by AES was found

to be identical on both the monolith and the composite specimens, which is consistent with the results on weight gain during oxidation reported earlier.

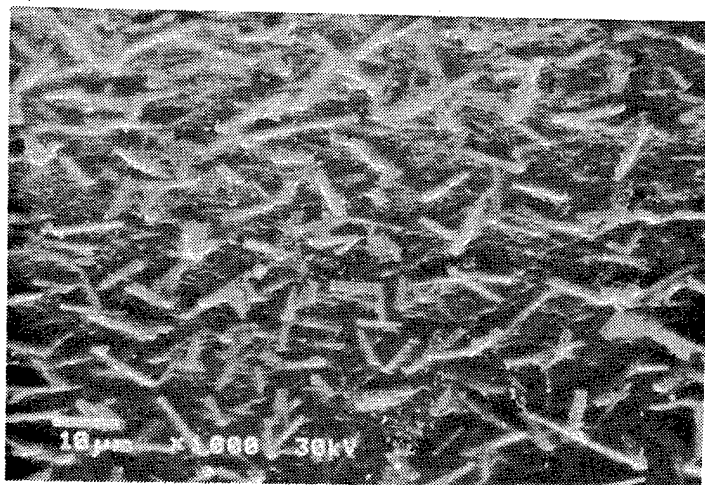


Figure 37. SEM Photomicrograph of the Oxidized Surface Layer of  $\text{Si}_3\text{N}_4$  (AY6)-30 v/o ARCO SiC Whiskers (100 hr, 1200°C, Static Air)

Thus, despite the differences during oxidation found in the make-up of the oxidation products, it may be concluded that the presence of SiC whiskers and additional calcium impurities in the AY6-30 v/o SiCw composites does not compromise or appreciably change the oxidation behavior of this material as compared to the AY6 monolith.

The oxidation of SiC (SC-9) whiskers was examined separately. The whiskers were oxidized in  $\text{Al}_2\text{O}_3$  crucibles at 1200°C in static air ( $\approx 50\%$  relative humidity) and exhibited parabolic oxidation behavior (Figure 38). Phase analysis (XRD) of the oxidized whiskers showed an increase in the amount of amorphous phase with increasing oxidation time at a lattice spacing corresponding to  $\text{SiO}_2$  (tridymite), which is consistent with the oxidation temperature employed. It was further noted that while the SiC whiskers in the as-received state exhibited predominantly  $\alpha$  phase (hexagonal) peaks, the relative intensity of  $\beta$  phase (cubic) peaks increased with increasing oxidation time. This may result from preferential oxidation of the  $\alpha$  phase.

Oxidation rate constants for whiskers, baseline silicon nitride, and the composite, as well as the expectation value calculated for 30 v/o SiC whisker composites, are given in Table 14. Calculated and measured values for 30 v/o SiC (whisker)-containing composites are in good agreement.

The effect of oxidation at 1200°C up to 500 hours on modulus of rupture has also been evaluated (Table 15). While at room temperature, small variations in strength were observed; the MOR at elevated temperature is unaffected by oxidation. Based on these data, i.e., weight gain and MOR, the effects of oxidation on AY6 and AY6 + 30 v/o SiC whisker-containing composites are statistically equivalent.

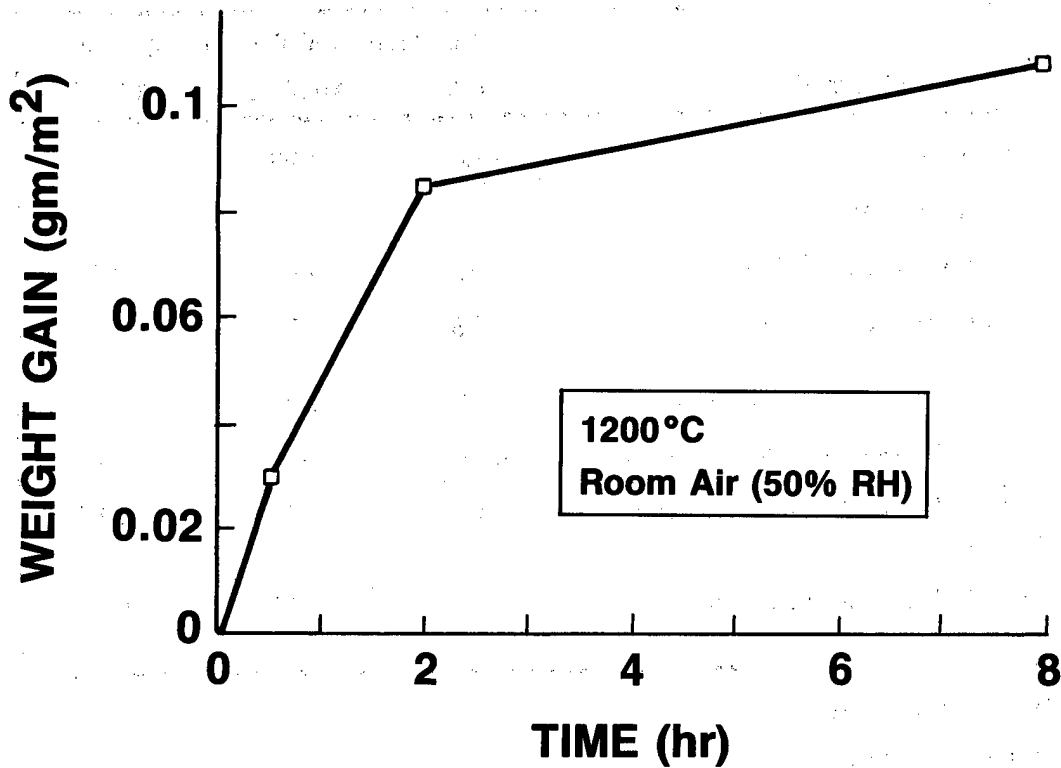


Figure 38. Static Air Oxidation of ARCO (SC-9) SiC Whiskers

Table 14. Oxidation rate constants ( $K_p$ ) of investigated materials

Material	$K_p$ (Kg/m <sup>2</sup> ·sec <sup>1/2</sup> ) <sup>2</sup>
SiCw (SC-9)	$3.47 \times 10^{-13}$
AY6	$5.89 \times 10^{-12}$
AY6 + 30 v/o SiCw (SC-9)	$4.51 \times 10^{-12}$
<b>Rule of Mixtures</b>	
$0.7 K_p^{AY6} + 0.3 K_p^{SiCw}$	$4.23 \times 10^{-12}$

Table 15. Strength of oxidized silicon nitride-based ceramics

Material	Relative Modulus of Rupture		
	25 °C	1000 °C	1200 °C
AY6-As Ground	1.00	0.98	0.81
AY6-Ground/Annealed*	0.98	—	—
AY6-Ground/Oxidized** (100 hr)	0.93	0.97	0.81
AY6-Ground/Oxidized** (500 hr)	0.98	1.01	0.74
AY6 + 30 v/o SiCw***-As Ground	1.00	1.03	0.93
AY6 + 30 v/o SiCw-Ground/Annealed*	0.95	—	—
AY6 + 30 v/o SiCw-Ground/Oxidized** (100 hr)	1.06	1.08	0.87
AY6 + 30 v/o SiCw-Ground/Oxidized** (500 hr)	0.98	1.06	0.88

\* 1200 °C/60 min/Ar

\*\* 1200 °C/Ambient Air

\*\*\* ARCO SC-9

**Thermal Conductivity.** Tables 16 and 17 give the experimental enthalpy-temperature and the calculated specific heat data for AY6 and the AY6 + 30 v/o SiC whisker composites. Tables 18 and 19 give the thermal diffusivity/conductivity data, and Figure 39 shows the thermal conductivity temperature relationship for the two materials measured. At room temperature, the addition of 30 v/o SiC produced a 30 % increase in thermal conductivity compared to monolithic  $\text{Si}_3\text{N}_4$ . This difference is reduced to 15 % at 1200 °C.

**Thermal Expansion.** Thermal expansion of the baseline composite and the composite containing 30 v/o SiC whiskers was measured by means of a dilatometer (Theta) for the range of temperature from 25 °C to 1400 °C. Thermal expansion coefficients of the composites perpendicular to the hot-pressing direction of both materials are given in Table 20 and Figure 40. Linear thermal expansion of the composite is similar to that of baseline AY6 material.

Table 16: Enthalpy and specific heat values for  $\text{Si}_3\text{N}_4$  (AY6)

Enthalpy		Specific Heat	
Temperature ( $^{\circ}\text{C}$ )	Cal ( $\text{gm}^{-1}$ )	Temperature ( $^{\circ}\text{C}$ )	$\text{Cp}$ Cal ( $\text{gm}^{-1} \text{C}^{-1}$ )
0	0	0	0.136
26.9	3.04	50	0.163
98.8	16.07	100	0.186
252.4	47.91	150	0.204
398.2	82.47	200	0.220
545.6	120.29	300	0.237
703.7	163.26	400	0.248
900.0	211.36	600	0.261
1208.0	297.19	800	0.269
		1000	0.273
		1200	0.275

Table 17: Enthalpy and specific heat values for  $\text{Si}_3\text{N}_4$  (AY6) — 30 v/o SiC whisker composite

Enthalpy		Specific Heat	
Temperature ( $^{\circ}\text{C}$ )	Cal ( $\text{gm}^{-1}$ )	Temperature ( $^{\circ}\text{C}$ )	$\text{Cp}$ Cal ( $\text{gm}^{-1} \text{C}^{-1}$ )
0	0	0	0.136
26.9	3.18	50	0.163
98.8	15.86	100	0.186
254.4	48.81	150	0.204
404.1	84.68	200	0.220
546.6	121.96	300	0.237
700.4	163.82	400	0.248
908.0	215.56	600	0.261
1194.0	300.01	800	0.269
		1000	0.273
		1200	0.275

Table 18: Thermal diffusivity/conductivity\* of  $\text{Si}_3\text{N}_4$  (AY6)

Temperature ( $^{\circ}\text{C}$ )	F	Diffusivity $\text{cm}^2 \text{ s}^{-1}$	Specific Heat $\text{cal g}^{-1} \text{ C}^{-1}$	Conductivity $\text{w cm}^{-1} \text{ C}^{-1}$	Btu in $\text{hr}^{-1} \text{ ft}^{-2} \text{ F}^{-1}$
28	82	0.0958	0.150	0.1940	134.5
99	211	0.0811	0.185	0.2026	140.5
264	508	0.0625	0.232	0.1959	135.8
429	805	0.0492	0.250	0.1661	115.2
653	1207	0.0422	0.264	0.1504	104.3
819	1506	0.0366	0.270	0.1332	92.4
985	1805	0.0343	0.273	0.1264	87.6
1106	2022	0.0310	0.274	0.1147	79.5
1200	2092	0.0288	0.275	0.1070	74.2

Table 19: Thermal diffusivity/conductivity\* of  $\text{Si}_3\text{N}_4$  (AY6) — 30 v/o  
SiC whisker composite

Temperature ( $^{\circ}\text{C}$ )	F	Diffusivity $\text{cm}^2 \text{ s}^{-1}$	Specific Heat $\text{cal g}^{-1} \text{ C}^{-1}$	Conductivity $\text{w cm}^{-1} \text{ C}^{-1}$	Btu in $\text{hr}^{-1} \text{ ft}^{-2} \text{ F}^{-1}$
28	82	0.1246	0.150	0.2523	174.9
98	208	0.1043	0.185	0.2605	180.6
264	508	0.0754	0.232	0.2361	163.7
431	807	0.0636	0.250	0.2147	148.9
656	1213	0.0492	0.264	0.1754	121.6
821	1509	0.0464	0.270	0.1691	117.2
986	1806	0.0369	0.273	0.1360	94.3
1110	2030	0.0351	0.274	0.1298	90.0
1200	2192	0.0335	0.275	0.1243	86.2

\*Measurements made parallel to the hot pressing direction



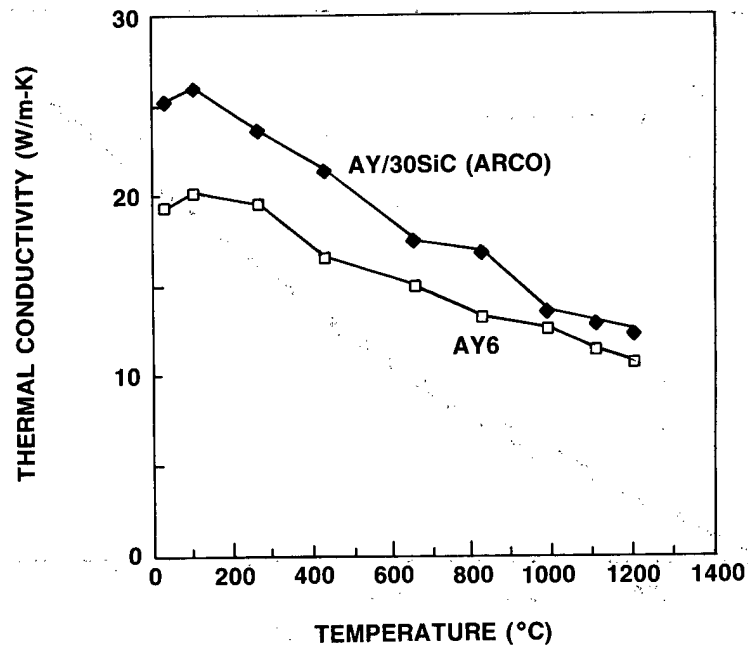


Figure 39. Thermal Conductivity of  $\text{Si}_3\text{N}_4$  (AY6) and a  $\text{Si}_3\text{N}_4$  (AY6) + 30 v/o SiC Whisker Composite up to 1200°C

Table 20: Thermal expansion coefficients of  $\text{Si}_3\text{N}_4$  (AY6) and  $\text{Si}_3\text{N}_4$  (AY6) containing 30% SiC whiskers

Temperature (°C)	AY6 + 30% Arco ( $10^{-6}/^{\circ}\text{C}$ )	AY6 ( $10^{-6}/^{\circ}\text{C}$ )
200	2.91	2.53
400	3.21	3.11
600	3.51	3.64
800	3.83	4.08
1000	4.16	4.42
1200	4.51	4.67
1400	4.86	4.87

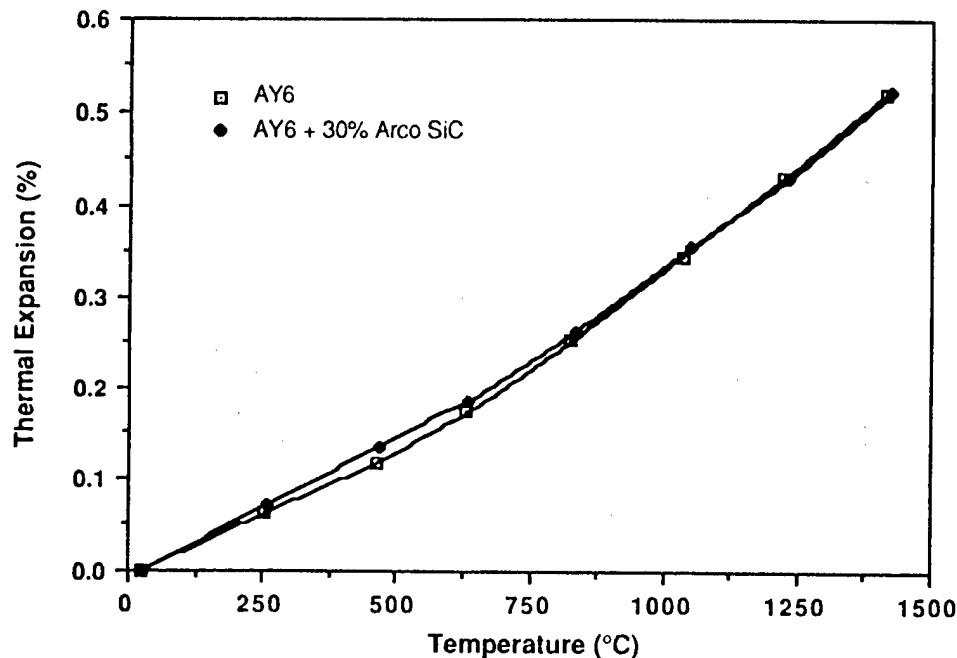


Figure 40. Thermal Expansion of Baseline  $\text{Si}_3\text{N}_4$  (AY6) and  $\text{Si}_3\text{N}_4$  (AY6) Containing 30 v/o SiC Whiskers As a Function of Temperature

## II. DEVELOPMENT OF PROCESS FOR COMPLEX PART FABRICATION

The process selected to develop and demonstrate a near-net-shape fabrication technology capable of producing ceramic matrix composite automotive engine components was injection molding. The system selected was the AY6 - 30 v/o SiC whisker material because of the improved properties previously described.

Figure 41 shows the approach used in the study. Due to unavailability of ARCO (SC-9) whiskers, it was necessary to utilize readily available Tateho whiskers for initial compounding and injection molding trials. Once procedures were developed using Tateho whiskers, ARCO whiskers were substituted for the final molding trials. The results of the feasibility experiments will be discussed in terms of the five major processing steps: powder preparation, compounding, injection molding, binder burnout, and densification.

### POWDER PREPARATION

Batches of AY6 + 30% SiC whiskers for injection molding were prepared by two process routes, preblend and compound blend. In the preblend case, dispersed whiskers were first added to AY6, and this material was then mixed with the binders. The alternate approach was to mix whiskers, AY6 and the binder using the high shear mixing action of the compounder to blend the components. Microstructural examination of as-molded and HIPed parts (compoinder blended powder) showed a large

number of AY6 agglomerates which were not broken down during compounding. Samples fabricated using preblended powders are homogeneous. Based on the above observations, preblending was selected as the powder preparation route of choice.

## COMPOUNDING

The compounding unit used throughout the feasibility study is a Haake torque rheometer mixer. The unit measures the torque required to maintain a fixed mixing rpm as well as an integrated total torque for each batch. Torques observed for whisker-containing material were significantly higher than for monolithic AY6 powder. After

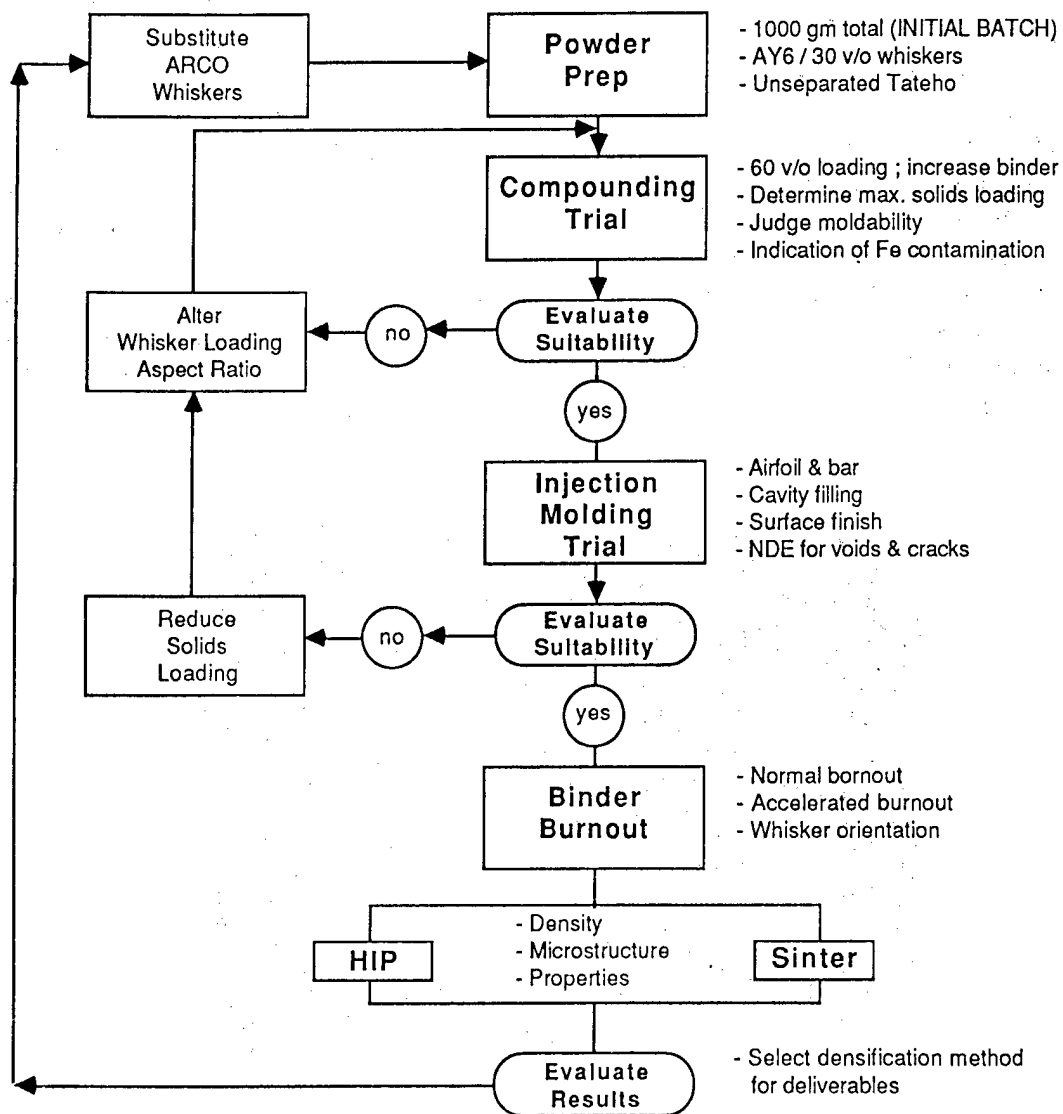


Figure 41. Outline of Process Development Approach

all powder was added, torques decreased exponentially with time to approach a steady state value. This final value was over twice that observed for noncomposite AY6 powders. This procedure was used in initial experiments designed to identify the maximum solids loading level in the binder which would give a moldable mix. Mixes were compounded containing from 52 to 58 v/o solids. The best results were obtained at 53 v/o solids. Compounding times from one to three hours were used. The three-hour compounding was observed to minimize residual AY6 agglomerates.

## INJECTION MOLDING

The injection molding machine used in all molding experiments is a Model 15S Boy screw-type injection molder with hydraulic clamping. It has a two-zone barrel heater and independent nozzle temperature control. Temperature control of the barrel and nozzle, along with mold temperature and injection pressure, was evaluated to maximize part yield and surface quality.

The mold employed for the majority of molding experiments was used previously in the DOE-sponsored CATE (Ceramic Applications in Turbine Engines) program. By altering the gate position, the mold can be configured to shoot either a single axial turbine blade, two test bars, or simultaneous filling of all three cavities. Figure 42 shows the fill pattern of the blade and one of the bar cavities.

Using this mold, blades and bars of AY6-containing 30 v/o SiC whiskers have been fabricated as injection-molded composite parts. SEM examination of fracture surfaces indicates that the whisker integrity is maintained through the molding process (Figure 43).

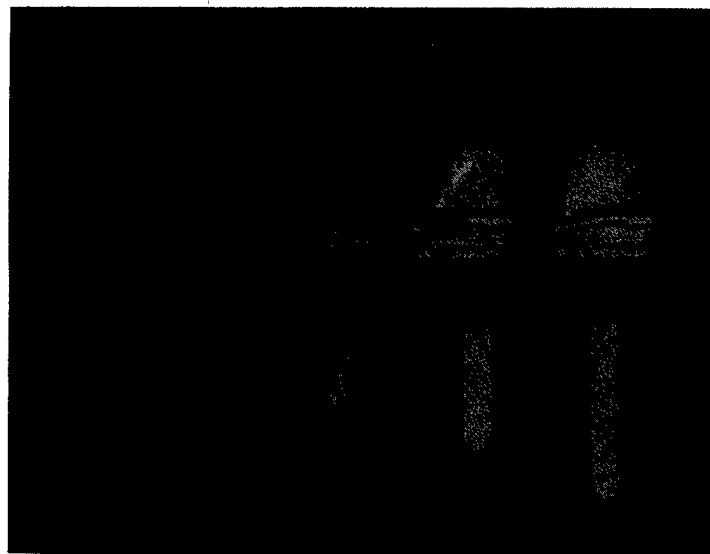


Figure 42. Series of Short Shots Showing Fill Pattern of  $\text{Si}_3\text{N}_4$ /Binder Mix in CATE Turbine Blade and Test Bar Die

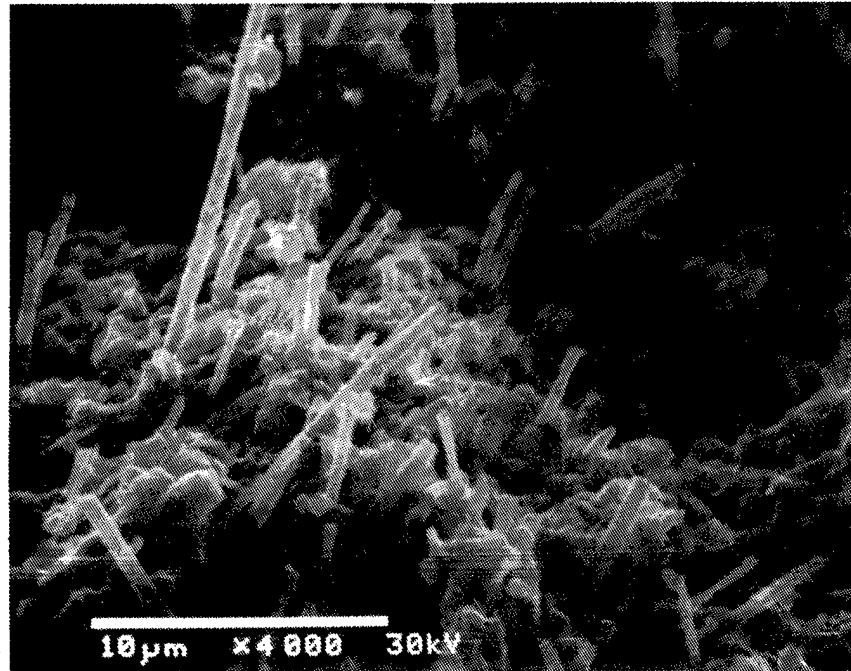


Figure 43. Fracture Surface of Injection-Molded  $\text{Si}_3\text{N}_4$ -30 v/o SiC Whisker Composite

#### **BINDER REMOVAL**

The binder was removed from the injection-molded composites by placing the part within a supporting setter powder and heating it slowly in an inert atmosphere. An air heating step is used after the binder is removed to eliminate residual free carbon. The parts showed no dimensional changes after binder burnout.

#### **HOT ISOSTATIC PRESSING**

Parts were glass encapsulated prior to hot isostatic pressing (HIP) at  $1750^\circ\text{C}$  and 30,000 psi for 1 hour. These conditions reproducibly yield composites of greater than 99% of theoretical density. Figure 44 shows a sequence of as-molded, burned out and HIPed CATE blades of AY6 + 30% SiC whisker composite material.

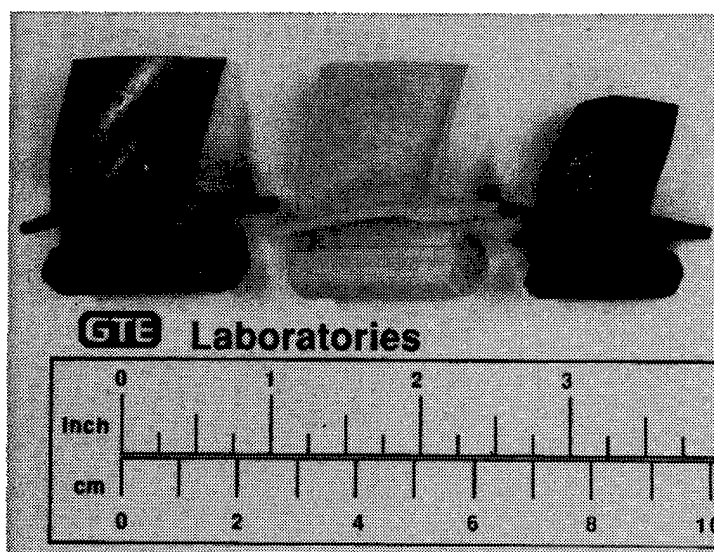


Figure 44. Injection-Molded CATE Blades Prepared from  $\text{Si}_3\text{N}_4$  - 30 v/o SiC (Whisker) Composite in As-Molded, Dewaxed, and Fired State

The main observation made from the densified samples was that a systematic and reproducible warpage occurred in the composite materials during densification. The blades showed areas of distortion in the airfoil trailing edge, platform, and dovetail. Test bars also showed distortion in the form of curvature along the length of the bar, with the gate on the concave side (Figure 45).

#### STUDY OF DISTORTION MECHANISM

Shrinkage measurements on AY6 + 30% SiC whisker samples have shown that shrinkage along the test bar length was smaller relative to test bar width and thickness. This shrinkage anisotropy suggested a preferred alignment of the whiskers.

An injection molding trial was then made using SiC whiskers which had been milled to a near equiaxed state prior to blending with AY6. This material, after HIP-ing by the same schedule, reached the same density but had uniform linear shrinkage in all directions (Table 21), which indicates that the whisker alignment played a major role in nonuniform densification shrinkage.

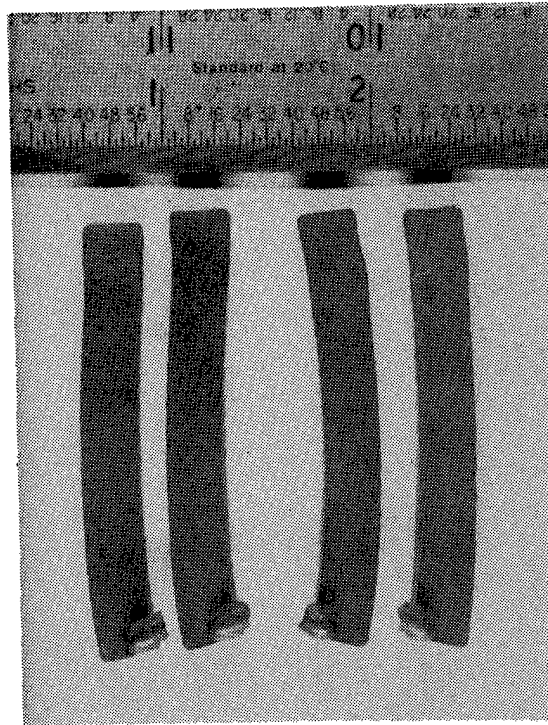


Figure 45. Distortion of Injection-Molded, HIPed Test Bars Containing  $\text{Si}_3\text{N}_4$ -30 v/o SiC Whiskers

Table 21: Normalized densification shrinkage of injection-molded composites containing 30 v/o SiC additions

Dimensions	Unmilled Whiskers	Milled Whiskers
Length	0.843	1.005
Width	1.074	1.000
Thickness	1.204	0.995

To understand the exact mechanism leading to test bar bending, a detailed quantitative microstructural evaluation of whisker orientation as a function of position in the test bar was performed. Sections of the HIPed composites containing 30 v/o ARCO SiC whiskers were cut from test bars. These sections were then mounted and polished. Multiple regions of the samples (Figure 46) were observed and photographed using both optical and SEM microscopy. Each whisker in a micrograph was defined by four points, the first two for whisker length, and the second two for the diameter. Each whisker image was digitized (Figure 47), and a computer program was used to determine aspect ratio and orientation angle for each of the approximately 200 whiskers

observed per picture along with their averages and standard deviations. For the bars, the angles of orientation for all whiskers with a  $l/d$  ratio greater than 2 were analyzed at different positions across the bar width. To provide a baseline against which samples could be compared, a computer simulation was made to predict the distribution of aspect ratios and orientations expected for randomly oriented and intersected whiskers.

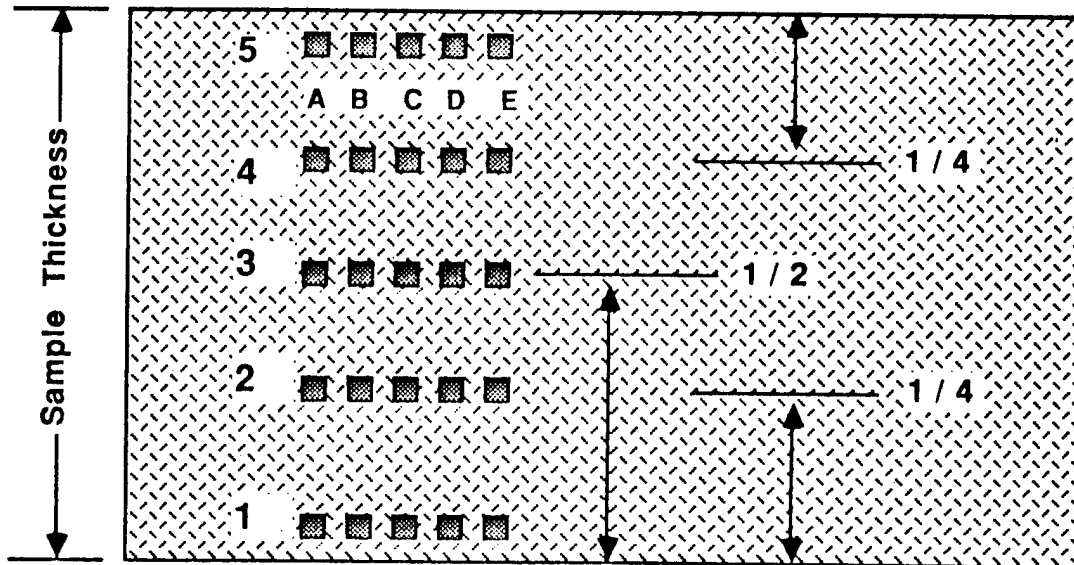


Figure 46. Regions Examined on Bar Cross Section for Whisker Orientation Determinations

Figure 48 illustrates in schematic form the whisker alignment determined along the bar length. The orientation observed is parabolic, but the side gate location causes the parabolic flow and the whisker orientation to be off-center with respect to the test bar central axis. The side opposite the gate has whisker orientation of a nature largely parallel to the bar length, while the gate side, containing the parabola vertex, has a greater number of whiskers orientated perpendicular to the bar length. Whiskers, when aligned in a matrix, would restrict densification shrinkage parallel to their alignment. It is the nonsymmetrical nature of the orientation, also observed across the bar, which is responsible for the distortion after HIPing.

Efforts to decrease the nonsymmetric whisker flow will require changes in the gate design for the injection molding die and would be proposed for future studies.

Compounding, molding, binder removal, and densification parameters capable of producing dense composites containing 30 v/o SiC whiskers in AY6 have been identified. These steps are represented along with powder preparation in a process flow sheet in Figure 49. Further development of forming techniques with particular attention to mold design to eliminate warpage and optimization of densification schedule are two of the prominently important areas to be considered in future research.



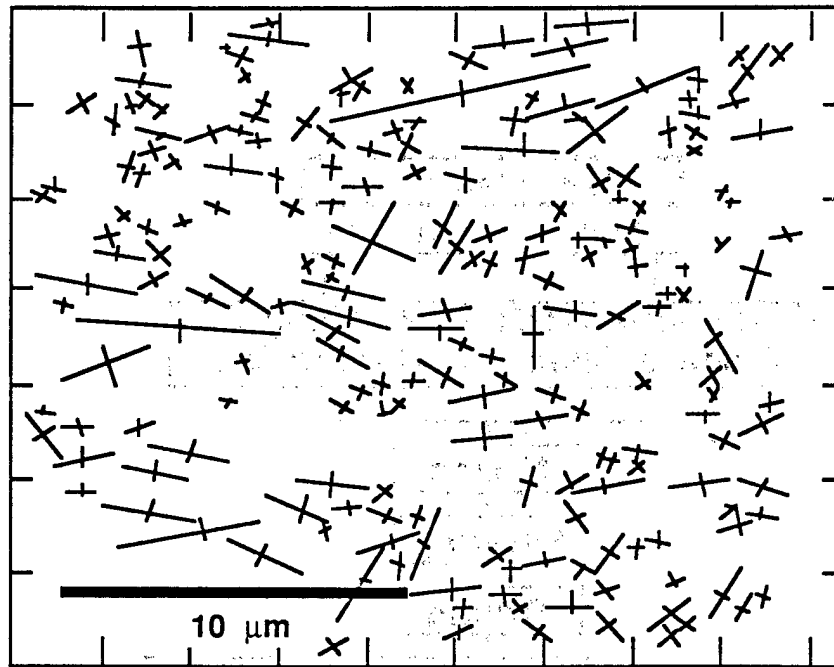


Figure 47. Digitized SiC Whiskers in Injection-Molded and HIPed Material Showing Orientation and Length/Diameter of Each Measured Whisker

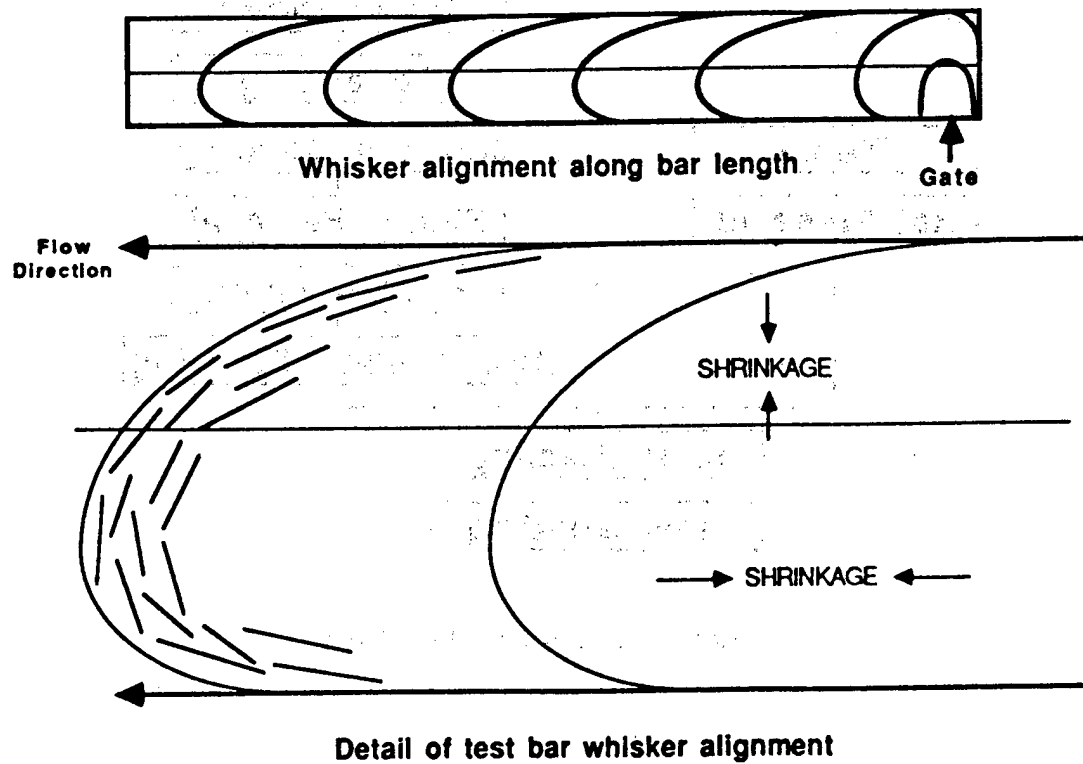


Figure 48. Whisker Orientation Model for Test Bar

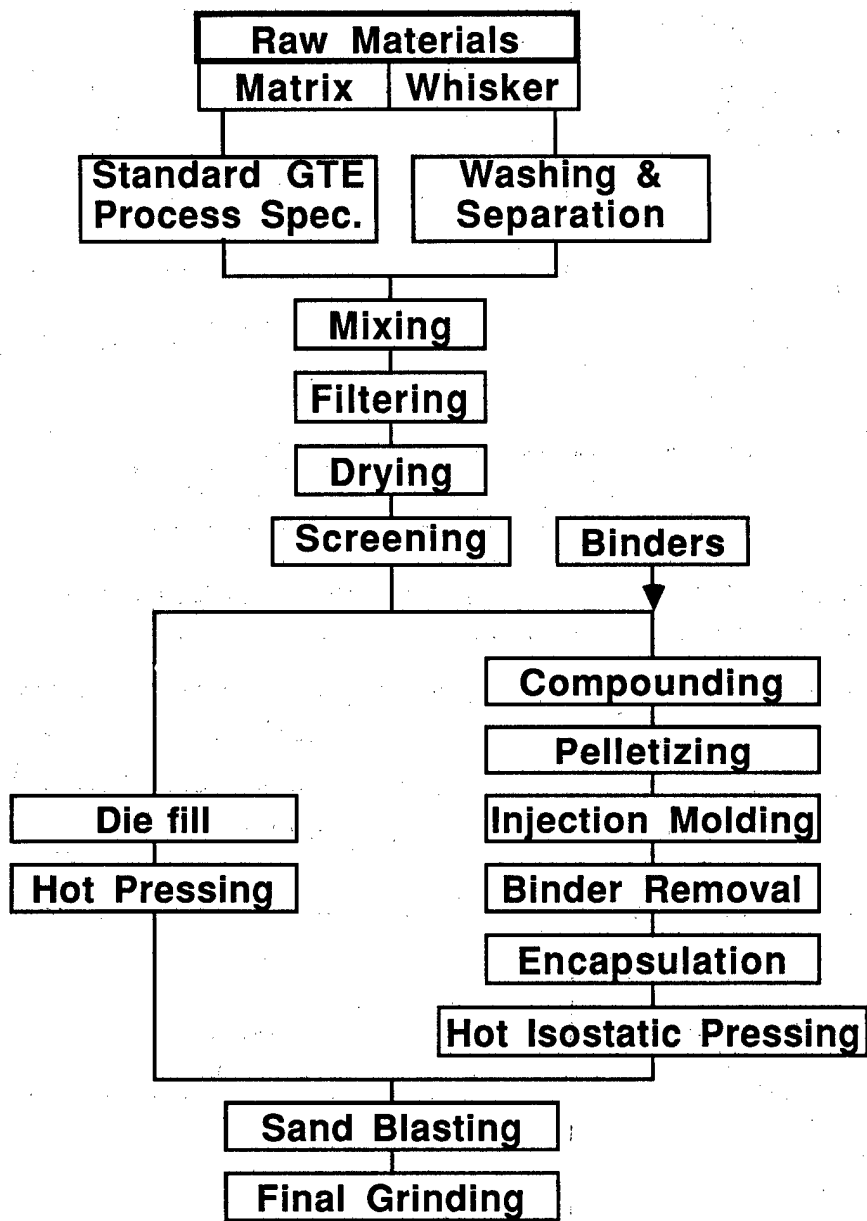


Figure 49. Process Flow Sheet

## CONCLUSIONS

Improvements in strength and fracture toughness of  $\text{Si}_3\text{N}_4$  have been achieved through the composite approach.

The room-temperature fracture toughness was increased by 40%, with a concomitant 25% strength increase by the addition of 30 v/o of SiC whiskers. At 35 v/o of whisker additions, an increase in fracture toughness of 70% was observed. Due to intergranular fracture, the degree of fracture toughness increase was found to depend on the matrix grain size, dispersoid content, and its size relative to the matrix. An increase in fracture toughness can be expected with dispersoids of a size larger than the effective grain size of the matrix ( $D/D^0 > 1$ ).

The acicular nature of  $\text{Si}_3\text{N}_4$  grains reduces the effectiveness of particulate dispersoids as toughening agents. Whisker additions offer considerably higher potential in fracture toughness and strength enhancement.

The matrix microstructural development during densification can be affected by the presence of dispersoids, as well as by sintering conditions. In order to interpret the effect of dispersoid additions, it is of paramount importance that the microstructures of composites, including the matrix grain size and size distribution, be fully characterized.

Considering the results obtained for the  $\text{Si}_3\text{N}_4$ -SiCw system, it appears reasonable to expect further improvements in fracture toughness through an increase of amount and aspect ratio of dispersed phase. This approach, in either case, is expected to increase difficulties in processing. As was demonstrated by this work, matrix microstructure plays an important role in determining the composite properties, suggesting that further development of these composites through dispersoid additions must be concurrent with additional matrix microstructure tailoring.

The current program has demonstrated that  $\text{Si}_3\text{N}_4$ -based composites containing up to 30 v/o of SiC whiskers could be injection molded and densified by HIP to over 99% of theoretical density. This work has also pointed at several areas where further process development is needed to bring injection-molded composites from the feasibility demonstration stage to a technology ready for prototype fabrication. In view of the preceding discussion, it is also apparent that additional process adaptations will be required to accommodate and fabricate new developmental materials. This effort would address optimization of binder system, compounding and molding techniques, and densification procedure.

## REFERENCES

1. F.F. Lange, "Effect of Microstructure on Strength of  $\text{Si}_3\text{N}_4$ -SiC Composite System," *J. Am. Ceram. Soc.* **56** (9), 445-450 (1973).
2. C. Greskovich and J.A. Palm, "Observations on the Fracture Toughness of  $\beta$ - $\text{Si}_3\text{N}_4$ - $\beta$ -SiC Composites," *J. Am. Ceram. Soc.* **63** (9-10), 597-599 (1980).
3. T. Mah, et al., "Fracture Toughness of  $\beta$ - $\text{Si}_3\text{N}_4$ -TiC Composites," *J. Am. Ceram. Soc.* **63** (9-10), 597-599 (1980).

4. S.T. Buljan and V.K. Sarin, "Machining Performance of Ceramic Tools," *Cutting Tool Materials, Proc. Conf. on Cutting Tool Mat., ASM*, 335-346 (1981).
5. S.T. Buljan and V.K. Sarin, "Silicon Nitride-Based Composites," *Sint. Metal-Ceramic Composites*, Ed. G.S. Upadaya, Elsevier Sci. Pub. B.V., Amsterdam, 455-468 (1984).
6. A.G. Evans, "The Strength of Brittle Materials Containing Second Phase Dispersoids," *Phys. Mag.* **26**, 1327-1344 (1972).
7. F.F. Lange, "The Interaction of a Crack Front with a Second Phase Dispersion," *Phil. Mag.* **22**, 983-992 (1980).
8. W.S. Williams and R.D. Schaal, "Elastic Deformation, Plastic Flow and Dislocations in Single Crystals of Titanium Carbide," *J. Appl. Phys.* **33** (3): 955-962 (1962).
9. J.C. Swearingen, et al., "Fracture Toughness of Reinforced Glasses," 973-987, *Fracture Mechanics of Ceramics, Vol. 4* (R.C. Bradt, et al., ed.) Plenum Press, New York (1978).
10. K.T. Faber, "Toughening of Ceramic Materials by Crack Deflection Process," Ph.D. Thesis, Univ. of CA, Berkeley (1982).
11. T.D. Eshelby, "The Determination of the Elastic Field of an Ellipsoidal Inclusion and Related Problems," *Proc. Roy. Soc.* **241**, 376-396 (1957).
12. K.T. Faber and A.G. Evans, "Crack Deflection Process-I Theory," *Acta. Metall.* **31** (4), 565 (1983).
13. G.C. Wei and P.F. Becher, "Development of SiC-Whisker-Reinforced Ceramics," *Am. Ceram. Soc. Bull.* **64** (2), 298-304 (1985).
14. P.D. Shalek, et al., "Hot Pressed SiC Whisker/Si<sub>3</sub>N<sub>4</sub> Matrix Composites," *Am. Ceram. Soc. Bull.* **65** (2), 351-356 (1986). J. Selsing, "Internal Stresses in Ceramics," *J. Am. Ceram. Soc.*, **44** (8): 419-424 (1961).
15. R.W. Davidge and T.J. Green, "The Strength of Two-Phase Ceramic/Glass Materials," *J. Mater. Sci.* **3**, 629-634 (1968).
16. V.V. Kristie and P.S. Nicholson, "Toughening of Glasses by Metallic Particles," *J. Am. Ceram. Soc.* **64** (9), 499-504 (1981).
17. J.J. Petrovic, et al., "Controlled Surface Flaws in Hot Pressed Si<sub>3</sub>N<sub>4</sub>," *J. Am. Ceram. Soc.* **58** (3-4): 113-116 (1975).
18. J.G. Baldoni, et al., "Particulate Titanium Carbide-Ceramic Matrix Composites," 472-458, *Inst. Phys. Conf. Ser. No. 75*: Clap Adam Hilger Ltd., Bristol, England (1986).
19. A.G. Evans and E.A. Charles, "Fracture Toughness Determinations by Indentation," *J. Am. Ceram. Soc.* **58** (7-8), 371-372 (1976).
20. S.T. Buljan, et al., "Si<sub>3</sub>N<sub>4</sub>-SiC Composites," *Bull. Am. Ceramic Soc.* **66** (2), 347-352 (1987).
21. G. Zilberstein and S.T. Buljan, "Characterization of Matrix-Dispersoid Reactions in Si<sub>3</sub>N<sub>4</sub>-TiC Composites," **Advances in Materials Characterization II**, Ed. R.L. Snyder, R.A. Condrate, Sr., and P.F. Johnson, Plenum Pub. Corp., 389-401 (1985).
22. R.D. Nixon, et al., "Deformation Behavior of SiC Whisker-Reinforced Si<sub>3</sub>N<sub>4</sub>," *Mater. Res. Soc. Symp. Proc.*, **Vol. 78**, 295-302 (1987).

### PUBLICATIONS

1. S.T. Buljan, J.G. Baldoni, M.L. Huckabee, "Si<sub>3</sub>N<sub>4</sub>-SiC Composites," *Am. Ceram. Soc. Bull.* **66** (2), 347-352 (1987).
2. S.T. Buljan and G. Zilberstein, "Microstructure Development in Si<sub>3</sub>N<sub>4</sub>-Based Composites," *Mater. Res. Soc. Symp. Proc.* **Vol. 78**, 273-281 (1987).
3. S.T. Buljan, J.G. Baldoni, M.L. Huckabee and G. Zilberstein, "Dispersion Toughened Si<sub>3</sub>N<sub>4</sub>," Proc. 24th Automotive Tech. Coord. Meeting, **P-197**, 319-325 (1986).
4. R.D. Nixon, et al., "Deformation Behavior of SiC Whisker-Reinforced Si<sub>3</sub>N<sub>4</sub>," *Mater. Res. Soc. Symp. Proc.*, **Vol. 78**, 295-302 (1987).

### PRESENTATIONS

1. J.G. Baldoni and S.T. Buljan, "Character of Crack Propagation in Ceramic Matrix Composites," Ann. Conf. on Composites and Adv. Ceram., Cocoa Beach, FL (January 1986).
2. S.T. Buljan, J.G. Baldoni, and M.L. Huckabee, "Silicon Nitride-Silicon Carbide Composites," 88th Ann. Meeting Am. Ceram. Soc., Chicago, IL (April 1986).
3. S.T. Buljan, J.G. Baldoni, M.L. Huckabee and G. Zilberstein, "Dispersion-Toughened Silicon Nitride," 24th Ann. CCM, Dearborn, MI (October 1986).
4. G. Zilberstein and S.T. Buljan, "Microstructure Development in Si<sub>3</sub>N<sub>4</sub>-Based Composites, Mat. Res. Soc., Boston MA (December 1986).
5. M.L. Huckabee, J.G. Baldoni, G. Zilberstein, and S.T. Buljan, "Effect of Matrix and Dispersoid Interactions on the Mechanical Properties of Silicon Nitride-Silicon Carbide Whisker Composites," 89th Ann. Meeting Am. Ceram. Soc., Pittsburgh, PA (April 1987).
6. S.T. Buljan, J.G. Baldoni, M.L. Huckabee, J.T. Neil, and G. Zilberstein, "SiC Whisker-Reinforced Si<sub>3</sub>N<sub>4</sub>," 25th Ann. CCM, Detroit, MI (October 1987).

**APPENDIX 1: ENGINEERING PROPERTY DATA FOR  $\text{Si}_3\text{N}_4$  AND  
30 v/o SiC WHISKER COMPOSITES**

<b>K<sub>IC</sub> (MPa·m<sup>1/2</sup>)</b>	<b>AY6</b>	<b>AY6 + 30 v/o SiCw</b>		
25 °C	4.6 ± 0.2	6.4 ± 0.5		
1000 °C	4.9 ± 0.3	7.7 ± 0.4		
1200 °C	6.1 ± 0.1	8.5 ± 0.5		
<b>MOR (MPa)</b>				
25 °C	773 ± 67	975 ± 39		
1000 °C	585 ± 14	819 ± 64		
1200 °C	486 ± 43	597 ± 26		
1400 °C	197 ± 4	257 ± 25		
<b>Elastic Properties</b>				
Young's Modulus (GPa)	297	335		
Poisson's Ratio	0.27	0.26		
Shear Modulus (GPa)	116	113		
Bulk Modulus (GPa)	218	234		
<b>Oxidation (1200 °C/Air)</b>				
Rate Constant (kg/m <sup>2</sup> ·sec <sup>-1/2</sup> ) <sup>2</sup>	5.9 × 10 <sup>-12</sup>	4.5 × 10 <sup>-12</sup>		
<b>MOR Normalized to Nonoxidized Room-Temperature Value</b>	<b>100 h</b>	<b>500 h</b>	<b>100 h</b>	<b>500 h</b>
25 °C	0.93	0.98	1.06	0.98
1000 °C	0.97	1.01	1.08	1.06
1200 °C	0.81	0.74	0.87	0.88
<b>Knoop Microhardness (GPa)</b>				
	13.8 ± 0.1		15.9 ± 0.1	
<b>Thermal Conductivity (W/cmC)</b>				
25 °C	0.194		0.252	
1000 °C	0.126		0.136	
1200 °C	0.107		0.124	
<b>Thermal Expansion Coefficient (× 10<sup>-6</sup> °C<sup>-1</sup>)</b>				
200 °C	2.53		2.91	
400 °C	3.11		3.21	
600 °C	3.64		3.51	
800 °C	4.08		3.83	
1000 °C	4.42		4.16	
1200 °C	4.67		4.51	
1400 °C	4.87		4.86	

## APPENDIX 2: INDENTATION FRACTURE TOUGHNESS

Based on a dimensional analysis, Evans and Charles<sup>19</sup> derived the following relationship:

$$K_C \phi / H \sqrt{a} = 0.15 k \left( \frac{c}{a} \right)^{-3/2} \dots \dots (1)$$

where  $K_C$  = fracture toughness

$H$  = microhardness

$\phi$  = constraint factor  $\cong 3$

$k$  = correlation factor required by the presence of the free surface = 3.2

$c$  = length of a single crack measured from the center of the Vickers indentation (Figure A2-1)

$a$  =  $1/2$  the size of the Vickers indentation diagonal (Figure A2-1)

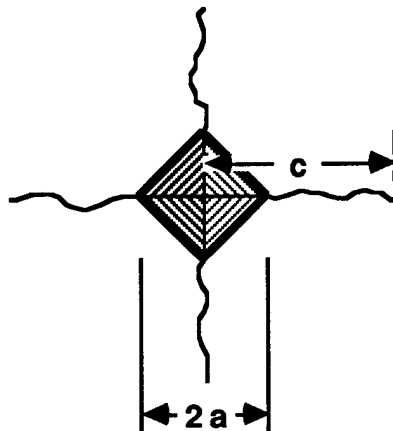


Figure A2-1. Appearance of Vickers Indentation and Parameters Used for  $K_C$

The equation used to calculate fracture toughness by indentation (IFT) in use at GTE Laboratories is derived from the Evans and Charles relationship in the following manner with a redefinition of indentation parameters.

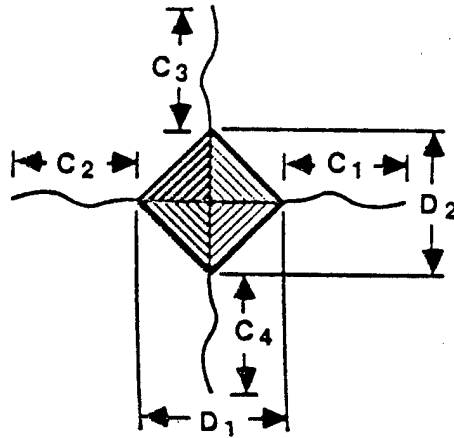


Figure A2-2. Appearance of Vickers Indentation and Parameters Used for IFT Determination at GTE Laboratories

$$C_L = \text{total crack length} = \sum_{n=1}^{n=4} C_n$$

where  $c_n$  are measured from the points of the Vickers indentation, *not* from the center of the Vickers indentation.

$$D = \frac{D_1 + D_2}{2} = \text{average indentation size, therefore by definition}$$

$$D = 2a \text{ or } a = 0.5D$$

comparing Figures A2-1 and A2-2

$$C(\text{Evans and Charles}) = a + \bar{c}$$

$$\text{where } \bar{c} = \text{average crack length} = \frac{C_L}{4}$$

$$\therefore c = a + \frac{C_L}{4}$$

$$\frac{C}{a} = 1 + \frac{C_L}{4a}$$

Rearranging equation (1) yields:

$$K_C = \frac{0.15k H \sqrt{a}}{\phi} \left( \frac{c}{a} \right)^{-3/2}$$



substituting the redefined term yields:

$$K_C = \frac{\frac{0.15k H \sqrt{a}}{\phi}}{\left(1 + \frac{C_L}{4a}\right)^{3/2}}$$

$$K_C = \frac{\frac{0.15k H \sqrt{0.5D}}{\phi}}{\left(1 + \frac{C_L}{4(0.5D)}\right)^{3/2}} \text{ since } a = 0.5D$$

$$\frac{0.15k \sqrt{0.5}}{\phi} = \frac{0.15 (3.2) (\sqrt{0.5})}{3} = 0.113$$

$$\therefore \text{IFT} = K_C = \frac{0.113 H \sqrt{D}}{\left(1 + \frac{C_L}{2D}\right)^{3/2}} \quad (2)$$

The microhardness term, H, in both equations 1 and 2 has not yet been specified as to type, i.e., Vickers or Knoop. Evans and Charles used the Vickers hardness calculated from the Vickers indentation used to produce surface cracks. However, hardness measurements made from cracked indentations can result in erroneous values. Therefore, the GTE Laboratories procedure has been standardized using Knoop microhardness with the Knoop indentations produced with a 1 kg load. The geometry of the Knoop indenter produces crack-free indentations which are also easier to measure and therefore less subject to measurement error than light load (<500 gm) crack-free Vickers indentations.

The relationship used to determine indentation fracture toughness (IFT) is then

$$K_C = \text{IFT} = \frac{0.113 H \sqrt{D}}{\left(1 + \frac{C_L}{2D}\right)^{3/2}} \quad (3)$$

where:

H = 1 kg Knoop microhardness (GN/m<sup>2</sup>)

D = average Vickers indentation diagonal size (μm),

C<sub>L</sub> = sum of four cracks emanating from the four corners of a Vickers indentation (μm)

The measured crack lengths and average diagonals produced by the 10 kg Vickers indentation are shown in Table A2-1 for Si<sub>3</sub>N<sub>4</sub> and Al<sub>2</sub>O<sub>3</sub>-based materials. Also included are the average Vickers and Knoop microhardness values for each material. For a given load, the diagonal of a Vickers indenter is about one third of the length of the Knoop

indenter due to the differences in indenter geometry. This affects the calculated values of microhardness with the Knoop values being approximately 15 % less than the Vickers values for the same material. Consequently, the value of fracture toughness calculated using the expression previously given, which contains a hardness term, is dependent upon microhardness technique; i.e., the IFT values calculated using Knoop microhardness are approximately 15 % lower than those calculated using Vickers microhardness.

Table A2-1. Indentation data and calculated indentation fracture toughness (IFT)

	$\text{Si}_3\text{N}_4$ (AY6)	$\text{Si}_3\text{N}_4$ (AY6) + 30 v/o TiC	$\text{Al}_2\text{O}_3^{**}$	$\text{Al}_2\text{O}_3$ + 30 v/o TiC
Vickers Diagonal, $\mu\text{m}$	109.5 $\pm$ 0.6	104.4 $\pm$ 0.6	102.1 $\pm$ 0.5	95.4 $\pm$ 0.7
Total Crack Length, $\mu\text{m}$	298.1 $\pm$ 9.0	341.4 $\pm$ 18.2	528.6 $\pm$ 37.4	475.9 $\pm$ 19.6
Microhardness, GPa				
Vickers, HV10	15.2 $\pm$ 0.3	16.7 $\pm$ 0.3	17.4 $\pm$ 0.2	20.0 $\pm$ 0.4
Knoop, HK1	13.6 $\pm$ 0.8	14.6 $\pm$ 0.5	15.2 $\pm$ 0.8	16.8 $\pm$ 0.7
IFT, $\text{MPa} \cdot \text{m}^{1/2}$				
using HV10	5.0 $\pm$ 0.1	4.5 $\pm$ 0.1	2.9 $\pm$ 0.1	3.5 $\pm$ 0.1
using HK1	4.1 $\pm$ 0.1	4.0 $\pm$ 0.2	2.6 $\pm$ 0.2	3.0 $\pm$ 0.2

\*\*Fine-grained  $\text{Al}_2\text{O}_3$  cutting tool

An AY6-30 v/o TiC sample was indented with a Vickers indenter using a 10 kg load, and the appropriate indentation parameters were measured. Modulus of elasticity and Knoop microhardness were also measured. The IFT was then calculated using the same data for the various published techniques (Table A2-1). The value of IFT by the GTEL standard technique is dependent upon the microhardness technique employed. The calculated value using Vickers hardness is higher than the standard technique. Additionally, this higher value is comparable to other techniques which employ the plastic zone correction indicating that, for ceramic materials, this factor has little influence on the measured indentation fracture toughness. For comparison with published data, use of the Vickers hardness value in the calculation is recommended.

Table A2-2. Indentation fracture toughness of  $\text{Si}_3\text{N}_4$  (AY6) + 30 v/o TiC accessed by various techniques

1) <u>Standard IFT</u>	2) <u>IFT Using Vickers Hardness</u>	3) <u><math>K_{IC}</math> Anstis, et al.</u>	4) <u><math>K_{IC}</math> Evans</u>
4.5	5.0	5.0	5.2
1) $IFT = 0.113 HD^{1/2} / (1 + \frac{C_L}{2D})^{3/2}$ H = Knoop Hardness, D = Vickers Diagonal, $C_L$ = Total Crack Length			
2) Same formula as 1, but substituting Vickers Hardness for Knoop Hardness.			
3) $K_{IC} \text{ Anstis} = 0.016 (E/H_V)^{1/2} (P/C_O)^{3/2}$ E = Young's Modulus; $H_V$ = Vickers Hardness; P = Indentation Load; $C_O$ = Length of a Single Crack = $C_L/4 + D/2$			
4) $K_{IC}$ Evans $\log \left[ \frac{K_{IC}}{H\sqrt{D/2}} \left( \frac{H}{E} \right)^{2/5} \right] = -1.59 - 0.3A - 2.02A^2 + 11.23A^3 - 24.97A^4 - 16.32A^5$ $A = \log \left( \frac{C_O}{D/2} \right)$			

ORNL/Sub/85-22011/1  
Dist. Category UC-95

## INTERNAL DISTRIBUTION

- |                                    |                        |
|------------------------------------|------------------------|
| 1-2. Central Research Library      | 62. R. R. Judkins      |
| 3. Document Reference Section      | 63. M. A. Karnitz      |
| 4-5. Laboratory Records Department | 64. H. D. Kimrey, Jr.  |
| 6. Laboratory Records, ORNL RC     | 65. T. G. Kollie       |
| 7. ORNL Patent Section             | 66. T. B. Lindemer     |
| 8. L. F. Allard, Jr.               | 67. K. C. Liu          |
| 9. B. R. Appleton                  | 68. E. L. Long, Jr.    |
| 10. R. L. Beatty                   | 69. W. D. Manly        |
| 11. P. F. Becher                   | 70. D. L. McElroy      |
| 12. T. M. Besmann                  | 71. J. R. Merriman     |
| 13. P. J. Blau                     | 72. A. J. Moorhead     |
| 14. A. Bleier                      | 73. T. A. Nolan        |
| 15. E. E. Bloom                    | 74. J. L. Rich         |
| 16. K. W. Boling                   | 75. C. R. Richmond     |
| 17-40. R. A. Bradley               | 76. J. M. Robbins      |
| 41. C. R. Brinkman                 | 77. M. W. Rosenthal    |
| 42. V. R. Bullington               | 78. M. L. Santella     |
| 43. A. J. Caputo                   | 79. A. C. Schaffhauser |
| 44. R. S. Carlsmith                | 80. G. M. Slaughter    |
| 45. P. T. Carlson                  | 81. W. B. Snyder, Jr.  |
| 46. J. V. Cathcart                 | 82. E. J. Soderstrom   |
| 47. G. M. Caton                    | 83. D. P. Stinton      |
| 48. R. H. Cooper                   | 84. R. W. Swindeman    |
| 49. S. A. David                    | 85. V. J. Tennery      |
| 50. J. H. DeVan                    | 86-88. P. T. Thornton  |
| 51. W. P. Eatherly                 | 89. T. N. Tieg         |
| 52. J. I. Federer                  | 90. J. R. Weir, Jr.    |
| 53. W. Fulkerson                   | 91. F. W. Wiffen       |
| 54. R. L. Graves                   | 92. R. K. Williams     |
| 55. D. L. Greene                   | 93. S. G. Winslow      |
| 56. M. A. Janney                   | 94. C. S. Yust         |
| 57-61. D. R. Johnson               |                        |

## EXTERNAL DISTRIBUTION

- |   |   |
|---|---|
| 95. Donald F. Adams<br>University of Wyoming<br>Laramie, WY 82071                             | 98. Bruce J. Agle<br>Sundstrand Corporation<br>Turbomach Division<br>4400 Ruffin Road<br>PO Box 85757<br>San Diego, CA 92138-5757 |
| 96. Jane W. Adams<br>Corning Glass Works<br>Corning, NY 14831                                 |   |
| 97. Donald J. Adrian<br>High Velocity Corporation<br>701 Scarboro Road<br>Oak Ridge, TN 37830 | 99. Richard L. Allor<br>Ford Motor Company<br>20000 Rotunda Drive<br>PO Box 2053<br>Dearborn, MI 48121-2053                       |

100. Richard T. Alpaugh  
U.S. Department of Energy  
Forrestal Building CE-151  
1000 Independence Avenue  
Washington, DC 20585
101. H. Arbabi  
Brunel University  
Uxbridge Middlesex  
UNITED KINGDOM UB8 3PH
102. V. S. Avva  
North Carolina Agricultural and  
Technical State University  
Greensboro, NC 27411
103. John M. Bailey  
Caterpillar Inc.  
Technical Center  
Post Office Box 1875  
Peoria, IL 61656-1875
104. Murray Bailey  
NASA Lewis Research Center  
21000 Brookpark Road  
MS: 77-6  
Cleveland, OH 44135
105. R. R. Baker  
Ceradyne, Inc.  
3169 Red Hill Avenue  
Costa Mesa, CA 92626
- 106-110. J. Gary Baldoni  
GTE Laboratories, Inc.  
40 Sylvan Road  
Waltham, MA 02254
111. A. L. Bement, Jr.  
TRW, Inc.  
23555 Euclid Avenue  
Cleveland, OH 44117
112. M. Bentele  
Xamag, Inc.  
259 Melville Avenue  
Fairfield, CT 06430
113. Clifton G. Bergeron  
University of Illinois  
105 South Goodwin Avenue  
204 Ceramics Building  
Urbana, IL 61801
114. William D. Bjorndahl  
TRW, Inc.  
One Space Park  
Building 01, Room 2060  
Redondo Beach, CA 90278
115. James A. Black  
American Matrix, Inc.  
118 Sherlake Drive  
Knoxville, TN 37922
116. Dan Blake  
Solar Energy Research  
Institute  
1617 Cole Boulevard  
Golden, CO 80401
117. Keith Blandford  
Boride Products, Inc.  
2879 Aero Park Drive  
Traverse City, MI 49684
118. John Blum  
Norton Company  
High Performance Ceramics  
Goddard Road  
Northboro, MA 01532-1545
119. Paul N. Blumberg  
Integral Technologies Inc.  
415 East Plaza Drive  
Westmont, IL 60559
120. Wolfgang D. G. Boecker  
Standard Oil Engineered  
Materials Company  
Post Office Box 832  
Niagara Falls, NY 14302
121. Han Juergen Bossmeyer  
BMW Technologies, Inc.  
800 South Street  
Waltham, MA 02154

122. J.A.M. Boulet  
University of Tennessee  
310 Perkins Hall  
Knoxville, TN 37996
123. S. Bradley  
Garrett Ceramic Components  
Division  
19800 S. Van Ness Avenue  
Torrance, CA 90509
124. Raymond J. Bratton  
Westinghouse Electric  
Corporation  
1310 Beulah Road  
Pittsburgh, PA 15235
125. Catherine E. Brown  
E. I. DuPont de Nemours &  
Company  
Wilmington, DE 19898
126. J. J. Brown  
Virginia Polytechnic Institute  
and State University  
Blacksburg, VA 24061
127. W. Bryzik  
U.S. Army Tank Automotive  
Command  
Warren, MI 48090
- 128-132. S. T. Buljan  
GTE Laboratories, Inc.  
40 Sylvan Road  
Waltham, MA 02254
133. John M. Byrne, Jr.  
PPG Industries, Inc.  
One PPG Place  
Pittsburgh, PA 15272
134. Donald J. Campbell  
Air Force Wright  
Aeronautical Laboratory  
AFWAL/POX  
Wright-Patterson AFB  
OH 45433
135. Roger Cannon  
Rutgers University  
Post Office Box 909  
Bowser Road  
Piscataway, NJ 08855-0909
136. Harry W. Carpenter  
19945 Acre Street  
Northridge, CA 91324
137. David Carruthers  
Allied-Signal Aerospace  
Company  
Garrett Engine Division  
111 South 34th Street  
Post Office Box 5217  
Phoenix, AZ 85010
138. Jere G. Castor  
Allied-Signal Aerospace  
Company  
Garrett Engine Company  
111 South 34th Street  
Post Office Box 5217  
Phoenix, AZ 85010
139. Se-Tak Chang  
Sundstrand Corporation  
Turbomach Division  
4400 Ruffin Road  
San Diego, CA 92138-5757
140. R. J. Charles  
General Electric Company  
Post Office Box 8  
Schenectady, NY 12301
141. En-sheng Chen  
B&C Engineering Research  
13906 Dentwood Drive  
Houston, TX 77014
142. Albert A. Chesnes  
U.S. Department of Energy  
Forrestal Building CE-151  
1000 Independence Avenue  
Washington, DC 20585
143. Frank Childs  
EG&G, Inc.  
PO Box 1625  
Idaho Falls, ID 83415
144. Gilbert Y. Chin  
Bell Telephone Laboratories  
Murray Hill, NJ 07974

145. Melvin H. Chiogioji  
U.S. Department of Energy  
Forrestal Building CE-15  
1000 Independence Avenue, SW  
Washington, DC 20585
146. William J. Chmura  
The Torrington Company  
59 Field Street  
Torrington, CT 06790
147. Eugene V. Clark  
Turbine Metal Technology, Inc.  
7327 Elmo Street  
Tujunga, CA 91042-2204
148. William L. Cleary  
ORI, Inc.  
1375 Piccard Drive  
Rockville, MD 20850
149. Jack L. Clem  
J. M. Huber Corporation  
PO Box 2831  
Borger, TX 79008-2831
150. Philip R. Compton  
National Aeronautics and  
Space Administration  
Washington, DC 20546
151. Harry E. Cook  
Chrysler Motors Corporation  
1200 Chrysler Drive  
Highland Park, MI 48288-1118
152. Stephen Copley  
University of  
Southern California  
Los Angeles, CA 90089-0241
153. John A. Coppola  
Standard Oil Engineered  
Materials Company  
Structural Ceramics Division  
PO Box 1054, Bldg 91-2  
Niagara Falls, NY 14302
154. Normand D. Corbin  
Norton Company  
High Performance Ceramics  
Goddard Road  
Northboro, MA 01532-1545
155. Charles H. Craig  
Defense Technology Security  
Administration  
400 Army-Navy Drive  
Suite 300  
Arlington, VA 22202
156. William J. Croft  
U.S. Army Materials  
Technology Laboratory  
Arsenal Street  
Watertown, MA 02172
157. Gary M. Crosbie  
Ford Motor Company  
20000 Rotunda Drive  
PO Box 2053, Room S-2079  
Dearborn, MI 48121-2053
158. Floyd W. Crouse, Jr.  
U.S. Department of Energy  
PO Box 880  
Morgantown, WV 26505
159. Raymond Cutler  
Ceramatec, Inc.  
163 West 1700 South  
Salt Lake City, UT 84115
160. David A. Dalman  
The Dow Chemical Company  
Midland, MI 48640
161. James I. Dalton  
Reynolds Metals Company  
Fourth and Canal Streets  
PO Box 27003  
Richmond, VA 23261
162. Stephen C. Danforth  
Rutgers University  
Post Office Box 909  
Bowser Road  
Piscataway, NJ 08854

163. Stanley J. Dapkunas  
National Bureau of Standards  
Gaithersburg, MD 20899
164. Robert F. Davis  
North Carolina State University  
232 Riddick Laboratory  
Box 7907  
Raleigh, NC 27695
165. Evelyn M. DeLiso  
Rutgers University  
PO Box 909  
Bowser Road  
Piscataway, NJ 08854
166. Alan L. Dragoo  
National Bureau of Standards  
Gaithersburg, MD 20899
167. Keith F. Dufrane  
Battelle Columbus Laboratories  
505 King Avenue  
Columbus, OH 43201
168. Edmund M. Dunn  
GTE Laboratories Inc.  
40 Sylvan Road  
Waltham, MA 02254
169. Jeremy D. Dunning  
Indiana Memorial Union 662  
Indiana University  
Bloomington, IN 47405
170. Dr. Sunil Dutta  
NASA Lewis Research Center  
21000 Brookpark Road  
MS: 49-3  
Cleveland, OH 44135
171. Paul N. Dyer  
Air Products and Chemicals, Inc.  
PO Box 538  
Allentown, PA 18105
172. Robert J. Eagan  
Sandia National Laboratories  
Department 1840  
PO Box 5800  
Albuquerque, NM 87185
173. Christopher A. Ebel  
Norton Company  
High Performance Ceramics  
Goddard Road  
Northboro, MA 01532-1545
174. J. J. Eberhardt  
U.S. Department of Energy  
Forrestal Building CE-12  
1000 Independence Avenue, SW  
Washington, DC 20585
175. E. E. Ecklund  
U.S. Department of Energy  
Forrestal Building CE-151  
1000 Independence Avenue  
Washington, DC 20585
176. William A. Ellingson  
Argonne National Laboratory  
9700 South Cass Avenue  
Argonne, IL 60439
177. Graydon A. Elliott  
U.S. Army Research and  
Technology Laboratory  
(AVSCOM)  
Fort Eustis, VA 23604
178. A. Erdely  
26 Av. Gore des Eaux-Vives  
1208 Geneva  
SWITZERLAND
179. Charles D. Estes  
U.S. Senate  
Washington, DC 20510
180. Peggy Evanich  
National Aeronautics and  
Space Administration  
Washington, DC 20546
181. Anthony G. Evans  
University of California  
Santa Barbara, CA 93106
182. Robert C. Evans  
NASA Lewis Research Center  
21000 Brookpark Road  
MS: 77-6  
Cleveland, OH 44135



183. Katherine T. Faber  
Ohio State University  
2041 College Road  
Columbus, OH 43210
184. John W. Fairbanks  
U.S. Department of Energy  
Forrestal Building CE-151  
1000 Independence Avenue  
Washington, DC 20585
185. Larry Farrell  
Babcock and Wilcox  
Old Forrest Road  
Lynchburg, VA 24505
186. H. W. Foglesong  
Dow Corning Corporation  
3901 South Saginaw Road  
Midland, MI 48686
187. Thomas F. Foltz  
Avco Corporation  
Two Industrial Avenue  
Lowell, MA 01851
188. Robert G. Frank  
Technology Assessment Group  
10793 Bentley Pass Lane  
Cincinnati, OH 45140
189. Douglas W. Freitag  
LTV Aerospace and Defense  
Company  
PO Box 225907  
MS: TH-85  
Dallas, TX 75265
190. George E. Gazza  
U.S. Army Materials  
Technology Laboratory  
405 Arsenal Street  
Watertown, MA 02172
191. Charles M. Gilmore  
The George Washington  
University  
Washington, DC 20052
192. Paul Glance  
Concept Analysis  
950 Stephenson Highway  
Troy, MI 48007-7013
193. Fred M. Glaser  
U.S. Department of Energy  
Washington, DC 20545
194. Joseph W. Glatz  
Naval Air Propulsion  
Test Center  
Box 7176, PE 34  
Trenton, NJ 08628
195. W. M. Goldberger  
Superior Graphite Company  
2175 East Broad Street  
Columbus, OH 43209
196. Stephen T. Gonczy  
Allied Signal Research Center  
50 UOP Plaza  
Des Plaines, IL 60016-6187
197. Robert J. Gottschall  
U.S. Department of Energy  
MS: G-256  
Washington, DC 20545
198. Dr. Earl Graham  
Cleveland State University  
Uclid Ave East 24th Street  
Cleveland, OH 44115
199. Kenneth Green  
Coors Ceramics Company  
17750 West 32nd Street  
Golden, CO 80401
200. Robert E. Green, Jr.  
Center for Nondestructive  
Evaluation  
Maryland Hall 107  
The Johns Hopkins University  
Baltimore, MD 21218

- |   |   |
|---|---|
| <p>201. Lance E. Groseclose<br/>General Motors Corporation<br/>PO Box 420<br/>Indianapolis, IN 46206-0420</p> <p>202. T. D. Gulden<br/>GA Technologies, Inc.<br/>PO Box 81608<br/>San Diego, CA 92138</p> <p>203. P. Ulf Gummeson<br/>Hoeganaes<br/>River Road and Taylors Lane<br/>Riverton, NJ 08077</p> <p>204. Bimleshwar P. Gupta<br/>Solar Heat Research Division<br/>Solar Energy Research Institute<br/>1617 Cole Boulevard<br/>Golden, CO 80401</p> <p>205. M. D. Gurney<br/>NIPER<br/>PO Box 2128<br/>Bartlesville, OK 74005</p> <p>206. John P. Gyekenyesi<br/>NASA Lewis Research Center<br/>21000 Brookpark Road<br/>Cleveland, OH 44135</p> <p>207. J. J. Habeeb<br/>Esso Petroleum Canada<br/>PO Box 3022<br/>Sarina, Ontario<br/>CANADA N7T 7M1</p> <p>208. Pennsylvania State University<br/>227 Hammond Building<br/>University Park, PA 16802</p> <p>209. Nabil S. Hakim<br/>General Motors Corporation<br/>36880 Ecorse Road<br/>Romulus, MI 48174</p> <p>210. John W. Halloran<br/>Ceramic Process Systems<br/>840 Memorial Drive<br/>Cambridge, MA 02139-3758</p> | <p>211. Kay Hardman-Rhyne<br/>DARPA<br/>1400 Wilson Boulevard<br/>Arlington, VA 22209</p> <p>212. R. A. Harmon<br/>25 Schalren Drive<br/>Latham, NY 12110</p> <p>213. Stephen D. Hartline<br/>Norton Company<br/>High Performance Ceramics<br/>Goddard Road<br/>Northboro, MA 01532-1545</p> <p>214. Willard E. Hauth<br/>Dow Corning Corporation<br/>3901 South Siginaw Road<br/>Midland, MI 48640</p> <p>215. Kevin L. Haynes<br/>McDonnell Douglas<br/>Astronautics Company<br/>Box 516 E456/HQ/3N/MS329<br/>Saint Louis, MO 63166</p> <p>216. Norman L. Hecht<br/>University of Dayton<br/>Research Institute<br/>300 College Park<br/>Dayton, OH 45469-0001</p> <p>217. S. S. Hecker<br/>Los Alamos National<br/>Laboratory<br/>PO Box 1663<br/>Los Alamos, NM 87545</p> <p>218. Peter W. Heitman<br/>General Motors Corporation<br/>PO Box 420, W-5<br/>Indianapolis, IN 46206-0420</p> <p>219. Richard L. Helferich<br/>The Duriron Company,<br/>Incorporated<br/>PO Box 1145<br/>Dayton, OH 45401</p> <p>220. H. E. Helms<br/>General Motors Corporation<br/>PO Box 420<br/>Indianapolis, IN 46206-0420</p> |
|---|---|

221. Thomas L. Henson  
GTE Products Corporation  
Hawes Street  
Towanda, PA 18848-0504
222. Thomas P. Herbell  
NASA Lewis Research Center  
21000 Brookpark Road  
MS: 49-3  
Cleveland, OH 44135
223. Hendrik Heystek  
Bureau of Mines  
Tuscaloosa Research Center  
PO Box L  
University, AL 35486
224. Robert V. Hillery  
General Electric Company  
One Neumann Way  
PO Box 156301  
Cincinnati, OH 45215
225. Jonathan W. Hinton  
Standard Oil Engineered  
Materials Company  
Structural Ceramics Division  
PO Box 1054  
Niagara Falls, NY 14302
226. George Hsu  
Jet Propulsion Laboratory  
4800 Oak Grove Drive  
MS: 512-103  
Pasadena, CA 91109
227. Stephen M. Hsu  
National Bureau of Standards  
Gaithersburg, MD 20899
228. Harold A. Huckins  
Princeton Advanced  
Technology, Inc.  
56 Finley Road  
Princeton, NJ 08540
229. Fred Huettig  
Advanced Ceramic  
Technology, Inc.  
17 Deerfield Road  
East Brunswick, NJ 08816
230. O. Richard Hughes  
Celanese Research Company  
86 Morris Avenue  
Summit, NJ 07901
231. Joseph E. Hunter, Jr.  
General Motors Corporation  
12 Mile and Mound Roads  
Warren, MI 48090-9055
232. Louis C. Ianniello  
U.S. Department of Energy  
Washington, DC 20545
233. Robert H. Insley  
Champion Spark Plug Company  
20000 Conner Avenue  
Detroit, MI 48234
234. D. M. Jacques  
Norton Company  
HPC Library  
Goddard Road  
Northboro, MA 01532-1545
235. Curt A. Johnson  
General Electric Company  
PO Box 8  
Schenectady, NY 12301
236. Douglas C. Johnson  
Sundstrand Corporation  
4400 Ruffin Road  
PO Box 85757  
San Diego, CA 92138-5757
237. Larry Johnson  
Argonne National Laboratory  
9700 South Cass Avenue  
Bldg 362  
Argonne, IL 60439
238. R. A. Johnson  
General Motors Corporation  
PO Box 420  
Indianapolis, IN 46206-0420
239. L. A. Joo  
Great Lakes Research  
Corporation  
Post Office Box 1031  
Elizabethton, TN 37643

- 240. A. David Joseph  
Sealed Power Corporation  
100 Terrace Plaza  
Muskegon, MI 49443
- 241. Roy Kamo  
Adiabatics, Inc.  
630 South Mapleton  
Columbus, IN 47201
- 242. K. Karasek  
Garrett Ceramic Components  
Division  
19800 S. Van Ness Avenue  
Torrance, CA 90509
- 243. Allan Katz  
Air Force Wright  
Aeronautical Laboratory  
Materials Laboratory,  
AFWAL/MLLM  
Wright-Patterson AFB  
OH 45433
- 244. R. N. Katz  
U.S. Army Materials  
Technology Laboratory  
405 Arsenal Street  
Watertown, MA 02172
- 245. Mr. Kawaguchi  
Tokai Carbon  
375 Park Avenue  
Suite 3802  
New York, NY 10152
- 246. P. Victor Kelsey  
Aluminum Company of America  
Alcoa Technical Center B  
Alcoa Center, PA 15061
- 247. Frederick L. Kennard, III  
General Motors Corporation  
1300 North Dort Highway  
Flint, MI 48556
- 248. J. R. Kidwell  
Allied-Signal Aerospace  
Company  
Garrett Engine Division  
111 South 34th Street  
Post Office Box 5217  
Phoenix, AZ 85010
- 249. Max Klein  
Gas Research Institute  
8600 West Bryn Mawr Avenue  
Chicago, IL 60631
- 250. C. E. Knapp  
Norton Company  
8001 Daly Street  
Niagara Falls, Ontario  
CANADA
- 251. A. S. Kobayashi  
University of Washington  
Seattle, WA 98195
- 252. David M. Kotchick  
AiResearch Manufacturing  
Company  
2525 West 190th Street  
Torrance, CA 90509
- 253. Bruce Kramer  
George Washington University  
Washington, DC 20052
- 254. Saunders B. Kramer  
U.S. Department of Energy  
Forrestal Building CE-151  
1000 Independence Avenue  
Washington, DC 20585
- 255. D. M. Kreiner  
Allied-Signal Aerospace  
Company  
Garrett Engine Division  
111 South 34th Street  
PO Box 5217  
Phoenix, AZ 85010
- 256. Pieter Krijgsman  
Ceramic Design Int.  
Hold., Ltd.  
PO Box 68  
8050 AB Hattem  
THE NETHERLANDS
- 257. W. J. Lackey  
Georgia Tech Research  
Institute  
Atlanta, GA 30332

258. Everett A. Lake  
Air Force Wright  
Aeronautical Laboratory  
AFWAL/POOS  
Wright-Patterson AFB  
OH 45433
259. Hari S. Lamba  
General Motors Corporation  
Electro-Motive Division  
LaGrange, IL 60525
260. James Lankford  
Southwest Research Institute  
6220 Culebra Road  
PO Drawer 28510  
San Antonio, TX 78284
261. John G. Lanning  
Corning Glass Works  
Corning, NY 14831
262. David C. Larsen  
Corning Glass Works  
Sullivan Park, FR-51  
Corning, NY 14831
263. Dr. S. K. Lau  
Standard Oil Engineered  
Materials Company  
Technology Division  
Box 832  
Niagara Falls, NY 14302
264. Harry A. Lawler  
Standard Oil Engineered  
Materials Company  
Structural Ceramics Division  
PO Box 1054, Bldg 91-2  
Niagara Falls, NY 14302
265. Alan Lawley  
Drexel University  
Philadelphia, PA 19104
266. Daniel Lee Temescon  
2850 7th Street  
Berkeley, CA 94710
267. June-Gunn Lee  
Korea Advanced Institute of  
Science and Technology  
PO Box 131  
Dong Dac Mun, Seoul  
KOREA
268. E. M. Lenoe  
Air Force Office of  
Scientific Research  
APO San Francisco  
CA 96503-0110
269. Stanley R. Levine  
NASA Lewis Research Center  
21000 Brookpark Road  
Cleveland, OH 44135
270. David Lewis  
Naval Research Laboratory  
4555 Overlook Avenue, SW  
Washington, DC 20375
271. Winston W. Liang  
AMERCOM, Inc.  
8948 Fullbright Avenue  
Chatsworth, CA 91311
272. Bill Long  
Babcock and Wilcox  
PO Box 1260  
Lynchburg, VA 24505
273. L. A. Lott  
EG&G, Inc.  
PO Box 1625  
Idaho Falls, ID 83415
274. Bryan K. Luftglass  
Chem Systems, Inc.  
303 South Broadway  
Tarrytown, NY 10591
275. Robert Lundberg  
Svenska Silikatforsknings-  
institutet  
Swedish Institute for  
Silicate Research  
Box 5403  
S-402 29 Gothenburg  
SWEDEN

276. Michael J. Lynch  
General Electric Company  
PO Box 414, 7B-36  
Milwaukee, WI 53201
277. James W. MacBeth  
Standard Oil Engineered  
Materials Company  
Structural Ceramics Division  
Box 1054  
Niagara Falls, NY 14302
278. Vincent L. Magnotta  
Air Products and Chemicals, Inc.  
PO Box 538  
Allentown, PA 18105
279. Tai-il Mah  
Universal Energy Systems  
4401 Dayton-Xenia Road  
Dayton, OH 45432
280. L. Manes  
Commission of the European  
Communities  
Ispra Establishment  
1-21020 Ispra (Varese)  
ITALY
281. Gerald R. Martin  
Fleetguard, Inc.  
Cookeville, TN 38501
282. Dr. John L. Mason  
Allied-Signal Aerospace Company  
AiResearch Los Angeles Division  
2525 West 190th Street  
Torrance, CA 90509
283. J. McCauley  
U.S. Army Materials Technology  
Laboratory  
DRXMR-MC  
Arsenal Street  
Watertown, MA 02172-0001
284. William J. McDonough  
Keramont  
4233 South Fremont Avenue  
Tucson, AZ 85714
285. Bryan J. McEntire  
Norton Company  
TRW Ceramics  
Goddard Road  
Northboro, MA 01532-1545
286. Thomas D. McGee  
Iowa State University  
Ames, IA 50011
287. H. Christopher McGowan  
Advanced Ceramic  
Technology, Inc.  
17 Deerfield Road  
East Brunswick, NJ 08816
288. Malcolm G. McLaren  
Rutgers University  
PO Box 909  
Bowser Road  
Piscataway, NJ 08854
289. Arthur F. McLean  
6225 N Camino Almonte  
Tucson, AZ 85718
290. Brian L. Mehosky  
Standard Oil Engineered  
Materials Company  
4440 Warrensville Center Road  
Cleveland, OH 44128
291. P. K. Mehrotra  
Kennametal, Inc.  
PO Box 639  
Greensburg, PA 15601
292. Joseph J. Meindl  
Reynolds International, Inc.  
PO Box 27002  
6603 West Broad Street  
Richmond, VA 23261
293. D. Messier  
U.S. Army Materials  
Technology Laboratory  
DRXMR-MC  
Arsenal Street  
Watertown, MA 02172

294. Arthur G. Metcalfe  
Solar Turbines, Inc.  
2200 Pacific Highway  
PO Box 80966  
San Diego, CA 92138
295. Thomas N. Meyer  
Aluminum Company of America  
Alcoa Technical Center  
Alcoa Center, PA 15069
296. W. Miloscia  
Standard Oil Engineered  
Materials Company  
4440 Warrensville Center Road  
Cleveland, OH 44128
297. Bill Moehle  
Ethyl Corporation  
451 Florida Avenue  
Ethyl Tower  
Baton Rouge, LA 70801
298. Helen Moeller  
Babcock and Wilcox  
PO Box 11165  
Lynchburg, VA 24506-1165
299. Frederick E. Moreno  
Turbo Energy Systems, Inc.  
350 Second Street, Suite 5  
Los Altos, CA 94022
300. Peter E. D. Morgan  
Rockwell International  
1049 Camino Dos Rios  
PO Box 1085  
Thousand Oaks, CA 91360
301. Lawrence M. Murphy  
Thermal Systems Research  
Branch  
Solar Energy Research  
Institute  
1617 Cole Boulevard  
Golden, CO 80401
302. Solomon Musikant  
General Electric Company  
PO Box 8555  
MS: U-1219  
Philadelphia, PA 19101
303. Pero Nannelli  
Pennwalt Corporation  
900 First Avenue  
PO Box C  
King of Prussia, PA 19406-0018
304. Robert M. Neilson, Jr.  
EG&G Idaho, Inc.  
PO Box 1625  
Idaho Falls, ID 83415
305. William D. Nix  
Stanford University  
Stanford, CA 94305
306. Richard D. Nixdorf  
American Matrix, Inc.  
118 Sherlake Drive  
Knoxville, TN 37922
307. Brian M. O'Connor  
The Lubrizol Corporation  
29400 Lakeland Boulevard  
Wickliffe, OH 44092
308. W. Richard Ott  
Alfred University  
Alfred, NY 14802
309. Muktesh Paliwal  
GTE Products Corporation  
Hawes Street  
Towanda, PA 18848-0504
310. Hayne Palmour III  
North Carolina State  
University  
2158 Burlington Engineering  
Laboratories  
PO Box 5995  
Raleigh, NC 27607
311. Joseph N. Panzarino  
Norton Company  
Goddard Road  
Northboro, MA 01532-1545
312. Pellegrino Papa  
Corning Glass Works  
Corning, NY 14831

313. James G. Paschal  
Reynolds Metals Company  
PO Box 76154  
Atlanta, GA 30358
314. Arvid E. Pasto  
GTE Laboratories, Inc.  
40 Sylvan Road  
Waltham, MA 02254
315. Donald O. Patten  
Norton Company  
High Performance Ceramics  
Goddard Road  
Northboro, MA 01532-1545
316. James W. Patten  
Cummins Engine Company, Inc.  
Box 3005, Mail Code 50183  
Columbus, IN 47202-3005
317. Timothy M. Pattison  
Textron Lycoming  
MS: LSM1  
550 Main Street  
Stratford, CT 06497
318. Robert A. Penty  
Eastman Kodak Company  
901 Elmgrove Road  
Rochester, NY 14650
319. Gary R. Peterson  
U.S. Department of Energy  
785 DOE Place  
Idaho Falls, ID 83402
320. R. Byron Pipes  
University of Delaware  
2001 Spencer Laboratory  
Newark, DE 19716
321. Robert C. Pohanka  
Office of Naval Research  
800 North Quincy St, Code 431  
Arlington, VA 22217
322. Stephen C. Pred  
ICD Group, Inc.  
1100 Valley Brook Avenue  
Lyndhurst, NJ 07071
323. Karl M. Prewé  
United Technologies  
Corporation  
Silver Lane, MS: 24  
East Hartford, CT 06108
324. Hubert B. Probst  
NASA Lewis Research Center  
21000 Brookpark Road  
Cleveland, OH 44135
325. Carr Lane Quackenbush  
Norton Company  
High Performance Ceramics  
Goddard Road  
Northboro, MA 01532-1545
326. Brian Quigy  
National Aeronautics and  
Space Administration  
Washington, DC 20546
327. George Quinn  
U.S. Army Materials  
Technology Laboratory  
Arsenal Street  
Watertown, MA 02172
328. Dennis T. Quinto  
Kennametal, Inc.  
PO Box 639  
Greensburg, PA 15601
329. S. Venkat Raman  
Air Products and  
Chemicals, Inc.  
PO Box 538  
Allentown, PA 18105
330. Dennis Readey  
Ohio State University  
2041 College Road  
Columbus, OH 43210
331. Robert R. Reeber  
U.S. Army Research Office  
PO Box 12211  
Research Triangle Park  
NC 27709



- |  |   |
|--|---|
| <p>332. K. L. Reifsnider<br/>Virginia Polytechnic Institute<br/>and State University<br/>Blacksburg, VA 24061</p> <p>333. Paul Rempes<br/>Williams International<br/>2280 West Maple<br/>MS: 6-5<br/>Walled Lake, MI 48088</p> <p>334. T. M. Resetar<br/>U.S. Army Materials<br/>Technology Laboratory<br/>DAXMA-MC<br/>Arsenal Street<br/>Watertown, MA 02172</p> <p>335. K. T. Rhee<br/>Rutgers University<br/>PO Box 909<br/>Bowser Road<br/>Piscataway, NJ 08854</p> <p>336. Roy W. Rice<br/>W. R. Grace and Company<br/>7379 Route 32<br/>Columbus, MD 21044</p> <p>337. David W. Richerson<br/>Ceramatec, Inc.<br/>163 West 1700 South<br/>Salt Lake City, UT 84115</p> <p>338. Paul Rieth<br/>Ferro Corporation<br/>661 Willet Road<br/>Buffalo, NY 14218-9990</p> <p>339. Michael A. Rigdon<br/>Institute for Defense Analyses<br/>1801 Beauregard Street<br/>Alexandria, VA 22311</p> <p>340. John E. Ritter, Jr.<br/>University of Massachusetts<br/>Amherst, MA 01003</p> | <p>341. Giulio A. Rossi<br/>Norton Company<br/>High Performance Ceramics<br/>Goddard Road<br/>Northboro, MA 01532-1545</p> <p>342. Barry R. Rossing<br/>Lanxide Corporation<br/>Tralee Industrial Park<br/>Newark, DE 19711</p> <p>343. David J. Rowcliffe<br/>SRI International<br/>333 Ravenswood Avenue<br/>Menlo Park, CA 94025</p> <p>344. Donald W. Roy<br/>Coors Ceramics Company<br/>17750 West 32nd Street<br/>Golden, CO 80401</p> <p>345. Bruce Rubinger<br/>Gobal<br/>50 Milk Street, 15th Floor<br/>Boston, MA 02109</p> <p>346. Robert Ruh<br/>Air Force Wright<br/>Aeronautical Laboratory<br/>Materials Laboratory<br/>AFWAL/M LLM<br/>Wright-Patterson AFB<br/>OH 45433</p> <p>347. Robert J. Russell, Sr.<br/>Norton Company<br/>High Performance Ceramics<br/>Goddard Road<br/>Northboro, MA 01532-1545</p> <p>348. George P. Safol<br/>Westinghouse Electric<br/>Corporation<br/>Pittsburgh, PA 15235</p> <p>349. J. Sankar<br/>North Carolina Agricultural<br/>and Technical State<br/>University<br/>Greensboro, NC 27411</p> |
|--|---|

350. Maxine L. Savitz  
Garrett Processing Company  
Ceramic Components Divisio  
19800 South Van Ness Avenu  
Torrance, CA 90509
351. Richard Schapery  
Texas A&M University  
College Station, TX 77843
352. J. L. Schienle  
Allied-Signal Aerospace  
Company  
Garrett Auxiliary Power  
Division  
2739 East Washington Stree  
PO Box 5227  
Phoenix, AZ 85010
353. Liselotte J. Schioler  
Aerojet Tech Systems Compa  
PO Box 13222  
Dept. 9990, Bldg. 2019-A2  
Sacramento, CA 95813
354. Richard A. Schmidt  
Battelle Columbus  
Laboratories  
505 King Avenue  
Columbus, OH, 43201-2693
355. Arnie Schneck  
Deere and Company  
Technical Center  
PO Box 128  
Wood-Ridge, NJ 07075
356. Matthew Schreiner  
Gas Research Institute  
8600 West Bryn Mawr Avenue  
Chicago, IL 60631
357. John Schuldies  
Industrial Ceramic  
Technology, Inc.  
37 Enterprise Drive  
Ann Arbor, MI 48103
- 358-367. R. B. Schulz  
U.S. Department of Energy  
Forrestal Building CE-151  
1000 Independence Avenue  
Washington, DC 20585
368. Wesley J.C. Shuster  
Thermo Electron Corporation  
115 Eames Street  
PO Box 340  
Wilmington, MA 01887
369. Murray A. Schwartz  
Bureau of Mines  
2401 Eye Street, N.W.  
Washington, DC 20241
370. Douglas B. Schwarz  
The Dow Chemical Company  
52 Building  
Midland, MI 48674
371. Thomas M. Sebestyen  
U.S. Army Tank  
Automotive Command  
AMSTA-RGRT  
Warren, MI 48397-5000
372. Brian Seegmiller  
Coors Ceramics Company  
17750 West 32nd Street  
Golden, CO 80401
373. S. G. Seshadri  
Standard Oil Engineered  
Materials Company  
PO Box 832  
Niagara Falls, NY 14302
374. Peter T. B. Shaffer  
Advanced Refractory  
Technologies, Inc.  
699 Hertel Avenue  
Buffalo, NY 14207
375. Maurice E. Shank  
United Technologies  
Corporation  
East Hartford, CT 06108
376. Laurel M. Sheppard  
Advanced Materials and  
Processes  
Route 87  
Metals Park, OH 44073
377. Dinesh K. Shetty  
The University of Utah  
Salt Lake City, UT 84112

378. Jack D. Sibold  
Coors Ceramics Company  
17750 West 32nd Street  
Golden, CO 80401
379. Neal Sigmon  
U.S. House of Representatives  
Rayburn Building, Room B308  
Washington, DC 20515
380. Richard Silbergliitt  
Quest Research Corporation  
1651 Old Meadow Road  
McLean, VA 22102
381. Maurice J. Sinnott  
University of Michigan  
438 West Engineering Building  
Ann Arbor, MI 48109-2136
382. S. R. Skaggs  
Los Alamos National Laboratory  
PO Box 1663  
Los Alamos, NM 87545
383. J. Thomas Smith  
GTE Laboratories, Inc.  
40 Sylvan Road  
Waltham, MA 02254
384. Jay R. Smyth  
Allied-Signal Aerospace  
Company  
Garrett Auxiliary Power  
Division  
2739 East Washington Street  
PO Box 5227  
MS: 93-172/1302-2K  
Phoenix, AZ 85010
385. Rafal Sobotowski  
Standard Oil Engineered  
Materials Company  
3092 Broadway Avenue  
Cleveland, OH 44115
386. Thomas M. Sopko  
Lubrizol Enterprises, Inc.  
29400 Lakeland Boulevard  
Wickliffe, OH 44092
387. Boyd W. Sorenson  
Du Pont Company  
Experimental Stat, Bldg 304  
Wilmington, DE 19898
388. Dr. Richard M. Spriggs  
Center for Advanced  
Ceramic Technology  
New York State College  
of Ceramics at  
Alfred University  
Alfred, NY 14802
389. M. Srinivasan  
Standard Oil Engineered  
Materials Company  
PO Box 832  
Niagara Falls, NY 14302
390. Gordon L. Starr  
Cummins Engine Company, Inc.  
Box 3005, Mail Code 50183  
Columbus, IN 47202-3005
391. Harold L. Stocker  
General Motors Corporation  
PO Box 420, T-23  
Indinapolis, IN 46206-0420
392. Paul D. Stone  
The Dow Chemical Company  
1801 Building  
Midland, MI 48674
393. Roger Storm  
Standard Oil Engineered  
Materials Company  
PO Box 832  
Niagara Falls, NY 14302
394. E. E. Strain  
Allied-Signal Aerospace  
Company  
Garrett Engine Division  
111 South 34th Street  
PO Box 5217  
MS: 301-2N  
Phoenix, AZ 85010

- |  |  |
|--|--|
| <p>395. Thomas N. Strom<br/>NASA Lewis Research Center<br/>21000 Brookpark Road, 77-6<br/>Cleveland, OH 44135</p> <p>396. Jerry Strong<br/>Albright &amp; Wilson<br/>PO Box 26229<br/>Richmond, VA 23260</p> <p>397. Richard Suddeth<br/>Boeing Motor Airplane Company<br/>PO Box 7730<br/>MS: K-76-67<br/>Wichita, KS 67277</p> <p>398. Paul Sutor<br/>Midwest Research Institute<br/>425 Volker Boulevard<br/>Kansas City, MO 64116</p> <p>399. J. J. Swab<br/>U.S. Army Materials<br/>Technology Laboratory<br/>405 Arsenal Street<br/>Watertown, MA 02172</p> <p>400. John W. Swain, Jr.<br/>Kollmorgen Corporation<br/>PCK Technology Division<br/>15424 Garrison Lane<br/>Southgate, MI 48915</p> <p>401. Lewis Swank<br/>Ford Motor Company<br/>20000 Rotunda Drive<br/>PO Box 2053<br/>Building SRL, Room S2023<br/>Dearborn, MI 48121-2053</p> <p>402. Stephen R. Tan<br/>ICI Advanced Materials<br/>PO Box 11<br/>The Heath, Runcorn<br/>Cheshire<br/>ENGLAND WA7 4QE</p> <p>403. Anthony C. Taylor<br/>U.S. House of Representatives<br/>Rayburn Building, Room 2321<br/>Washington, DC 20515</p> | <p>404. W. H. Thielbahr<br/>U.S. Department of Energy<br/>550 2nd Street<br/>Idaho Falls, ID 83401</p> <p>405. John K. Tien<br/>Columbia University<br/>1137 S.W. Mudd Building<br/>New York, NY 10027</p> <p>406. T. Y. Tien<br/>University of Michigan<br/>Dow Building<br/>Ann Arbor, MI 48109-2136</p> <p>407. Julian M. Tishkoff<br/>Air Force Office of<br/>Scientific Research<br/>(AFOSR/WC) Bolling AFB<br/>Washington, DC 20332</p> <p>408. Louis E. Toth<br/>National Science Foundation<br/>1800 G Street, N.W.<br/>Washington, DC 20550</p> <p>409. Richard E. Tressler<br/>Pennsylvania State University<br/>201 Steidle Building<br/>University Park, PA 16802</p> <p>410. Donald R. Uhlmann<br/>Massachusetts Institute<br/>of Technology<br/>77 Massachusetts Avenue<br/>Cambridge, MA 02139</p> <p>411. Edward C. Van Reuth<br/>Technology Strategies, Inc.<br/>10722 Shingle Oak Court<br/>Burke, VA 22015</p> <p>412. Thomas Vasilos<br/>Avco Corporation<br/>201 Towell Street<br/>Wilmington, MA 01887</p> <p>413. V. Venkateswaran<br/>Standard Oil Engineered<br/>Materials Company<br/>PO Box 832<br/>Niagara Falls, NY 14302</p> |
|--|--|

414. John B. Wachtman, Jr.  
Rutgers University  
PO Box 909  
Bowser Road  
Piscataway, NJ 08854
415. Richard B. Wallace  
General Motors Corporation  
36880 Ecorse Road  
Romulus, MI 48174
416. Harlan L. Watson  
U.S. House of Representatives  
Rayburn Building, Suite 2321  
Washington, DC 20515
417. John D. Watson  
BHP Research & New Technology  
Melbourne Research Laboratories  
245 Wellington Road  
Mulgrave, Vic. 3170  
AUSTRALIA
418. Albert R. C. Westwood  
Martin Marietta Laboratories  
1450 South Rolling Road  
Baltimore, MD 21227
419. Thomas J. Whalen  
Ford Motor Company  
20000 Rotunda Drive  
PO Box 2053  
Dearborn, MI 48121-2053
420. Sheldon M. Wiederhorn  
National Bureau of Standards  
Gaithersburg, MD 20899
421. James C. Williams  
Carnegie-Mellon University  
Schenley Park  
Pittsburgh, PA 15213
422. Roger R. Wills  
TRW, Inc.  
Valve Division  
1455 East 185th Street  
Cleveland, OH 44110
423. J. M. Wimmer  
Allied-Signal Aerospace  
Company  
Garrett Engine Division  
111 South 34th Street  
Post Office Box 5217  
Phoenix, AZ 85010
424. David Wirth  
Coors Ceramics Company  
17750 West 32nd Street  
Golden, CO 80401
425. Thomas J. Wissing  
Eaton Corporation  
26201 Northwestern Highway  
Post Office Box 766  
Southfield, MI 48037
426. Dale Wittmer  
Southern Illinois University  
at Carbondale  
Department of Mechanical  
Engineering and  
Energy Processes  
Carbondale, IL 62901
427. George W. Wolter  
Howmet Turbine Components  
Corporation  
699 Benston Road  
Whitehall, MI 49461
428. James C. Wood  
NASA Lewis Research Center  
21000 Brookpark Road  
MS: 500-210  
Cleveland, OH 44135
429. Roger P. Worthen  
Eaton Corporation  
26201 Northwestern Highway  
PO Box 766  
Southfield, MI 48076
430. Hun C. Yeh  
Garrett Processing Company  
Ceramic Components Division  
19800 Van Ness Avenue  
Torrance, CA 90509

431. Thomas M. Yonushonis  
Cummins Engine Company, Inc.  
Box 3005, Mail Code 50183  
Columbus, IN 47202-3005
432. Don Zabierek  
Air Force Wright  
Aeronautical Laboratory  
AFWAL/POTC  
Wright-Patterson AFB  
OH 45433
433. Charles Zeh  
U.S. Department of Energy  
PO Box 880  
Morgantown, WV 26505
434. Anne Marie Zerega  
U.S. Department of Energy  
Forrestal Building CE-15  
1000 Independence Avenue  
Washington, DC 20585
435. G. Zilberstein  
GTE Laboratories Inc.  
40 Sylvan Road  
Waltham, MA 02254
436. Martin Zlotnick  
Nichols Research Corporation  
8618 Westwood Center Dr.  
Suite 200  
Vienna, VA 22180-2222
437. Klaus M. Zwilsky  
National Research Council  
2101 Constitution Avenue  
Washington, DC 20418
438. Department of Energy  
Oak Ridge Operations Office  
Assistant Manager for Energy  
Research and Development  
P.O. Box 2001  
Oak Ridge, TN 37831
- 439-505. Department of Energy  
Office of Scientific and  
Technical Information  
Office of Information Service  
P.O. Box 62  
Oak Ridge, TN 37831
- For distribution by microfiche  
as shown in DOE/TIC-4500,  
Distribution Category UC-95.